Elsevier Editorial System(tm) for Journal of Manufacturing Processes

Manuscript Draft

Manuscript Number: SMEJMP-D-17-00969R2

Title: Pulsed Laser Remelting of A384 Aluminum, Part II: Modeling of Surface Homogenization and Topographical Effects

Article Type: Full Length Article

Keywords: Aluminum; Laser; Remelting; Simulation; Homogenization; Roughness

Corresponding Author: Professor Frank E pfefferkorn, Ph.D.

Corresponding Author's Institution: University of Wisconsin-Madison

First Author: Brodan Richter, M.S.

Order of Authors: Brodan Richter, M.S.; Shixuan Chen; Justin D Morrow, Ph.D.; Kumar Sridharan, Ph.D.; Melih Eriten, Ph.D.; Frank E pfefferkorn, Ph.D.

Abstract: A simulation model is developed for pulsed laser remelting that captures the homogenization of surface chemical composition and height variations that occur due to silicon (Si) precipitates in a hypereutectic aluminum-silicon (Al-Si) casting alloy. The model simulates remelting pulse-by-pulse with two sequential and repeated steps - it first predicts surface homogenization by areal averaging within a laser spot and then generates and adds a surface feature, due to thermocapillary flow, whose size depends on the concentration of Si within the homogenized spot. Compositional data of remelted lines was collected with energy-dispersive x-ray spectroscopy and used to verify the homogenization step of the simulation model. It was found that Si precipitates get redistributed by the laser with the peak in Si concentration occurring in the direction opposite that of beam travel. Height data from remelted lines were measured using white light interferometry to verify the accuracy of the remelting model in simulating surface topographical modifications. It was found that variations of approximately +/- 1 μm are induced in the Al-Si alloy during pulsed laser remelting due to the Si proeutectic precipitates. This is attributed to differences in laser absorption of Si and Al. Because the Si precipitates absorb more energy from the laser, they experience higher temperatures and temperature gradients, which cause larger thermocapillary flow. The results provide insights into approaches to model surface compositional homogenization that occurs during laser remelting and provides an understanding of surface microstructural and topographical features often seen in laser polished of Al-Si casting alloys.

Suggested Reviewers:

Opposed Reviewers:

Pulsed Laser Remelting of A384 Aluminum, Part II: Modeling of Surface Homogenization and Topographical Effects

Brodan Richter[1], Shixuan Chen[2], Justin D. Morrow[1], Kumar Sridharan[3], Melih Eriten[1], Frank E. Pfefferkorn[1,*]

[1] Department of Mechanical Engineering, University of Wisconsin-Madison, USA
[2] Department of Materials Science and Engineering, University of Wisconsin-Madison, USA
[3] Department of Engineering Physics, University of Wisconsin-Madison, USA
[*] Corresponding author. email: frank.pfefferkorn@wisc.edu

Abstract

A simulation model is developed for pulsed laser remelting that captures the homogenization of surface chemical composition and height variations that occur due to silicon (Si) precipitates in a hypereutectic aluminum-silicon (Al-Si) casting alloy. The model simulates remelting pulse-by-pulse with two sequential and repeated steps - it first predicts surface homogenization by areal averaging within a laser spot and then generates and adds a surface feature, due to thermocapillary flow, whose size depends on the concentration of Si within the homogenized spot. Compositional data of remelted lines was collected with energy-dispersive x-ray spectroscopy and used to verify the homogenization step of the simulation model. It was found that Si precipitates get redistributed by the laser with the peak in Si concentration occurring in the direction opposite that of beam travel. Height data from remelted lines were measured using white light interferometry to verify the accuracy of the remelting model in simulating surface topographical modifications. It was found that variations of approximately +/- 1 μm are induced in the Al-Si alloy during pulsed laser remelting due to the Si proeutectic precipitates. This is attributed to differences in laser absorption of Si and Al. Because the Si precipitates absorb more energy from the laser, they experience higher temperatures and temperature gradients, which cause larger thermocapillary flow. The results provide insights into approaches to model surface compositional homogenization that occurs during laser remelting and provides an understanding of surface microstructural and topographical features often seen in laser polished of Al-Si casting alloys.

Keywords: Aluminum; Laser; Remelting; Simulation; Homogenization; Roughness

1. Introduction

Due to the ability of lasers to induce localized melting and ablation in a controlled manner, they have found numerous applications in manufacturing and material processing. One category of laser processing is laser surface treatment where the laser beam irradiates and melts a thin surface layer of a metallic alloy. In this melted layer, fluid flow is induced due to surface tension, temperature gradients within the melt pool, and buoyancy from density differences [1]. These flow effects cause mixing of the constituents within the melt pool and form the basis for laser surface alloying [2] and laser cladding [3]. Many numerical models have been developed to simulate the fluid dynamics and heat transfer within a melt pool during laser remelting [4–6]. For example, it has been demonstrated that a particle will recirculate numerous times before solidification within a melt pool created with a laser beam diameter of 0.5 mm and scanning velocities of 25 and 50 mm/s [4]. Other work simulating laser welding has shown that the induced velocities in the melt pool due to recirculation motion in a 0.2 mm beam can range from 5.5-6.9 m/min [5]. In work modeling stationary laser melting, non-dimensional surface velocities were found to range between 0 and 0.2 of the surface tension reference velocity for the lowest temperature coefficient of surface tension case. Those values correspond to velocities of 0 to ~10 m/s for melt diameters of ~0.5 mm in radius. The recirculating streamlines that occur within the melt pool are also presented [6]. The rapid freezing event that occurs during laser remelting has been shown to refine the microstructure on aluminum-silicon (Al-Si) alloys by creating finer silicon (Si) grains [7–14]. The process has also been shown to improve and reduce the corrosion resistance of Al-Si alloys to various solvents [8,11,12,14]. The Vickers microhardness in Al-Si alloys has also been observed to increase following laser remelting [7–14] in addition to changes in mechanical properties [12].

Flows on the surface due to surface tension and temperature gradients have also been used to reduce surface roughness features and have led to a subfield of laser remelting termed laser polishing [15–21]. The surface topography (*e.g.*, roughness) resulting from laser remelting has been modeled by various

approaches [15,22,23]. Starting with the Navier-Stokes equations for fluid flow, a description of capillary surface waves was derived, which showed that the spatial frequencies of a surface are reduced proportional to a critical frequency related to the melt duration [21,24]. That critical frequency was applied to a surface smoothing model that uses a Gaussian filter to predict the surface after *capillary regime polishing* [22]: *i.e.*, where thermocapillary flow is negligible. Capillary regime polishing occurs for shorter melt durations and shallower melt pools. As the melt duration and melt pool depth become large, thermocapillary or Marangoni flow from temperature gradients across the melt pool can become large enough to cause a surface feature from net fluid motion from the middle of the melt pool towards the perimeter. Through numerical heat transfer and fluid flow simulations, a numerical-empirical relationship was derived that relates the normalized melting temperature of the material to the normalized average displacement during laser remelting [25]. This simulation of the displacement of material was applied to predict the surface features generated as a result of *thermocapillary regime polishing* [23].

Smoothing from laser polishing has been applied to a variety of engineering materials [26]. However, aluminum (Al) alloys have received less attention relative to ferrous or titanium alloys, and with most of the published work focusing on Al-Si alloys. One study was unable to laser polish forged AlCu4MgPb but was able to polish Al casting alloy AlSi10Mg(Fe) from an initial average surface roughness, R_a = 1.37 μm to an Ra of ~0.47 μm using a laser beam 292 μm in diameter [27]. However, the resultant surface displayed large bumps and the study only considered roughness with wavelengths between 2.5-800 μm. In other studies, on laser polishing of a ground AlSi9MnMg surface achieved a reduction in values of R_a from ~2.2 μm to ~0.2 μm [28]. Inhomogeneities were found on the remelted surfaces that were attributed to porosity. Laser polishing has also been applied to selective laser melted AlSi10Mg, where the R_a was reduced from 8.7 μm to 0.66 μm [29], where appearance of bumps over the region of measurement was reported. All of the relevant studies on laser polishing of Al-Si alloys have reported either bumps or inhomogeneities on the resulting surface. One potential reason for these resultant features is the high percentage of Si in the Al alloys being studied. Si is a common element in Al alloys, as it imbues castings

with better fluidity and mold filling ability [30]. However, Si, which has only a 1.65 wt.% solubility in Al at 577°C when cooling in equilibrium, precipitates out of liquid Al during cooling and forms proeutectic Si particles and/or a eutectic Al-Si mixture [31]. As Al and Si have different light absorption properties [32,33], a variance in thermal conditions during laser remelting would be expected and may be the cause for the features left on surfaces during laser remelting of Al alloys.

Both the *capillary regime polishing* and *thermocapillary regime polishing* (*i.e.*, remelting) smoothing models developed at the University of Wisconsin-Madison rely on the assumption of a perfectly homogeneous melting condition [22,23]. However, many materials, such as Al-Si alloys, have a heterogeneous chemical composition that can be reasonably assumed to experience non-homogenous melting conditions. The work presented here includes two new additions to the laser remelting models that enable it to predict the compositional distribution and surface topography resulting from pulsed laser remelting of Al-Si alloys (*e.g.,* A384). The model presented accounts for: (1) the compositional redistribution in melt pools, and (2) the variation in laser absorption of the different constituents (*e.g.,* Al-matrix versus Si precipitates). This model enables more accurate prediction of surface topography resulting from pulsed laser remelting of a compositionally heterogeneous surface. The goal of this study was to understand the effect of the initial surface chemical composition on the process and resultant surface chemical distribution following laser remelting. In general, previous studies on laser remelting of Al-Si alloys have been performed on a macro-scale with a continuous laser beam of diameters between 0.5 – 4.0 mm and melt depths measured in hundreds of micrometers. Conversely, this work examines pulsed laser remelting with a beam diameter less than 100 μm, melt depths of approximately 5 μm, and studies the effect of individual grains on the remelting process. The results and ensuing discussions provide insights into why surface features remain after laser remelting of some alloys and how laser remelting can achieve chemical homogenization at the surface.

2. Materials and Experimental Methods

2.1 Materials

This work studies the effect of pulsed laser remelting on Al alloy A384 that was manufactured using gravity die casting. A384 contains a high weight percentage of Si (10.5 – 12.0%) that precipitates out during solidification into proeutectic grains (approximately 10-30 μm diameter) and a smaller eutectic phase (approximately 1-2 μm width and 10-60 μm length in cross-section) within the Al-alloy matrix matrix [31,34]. The other alloying elements are shown in Table 1. This alloy was chosen to study the effect of a highly inhomogeneous chemical composition on pulsed laser remelting. Si and Al have significantly different absorption coefficients for 1070-nm-wavelength light (9% absorption for Al [32] versus 69% absorption for Si [33]), which is the wavelength emitted by the fiber laser used in this study. The result is a difference in the thermal history experienced by different regions on the surface of the sample. The difference in absorption of 1070-nm-wavelength light for Si and Al is used to estimate the amount of thermocapillary flow that occurs in the remelting model (presented in §3.2).

Table 1: Composition percentage (wt%) of aluminum alloy A384 [34]

Si	Cu	Fe	Zn	Others (Mn, Ni, Sn, Mg, etc.)	Al
10.5-12.0	3.0-4.5	< 1.3	< 1.0	< 1.95	Balance

2.2 Pulsed Laser Remelting

The pulsed laser remelting experiments were performed using a 200 W, 1070 nm, fiber laser (SPI Lasers, SP-200C-W-S6-A-B) with a Gaussian-shaped beam. This is a continuous wave fiber laser that is pulsed by turning the pumping diodes on and off, hence the pulse power is the same as the peak power during a pulse. The laser was pulsed using an external control card (LasX Foresight), and the power was controlled using the laser manufacturer's control software. The pulsed laser beam was scanned over the sample surface to create lines of overlapped remelted spots using a 30-μm-diameter and 100-μm-diameter

beam (the former creating a 25-µm-diameter melt pool and the latter creating a 55-µm-diameter melt pool) to verify the ability of the remelting model to predict compositional homogenization and surface height variations. The laser parameters were chosen such that the 30-µm-diameter beam and 100-µm-diameter beam conditions would have a similar pulse fluence and spot overlap (Table 2). In addition, a 1 mm x 1 mm area was remelted with the 30-µm-diameter beam to study the ability of the model to accurately simulate the results of areal remelting. The remelting was performed in a vacuum chamber at a base pressure of 0.07 Torr to mitigate oxidation of the molten surface.

Table 2: Laser remelting parameters used in this study

	30-µm-dia. Condition	**100-µm-dia. Condition**
Beam Diameter (µm)	**30**	**100**
Melt Diameter (µm)	25	55
Pulse Power (W)	20	150
Pulse Fluence (J/mm^2)	1.88	1.27
Pulse Duration (µs)	66.7	66.7
Pulse Frequency (kHz)	3	3
Pulse Duty Cycle (%)	20	20
Scan Velocity (mm/s)	15	45
Horizontal Spot Spacing 'step over' (µm)	5	15
Vertical Spot Spacing 'scan direction' (µm)	5	15
Spot Overlap (%)	83	85

2.3 Surface Analysis

To study the effect of A384's heterogeneous chemical composition on laser remelting outcomes (*e.g.*, surface height changes), samples were mechanically polished to a mirror-like finish using progressive grinding and polishing steps (Buehler MetaServ 250 Grinder-Polisher), with the final polishing step using 0.05 µm colloidal silica. Following this, the surface was cleaned using methanol and delicate task wipes. A focus variation optical microscope (Alicona InfiniteFocus G4) was used to image the Si grains before (with 20x objective) laser remelting and the resulting surface (with 100x objective) after laser remelting. Surface height data was collected using a white light interferometer (Zygo NewView 6300, 50x objective). Energy dispersive x-ray spectroscopy (LEO 1530 FESEM/EDS) with an accelerating voltage of 15 keV was performed to measure the elemental distribution of Al and Si within the remelted regions.

Image processing was used (MATLAB 2016b, ImageJ 1.51n [35,36]) to overlay the Si grains captured before remelting onto the surface following laser processing. When converting the optical image to a binary black-and-white image, a grayscale threshold value of 170 was used on the 8-bit grayscale image to distinguish the Si and Al-rich phases.

3. Modeling the Remelting Process

During the remelting process, fluid flow occurs due to temperature gradients within the melt pool. This fluid flow is often referred to as thermocapillary or Marangoni flow and is caused by variations in surface tension as a function of temperature [4,25]. Previous simulation work presented a model for pulsed laser polishing that predicts the induced feature slope of a surface feature created due to thermocapillary flow and generates a unit cell which is applied across the surface to estimate the surface characteristics after laser polishing [23]. This work incorporates a similar approach, but rather than generate a unit cell that is replicated across the surface, each spot is simulated in sequence and added to the mean plane within the current area being irradiated. The model being presented also incorporates an additional step which predicts surface homogenization to allow for the estimation of differences in flow that arise due to an initially heterogeneous surface chemical composition. Previous work also incorporated a Gaussian filter to estimate smoothing due to capillary forces from surface asperities [22]. As this work starts with a polished surface, a Gaussian filter is not applied.

3.1 Modeling Surface Homogenization

The chemical homogenization of the surface during laser remelting is modeled through a pulse-by-pulse procedure (Figure 1a). A grayscale image of the initial chemical composition is read in by the model as the initial chemical composition to simulate. The area is processed using image thresholding to separate sections that are Al and Si. Areas that are black (an intensity of 0) are assumed to be 100% Si, and areas that are white (an intensity of 1) are assumed to be an Al-rich matrix. Individual pulses are sequentially simulated. When a simulated spot (*e.g.*, melt pool) overlaps a region containing both Si and the Al-rich matrix (Figure 1b), the intensity within the region is averaged (Figure 1c). For example, if a

pulse overlaps a Si grain and contains 30% Si (30% of an intensity of 0) and 70% Al-rich matrix (70% of an intensity of 1), the resultant spot would be a mixture of 70% Al-rich matrix and 30% Si (100% of an intensity of 0.70). Hence, this model assumes that each melt pool results in a homogeneous distribution of the elements in the melt pool. As each spot overlaps, the next simulated spot would contain a portion of the previous remelted region as well as a new area that has not yet been affected.

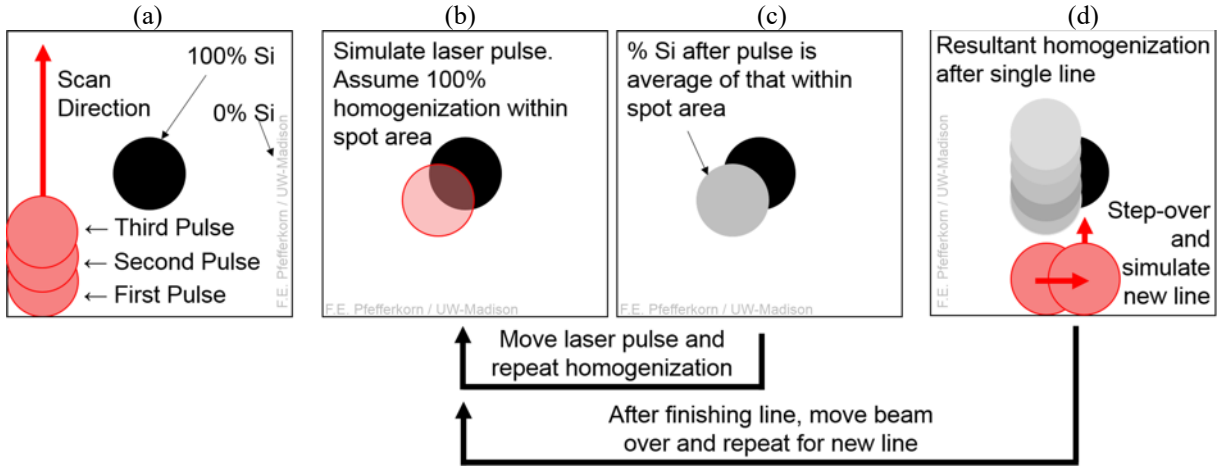

Figure 1: Schematic illustration of the concept underlying simulation of surface homogenization. (a) The model simulates individual laser pulses. It assumes black areas to be 100% Si and white areas to be 100% Al-rich matrix, (b) When a pulse contains both Si and Al, (c) it averages the intensities into a gray-scale value, (d) After the first pulse containing Si is homogenized, subsequent pulses incorporate part of the previous homogenized area into a new homogenized area. This spreads the initial chemical composition. After an entire line is completed, a new line starts.

This pulse-by-pulse modeling of surface homogenization causes the composition on the surface to be distributed into an area much greater in size than the initial surface feature. Once an entire line has been simulated, the beam moves over the step-over distance and the next line is simulated (Figure 1d). Through this simulation, both individual remelted lines as well as remelted areas can be modeled.

3.2 Modeling Surface Height Variation

A temperature gradient exists within the melt pool during pulsed laser remelting. For materials that have a negative surface tension temperature gradient (*i.e.,* less surface tension with higher temperatures), a net flow occurs from the inside to the outside of the melt pool (Figure 2a). This is because a Gaussian laser intensity distribution will result in higher temperatures at the center of the melt pool, which will also cool from the outside towards the center. This causes a depression towards the center of the laser spot and

an uplifting of material towards the perimeter. After the remelting model calculates the homogenization within a laser spot, it generates a surface feature meant to simulate the feature that thermocapillary flow creates (Figure 2c).

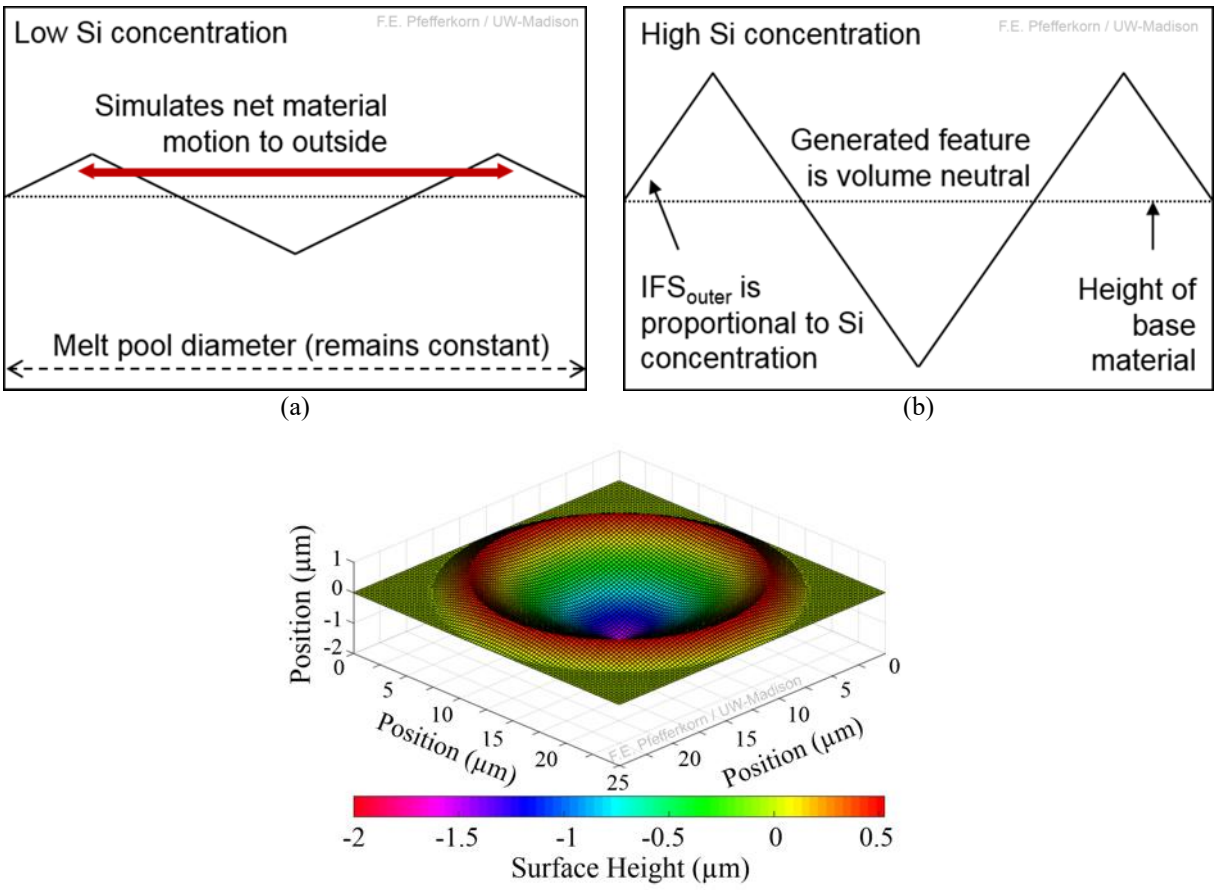

Figure 2: Two-dimensional schematic of model's representation of thermocapillary flow during a single laser pulse (*i.e.*, remelting and resolidification event) with (a) low Si concentration and (b) high Si concentration. (c) 3D schematic illustration of simulated feature generated with thermocapillary flow.

Based on experimental observations, areas with higher Si content experience more thermocapillary flow. This is, at least partially, due to the higher absorption of 1070-nm-wavelength laser light by Si as compared to Al. To model this phenomenon, the melt pool's induced feature slope is made linearly proportional to the percentage of Si within the simulated spot as well as the ratio of Si to Al absorption (Figure 2b and Eq. 1)

$$\boldsymbol{IFS_{spot,outer} = IFS_{Al-matrix,outer}\left[\%Al + \frac{\alpha_{Si,1070\,nm}}{\alpha_{Al,1070\,nm}}(1 - \%Al)\right]} \quad [1]$$

where, $IFS_{spot,\ outer}$ is the introduced feature slope on the outer portion of the generated feature. The values used were $\alpha_{Al,\ 1070\ nm} = 0.09$ [32], $\alpha_{Si,\ 1070\ nm} = 0.69$ [33], and $IFS_{Al\text{-}matrix,outer} = 0.21$. The $IFS_{Al\text{-}matrix,outer}$ value was estimated through experimental measurements on the line remelted using the 30-µm-diameter beam. The $IFS_{Al\text{-}maxrix,outer} = 0.21$ is similar to those reported for Ti-6Sl-4V and S7 tool steel [23]. This simulation uses a triangular approximation of a thermocapillary feature to model the primary physics of the process and is not trying to replicate with high precision the thermocapillary features observed experimentally and in numerical models [37]. After generating a new surface feature, it is added to the surface by taking a mean-plane of the area within the spot prior to adding the new feature. Adding using a mean plane is required to conserve the mass of the simulated surface. Additional details on the generation of a thermocapillary feature and its addition to the surface is outlined in SUPPLEMENTAL MATERIAL.

3.3 Model Assumptions

The assumptions of the current implementation of the remelting model are:

1. Only melting (*i.e.,* no ablation) occurs during the process.
2. The melt pool diameter does not depend on the Si concentration.
3. The size of the induced feature slope is linearly proportional to the Si concentration and the ratio of absorption of 1070-nm-wavelength light for Si and Al.
4. The size of the induced feature slope on the outer portion of the melt pool is the same when using a 30-µm-diameter beam (25-µm-diameter melt pool) and 100-µm-diameter beam (55-µm-diameter melt pool).
5. The melt duration is long enough for both conditions that significant thermocapillary flow occurs and material accumulates near the melt pool perimeter, as observed in previous experiments and finite element simulations [25,37].
6. A triangular representation of a thermocapillary feature is a reasonable approximation.
7. Perfect homogenization occurs within a melt pool during a single laser pulse.

8. Areal averaging (rather than volumetric) reasonably represents the homogenization.
9. The other elements found within the material have no effect on the process.
10. When simulating a spot, the compositional homogenization occurs before the height estimation rather than simultaneously.

Many of these assumptions are not intrinsically necessary in the design of the simulation model, and future versions of the model can loosen these assumptions. The simulation as presented is designed to help assess its ability to capture the primary physics occurring during remelting: *i.e.*, test the hypothesis that heterogeneous chemistry can account for some of the surface roughness that is observed.

4. Model Verification

To verify that the model accurately captures the physics of the remelting process, individual lines with two different beam diameters were scanned over the base material and compared with simulated results. Through image processing, proeutectic Si grains that the remelted lines scanned over were extracted and overlaid onto the remelted regions. The proeutectic and eutectic Si phases discussed in §2.1 can be observed in Figure 3. These extracted Si grains were then used in the simulation model. In Figure 3b and 3d it can be seen that dark spots occur to the left of where the Si grains were originally located.

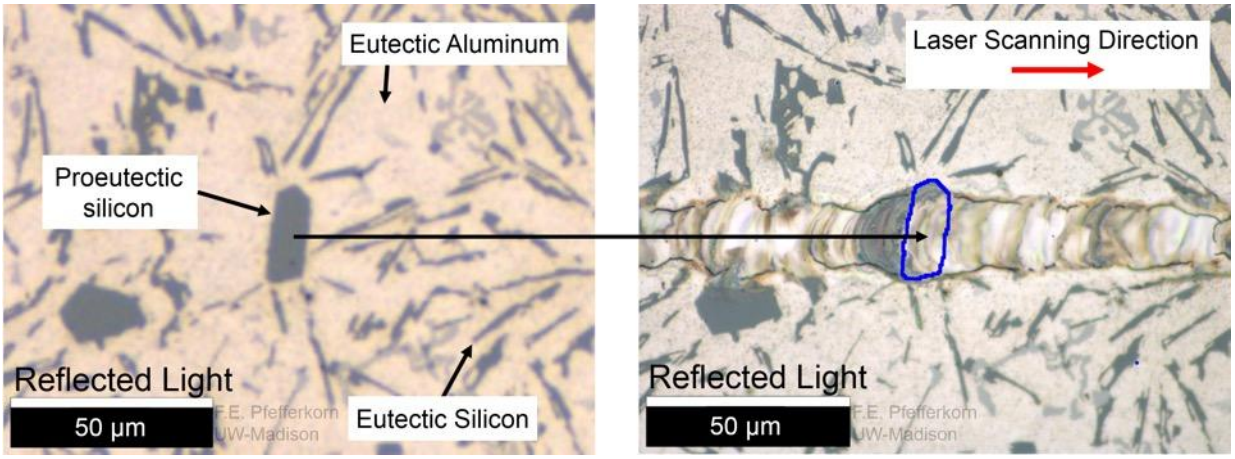

(a) (b)

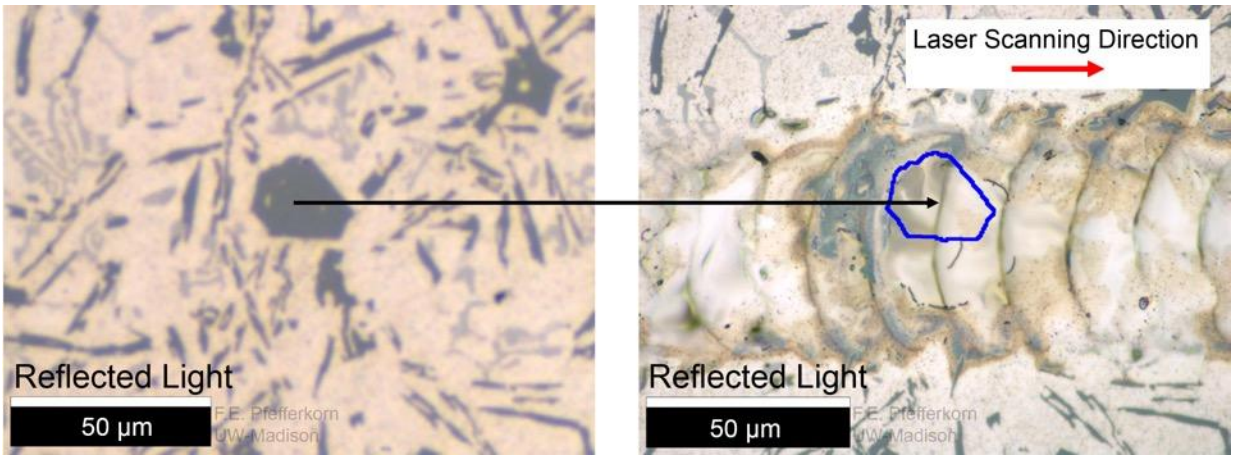

(c) (d)

Figure 3: Optical (reflected light) images of 30-µm-diameter beam (25-µm-diameter melt pool) (a) before and (b) after line remelting and the 100-µm-diameter beam (55-µm-diameter melt pool) (c) before and (d) after line remelting.

When simulating individual remelted lines, only the proeutectic Si grains that were remelted were considered (Figure 4c). This was done by isolating the Si grain with image processing prior to using the model. When simulating an entire remelted area (presented in §5), the eutectic Si grains were also considered in the model to yield more comprehensive results (input similar to that in Figure 4b).

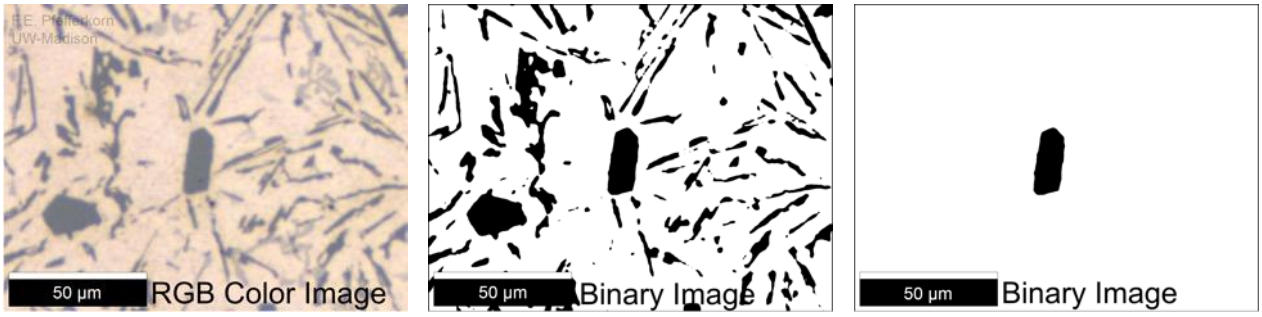

(a) (b) (c)

Figure 4: Process of going from (a) optical image to (b) binary image and (c) isolating proeutectic Si grain of interest for 30-µm-diameter beam simulation.

4.1 Compositional Homogenization

The ability of the model to accurately capture the compositional homogenization that occurs during the remelting process was verified by energy dispersive x-ray spectroscopy (EDS) surface mapping (Figures 5a and 5b). With respect to the laser scanning direction, the area directly before a Si grain shows an increase in intensity of Si. This area correlates to the darker areas seen in the reflected light images of

Figures 3b and 3d. The simulated regions (Figures 5b and 5d) accurately capture the presence of an area of higher Si concentration immediately before the Si grain for both beam diameters (Figures 5a and 5c).

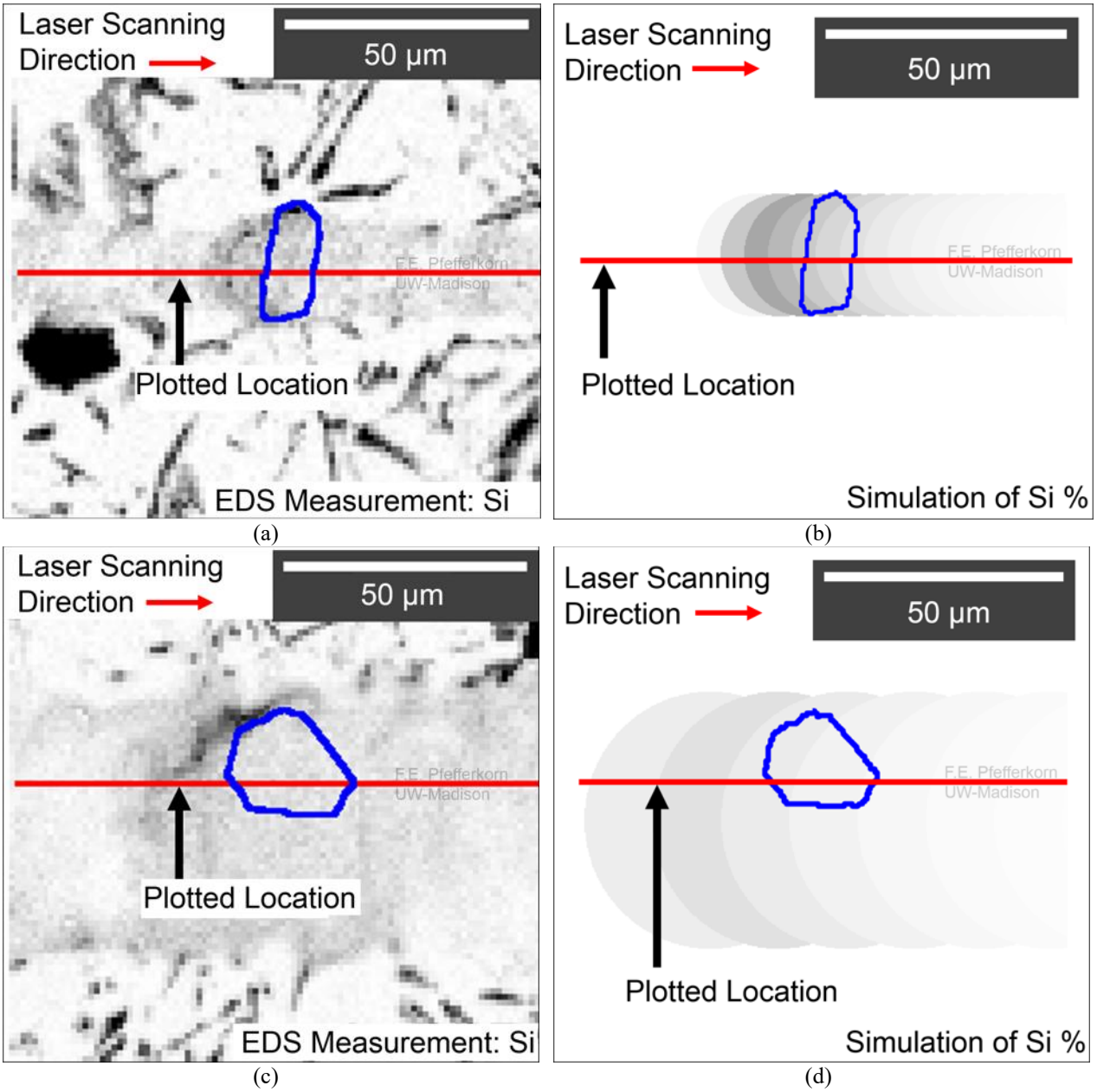

Figure 5: Energy dispersive x-ray spectroscopy maps of Si concentration after pulsed laser remelting with a single line scan: (a) 30-µm-diameter beam real surface, (b) 30-µm-diameter beam simulated surface, (c) 100-µm-diameter beam real surface, and (d) 100-µm-diameter simulated surface.

From plots extracted from the EDS surface maps of Figure 5 a peak in the Si concentration for both the experimental (Figures 6a and 6c) and simulated results (Figures 6b and 6d) is observed to be immediately before the region containing the Si grain. The simulation again shows good agreement with

the relative intensity, rise in concentration, and decay in compositional concentration for both the 30-µm-diameter beam and 100-µm-diameter beam cases. As the 100-µm-diameter beam simulation is averaging the composition across the entire melt pool, a lower peak in Si concentration is observed compared to the 30 µm beam. This lower peak is also observed in the experimental results comparing the 30-µm-diameter beam and 100-µm-diameter beam cases. After the Si concentration peaks, a decay in Si content back to the baseline level is observed. Because a single grain is being simulated for both beam diameters, the baseline composition that the line will decay back to will be 0% Si. As A384 contains between 10.5% and 12.0% Si and homogenization of Si is observed during laser remelting, a simulation baseline between these concentrations would be closer to those observed experimentally.

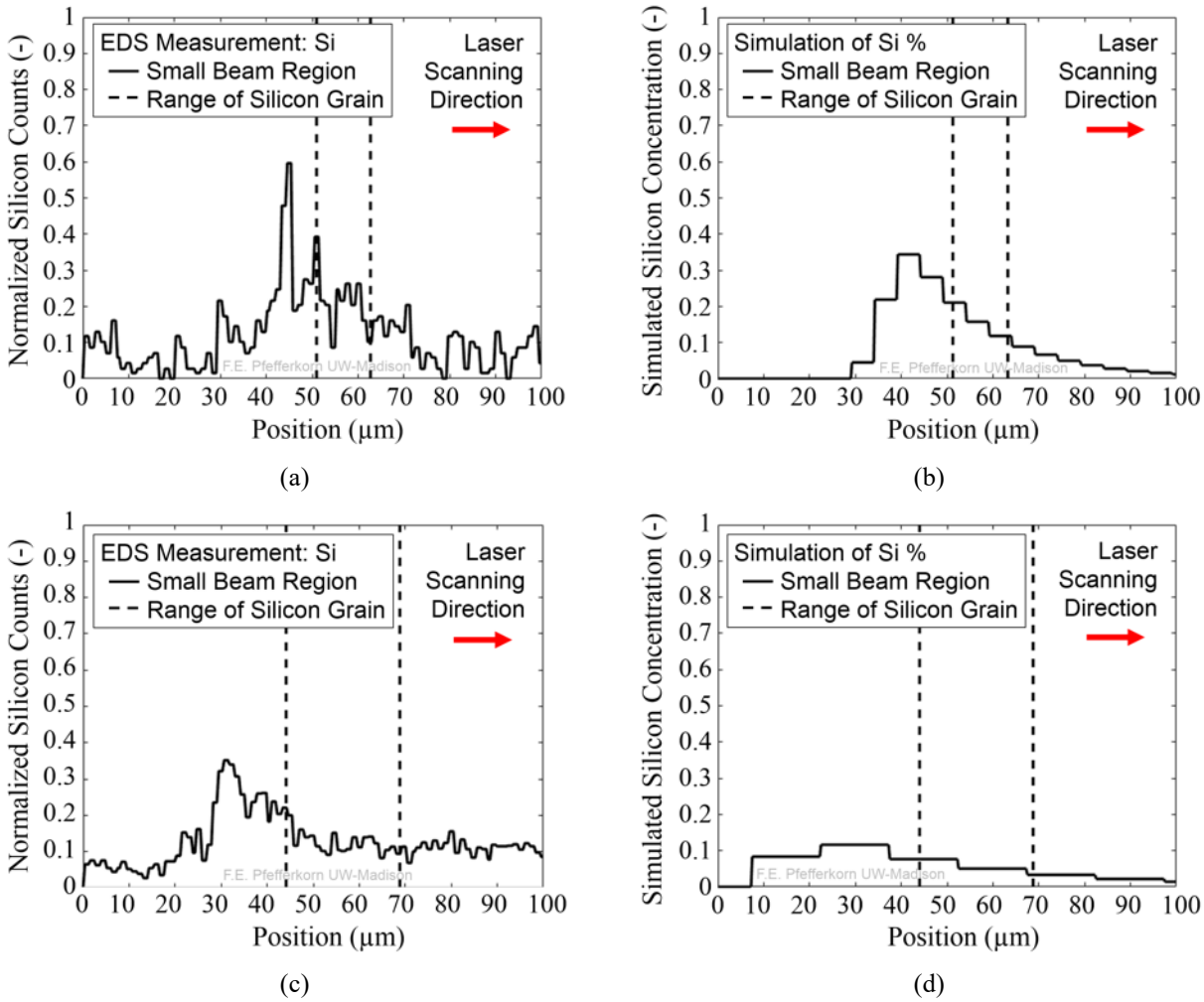

Figure 6: Composition plots from energy dispersive x-ray spectroscopy maps for: (a) 30-µm-diameter-beam experimental surface, (b) 30-µm-diameter-beam simulated surface, (c) 100-µm-diameter-beam experimental surface,

and (d) 100-µm-diameter-simulated surface.

4.2 Surface Height Profile

Height maps of the remelted lines were collected using a white-light interferometer and compared to the results predicted with the remelting simulation (Figures 7 and 8). In both experimental cases, a protuberance and then corresponding depression in the surface can be seen near the Si grain (Figures 7a and 7c). That is believed to be due to thermocapillary flow differences occurring due to the Si grains absorbing significantly more energy than the Al-rich matrix. That protuberance and depression is accurately captured in the simulation for both remelting conditions, suggesting that the primary physics governing this phenomenon has been accurately captured (Figures 7b and 7d).

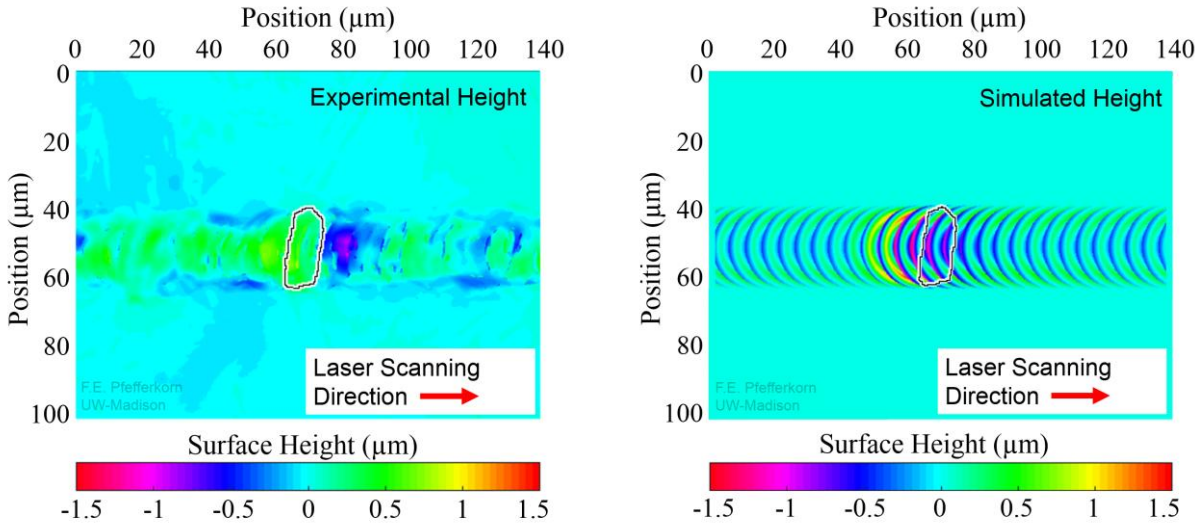

(a) (b)

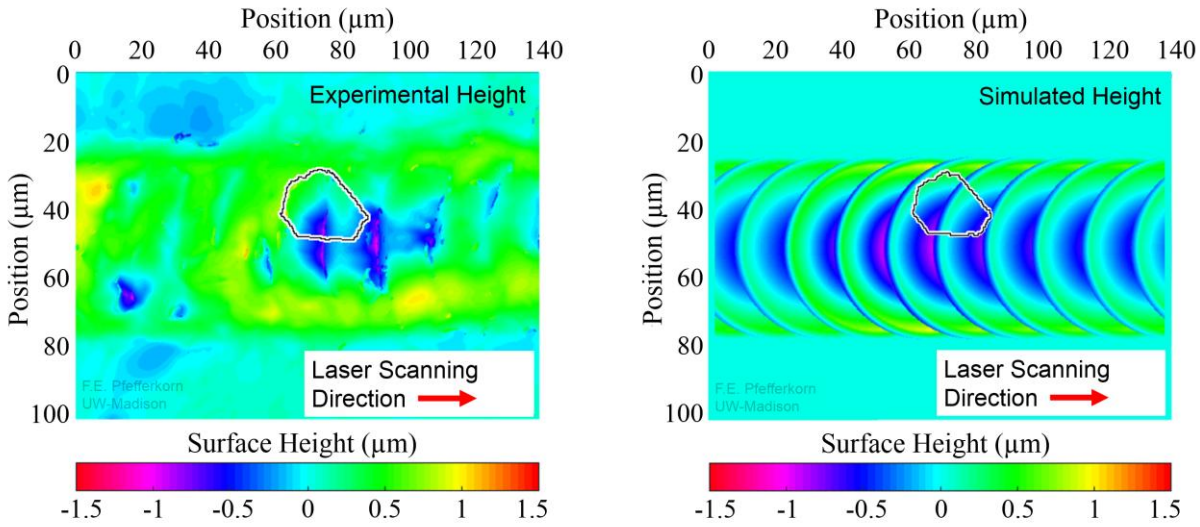

(c) (d)

Figure 7: Surface maps of (a) 30-µm-diameter beam (25-µm-diameter melt pool) experimental surface, (b) 30-µm-diameter beam simulated surface, (c) 100-µm-diameter beam (55-µm-diameter melt pool) experimental surface, and (d) 100-µm-diameter-simulated surface.

The corresponding heights in the middle of the remelted lines have been extracted and plotted with the location of the Si precipitates outlined (Figure 8).

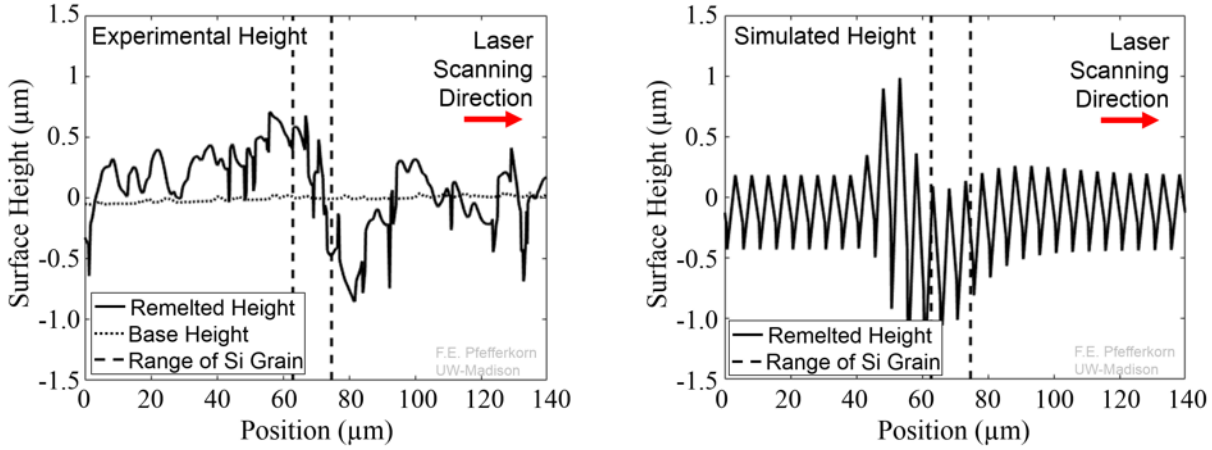

(a) (b)

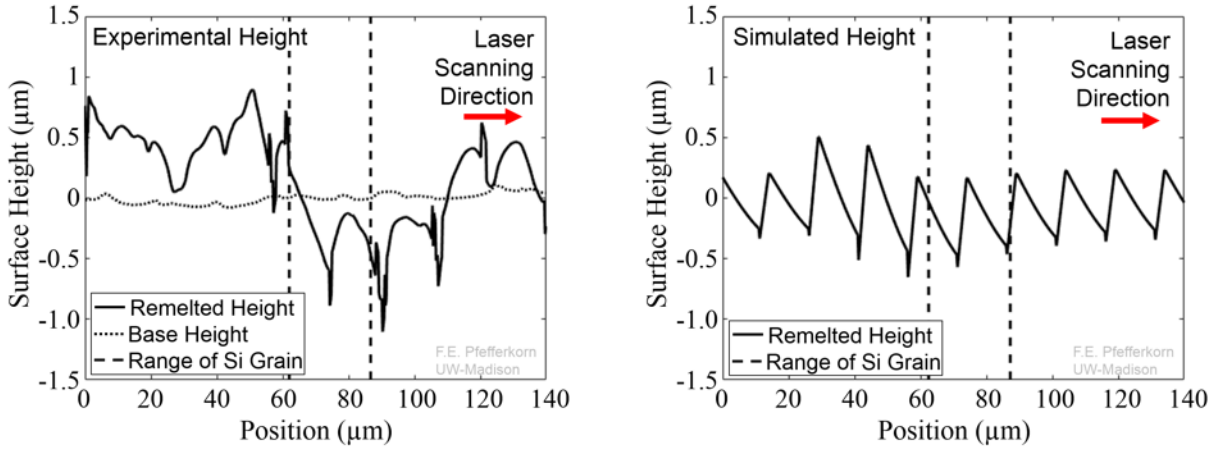

(c) (d)

Figure 8: Height plots of (a) 30-µm-diameter-beam experimental surface, (b) 30-µm-diameter-beam simulated surface, (c) 100-µm-diameter-beam experimental surface, and (d) 100-µm-diameter-simulated surface.

The experimental and simulated height plots from the middle of the remelted regions show the magnitudes of the protuberances and depressions. Both experimental conditions experienced protuberances of approximately 0.5-1.0 µm in height, and depressions of magnitude 0.5-1.0 µm (Figures 8a and 8c). The 30-µm-diameter beam simulation predicts protuberance and depressions of ~1.0 µm, while the 100-µm-diameter beam predicts protuberances and depressions of approximately 0.5 µm (Figures 8b and 8d). The simulated plots have a very consistent appearance while the experimental plot has a more stochastic nature. This may be due to the simulation only considering a single proeutectic Si grain when the remelted region inevitably contains eutectic Si precipitates. Additionally, the simulations predict that the depression occurs slightly before the location of the grain, while the experiments show this occurs after the grain.

5. Prediction of Laser Area Remelting

To demonstrate how the model captures the remelting of an area, a subsection of a 1 mm x 1 mm region that was remelted with the 30-µm-diameter beam is compared to a simulated area scan (Figure 9).

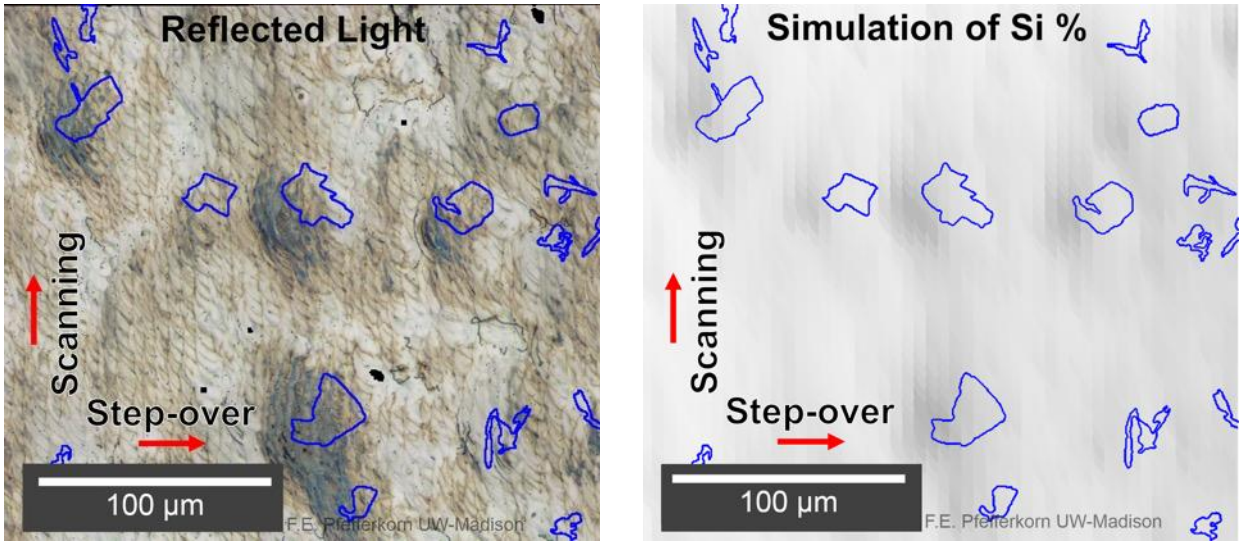

(a) (b)

Figure 9: (a) Optical image of experimental surface and (b) composition map following homogenization model from 30-µm-diameter-beam processing.

Within the experimental remelted region shown in Figure 9a there are dark regions that correlate to the locations of the large Si grains within the surface. This is similar to what was seen in the remelted lines, and it can be inferred from these results that these regions will also contain a higher percentage of Si. Qualitatively, the reflected light image of the surface matches well to the simulated composition map (Figure 9b). In a height map of the remelted region, these dark regions correlate with elevated features (Figure 10).

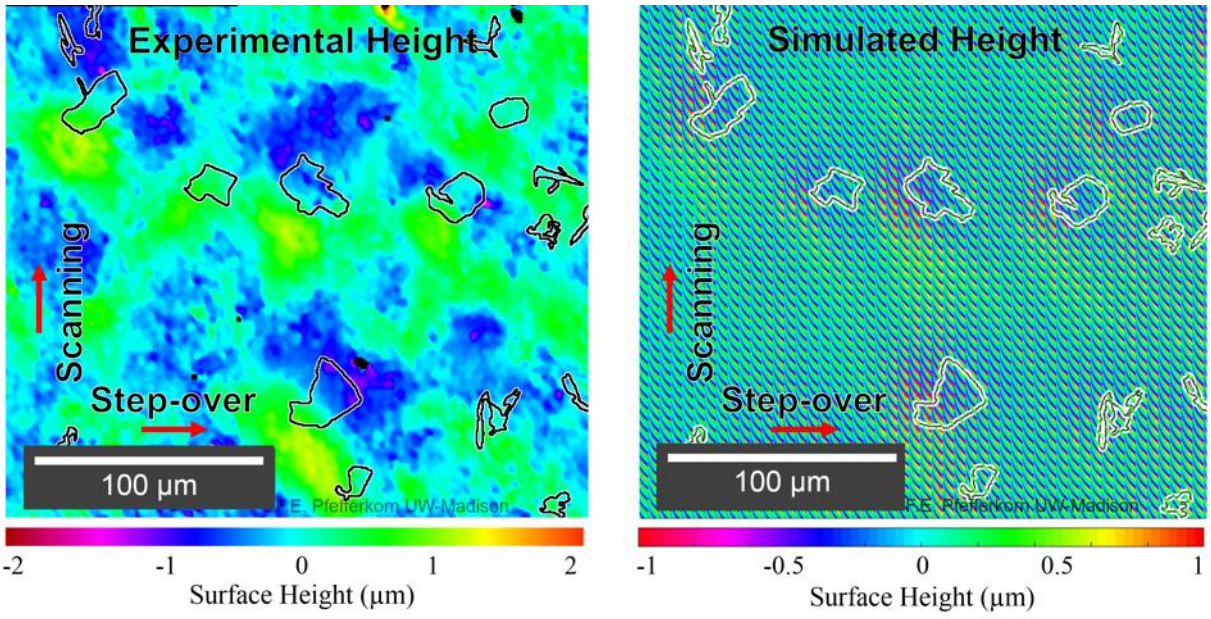

(a) (b)

Figure 10: Surface height maps after pulsed laser remelting using 30-µm-diameter-beam processing: (a) experimentally measured surface and (b) simulated surface. The differences in scale should be noted.

The remelting was done on a mechanically polished surface, hence there were no roughness features of the magnitude seen in Figure 10 prior to pulsed laser remelting. The features in Figure 10 were created by the remelting process. The proximity of the proeutectic Si grains to height protuberances and depressions on the surface indicates that those Si grains are a contributor to the features observed on the remelted surfaces. The simulation of pulsed laser remelting in the region also displays similar protuberances and depressions that were generated due to the higher concentrations of Si in those regions causing larger thermocapillary features. To better highlight the generated features, a filter was applied to the experimental and simulated surfaces of Figure 10 to show the underlying waviness (shown in Figure 11). The roughness-waviness cutoff frequency used was 33.3 mm^{-1}, which was the frequency of the laser beam's diameter. This value was chosen to remove features present in the individual melt pools, while leaving out generated features larger than the beam itself.

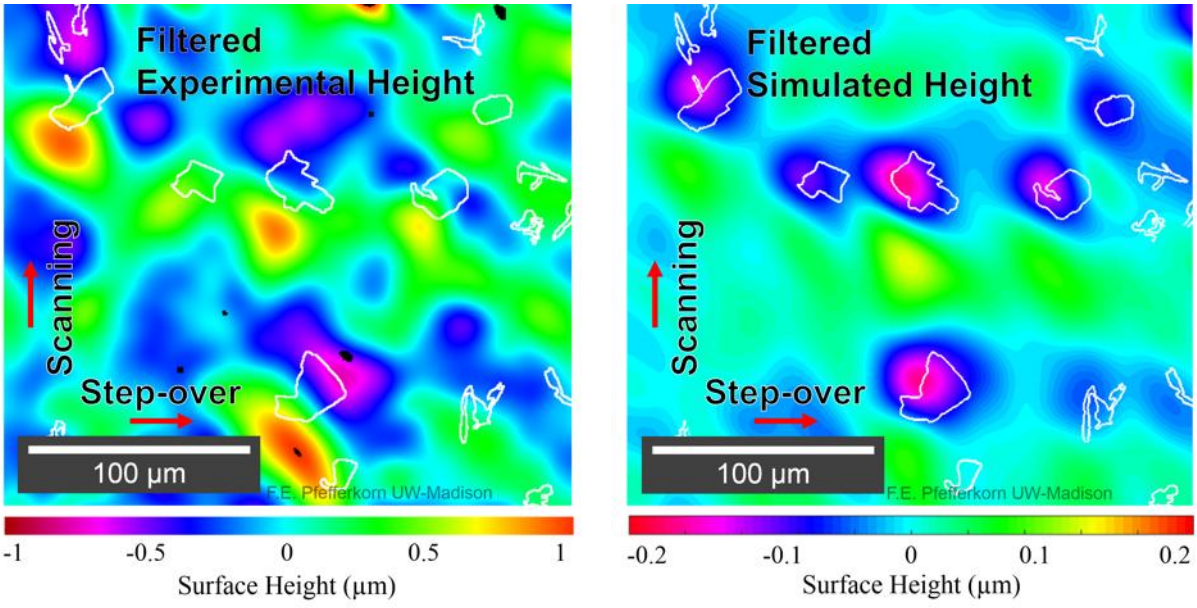

(a) (b)

Figure 11: Waviness after pulsed laser remelting using 30-µm-diameter-beam processing: (a) experimentally measured surface and (b) waviness of simulated surface using cutoff frequencies of 33.3 mm^{-1}. The differences in scale should be noted.

As in the case of remelted lines, protuberances and depressions occur near the large Si precipitates but with protuberances occurring in the direction opposite of both the scan and step-over directions. The simulation shifts the protuberance and depression further away from the grains than that observed experimentally, but the relative magnitude of the surface features to each other within the experimental or simulated region is similar. The filtered surface helps demonstrate this: the locations with the largest protuberances & depressions are the same in both, even though their magnitude is different (Figure 11). This demonstrates the model's ability to capture the primary physics occurring during pulsed laser remelting of heterogeneous surfaces. One reason for the difference in magnitude and location of the protuberances & depressions may be due to assumption that the generated thermocapillary feature is uniform across a single melt event. Another reason for the difference may be due to treating the composition as averaging over an area rather than a volume, or the assumption that the flow difference is proportional to the ratio of laser absorptivity for Si and Al. However, even with those differences the roughness metrics of the unfiltered experimental surface and unfiltered simulated surface show good agreement (Table 3).

Table 3: Measured and Predicted Surface Roughness Metrics for Remelted Area (experimental values are an average of 6 measurements)

	Experimental Observation	**Simulation**
Average Roughness (S_a)	251 nm ± 38 nm	253 nm
Maximum Roughness (S_z)	2.69 µm ± 0.40 µm	2.36 µm

6. Conclusions

A model has been proposed that simulates pulsed laser remelting in a spot-by-spot (line scan) fashion. This model was verified through comparisons of experimentally measured surface composition and height (topography) profiles created with two different laser beam (melt pool) diameters (30 µm and 100 µm) on an Al casting alloy (A384) which has a heterogeneous starting chemical composition. The predicted distributions of Si and surface topographic features were consistent with those measured experimentally. The model was then expanded and shown to work for the prediction of area remelting. There was good

qualitative agreement between the model and experimental observations suggesting that the primary process physics were captured.

It was found that proeutectic and eutectic Si precipitates were redistributed during laser remelting by spreading out in the direction of beam travel. However, perfect homogenization of Si during remelting of lines and areas did not occur, nor was predicted. By assuming, for modeling purposes, perfect mixing during each individual melt event, the primary process by which Si is redistributed during laser remelting was accurately simulated. The prediction of larger area redistribution (*i.e.,* when remelted lines overlap each other) was also demonstrated. This indicates that laser path planning and the use of a model such as the one presented may help achieve the maximum possible homogenization.

The model predicted the topographical features generated during laser remelting by using the ratio of laser absorptivity (for 1070-nm-wavelength light) for Si and Al and the law of mixtures to estimate the amount of Si within a given area. The variation in thermocapillary flow during individual melt events were predicted and used to qualitatively account for the height variations that occur and their relation to composition variation in the starting surface. Large Si precipitates present in the surface induced material displacement in the direction opposite of the laser beam travel direction. This caused a protuberance and corresponding depression in the surface height relative to the base surface. The protuberance occurred at a location in front of the original location of the Si precipitate and the depression is located approximately where the Si precipitate was. This demonstrates that starting surface composition heterogeneity can cause surface topography changes during laser remelting.

Acknowledgements

This work was partially supported by the U.S. National Science Foundation (NSF) grant CMMI-1462295, LasX Industries, Inc., and NSF-supported shared facilities at the University of Wisconsin – Madison.

References

[1] Kou S, Wang YH. Three-dimensional convection in laser melted pools. MTA 1986;17:2265–70. doi:10.1007/BF02645924.

[2] Chande T, Mazumder J. Two-dimensional, transient model for mass transport in laser surface alloying. Journal of Applied Physics 1985;57:2226–32. doi:10.1063/1.334367.

[3] Qi H, Mazumder J, Ki H. Numerical simulation of heat transfer and fluid flow in coaxial laser cladding process for direct metal deposition. Journal of Applied Physics 2006;100:024903. doi:10.1063/1.2209807.

[4] Chan CL, Mazumder J, Chen MM. Effect of surface tension gradient driven convection in a laser melt pool: Three-dimensional perturbation model. Journal of Applied Physics 1988;64:6166–74. doi:10.1063/1.342121.

[5] Sudnik W, Radaj D, Breitschwerdt S, Erofeew W. Numerical simulation of weld pool geometry in laser beam welding. J Phys D: Appl Phys 2000;33:662. doi:10.1088/0022-3727/33/6/312.

[6] Kim Y-D, Kim W-S. A numerical analysis of heat and fluid flow with a deformable curved free surface in a laser melting process. International Journal of Heat and Fluid Flow 2008;29:1481–93. doi:10.1016/j.ijheatfluidflow.2008.06.009.

[7] Leech PW. The laser surface melting of aluminum-silicon-based alloys. Thin Solid Films 1989;177:133–40. doi:10.1016/0040-6090(89)90562-2.

[8] Wong TT, Liang GY. Effect of laser melting treatment on the structure and corrosion behaviour of aluminium and AlSi alloys. Journal of Materials Processing Technology 1997;63:930–4. doi:10.1016/S0924-0136(96)00098-2.

[9] Wong TT, Liang GY, Tang CY. The surface character and substructure of aluminium alloys by laser-melting treatment. Journal of Materials Processing Technology 1997;66:172–8. doi:10.1016/S0924-0136(96)02514-9.

[10] Tomida S, Nakata K, Shibata S, Zenkouji I, Saji S. Improvement in wear resistance of hyper-eutectic AlSi cast alloy by laser surface remelting. Surface and Coatings Technology 2003;169:468–71. doi:10.1016/S0257-8972(03)00100-2.

[11] Biswas A, Mordike BL, Manna I, Majumdar JD. Studies on laser surface melting of Al-11% Si alloy. Lasers in Engineering 2008;18:95.

[12] Osório WR, Cheung N, Peixoto LC, Garcia A, others. Corrosion resistance and mechanical properties of an Al 9wt% Si alloy treated by laser surface remelting. Int J Electrochem Sci 2009;4:820–831.

[13] Sušnik J, Šturm R, Grum J. Influence of Laser Surface Remelting on Al-Si Alloy Properties. Strojniški Vestnik - Journal of Mechanical Engineering 2012;58:614–20. doi:10.5545/sv-jme.2012.696.

[14] Tillová E, Kuchariková L, Chalupová M, Belan J, Vaško A, Švecová I. Influence of laser surface hardening on corrosion properties of Al-Zn-Si cast alloy. Metalurgija 2017;56:47–50.

[15] Ramos JA, Bourell DL. Modeling of surface roughness enhancement of indirect-SLS metal parts by laser surface polishing 2002:191–202.

[16] Willenborg E. Polishing by Laser Irradiation. Tailored Light 2: Laser Application Technology, Springer; 2011, p. 196–202.

[17] Mai TA, Lim GC. Micromelting and its effects on surface topography and properties in laser polishing of stainless steel. Journal of Laser Applications 2004;16:221–8. doi:10.2351/1.1809637.

[18] Ramos-Grez J a., Bourell D l. Reducing surface roughness of metallic freeform-fabricated parts using non-tactile finishing methods. International Journal of Materials and Product Technology 2004;21:297–316. doi:10.1504/IJMPT.2004.004944.

[19] Lamikiz A, Sánchez JA, Lacalle L de, Norberto L, del Pozo D, Etayo JM. Surface Roughness Improvement Using Laser-Polishing Techniques. Materials Science Forum 2006;526:217–22. doi:10.4028/www.scientific.net/MSF.526.217.

[20] Lamikiz A, Sanchez J a., De Lacalle LNL, Del Pozo D, Etayo J m., Lopez J m. Laser polishing techniques for roughness improvement on metallic surfaces. International Journal of Nanomanufacturing 2007;1:490–8. doi:10.1504/IJNM.2007.014568.
[21] Perry TL, Werschmoeller D, Li X, Pfefferkorn FE, Duffie NA. Pulsed laser polishing of micro-milled Ti6Al4V samples. Journal of Manufacturing Processes 2009;11:74–81. doi:10.1016/j.jmapro.2009.10.001.
[22] Vadali M, Ma C, Duffie NA, Li X, Pfefferkorn FE. Pulsed laser micro polishing: Surface prediction model. Journal of Manufacturing Processes 2012;14:307–15. doi:10.1016/j.jmapro.2012.03.001.
[23] Wang Q, Morrow JD, Ma C, Duffie NA, Pfefferkorn FE. Surface prediction model for thermocapillary regime pulsed laser micro polishing of metals. Journal of Manufacturing Processes 2015;20, Part 1:340–8. doi:10.1016/j.jmapro.2015.05.005.
[24] L. D. Landau & E.M. Lifshitz. Fluid Mechanics. n.d.
[25] Ma C, Vadali M, Li X, Duffie NA, Pfefferkorn FE. Analytical and Experimental Investigation of Thermocapillary Flow in Pulsed Laser Micropolishing. Journal of Micro and Nano-Manufacturing 2014;2:021010–021010. doi:10.1115/1.4027433.
[26] Bordatchev EV, Hafiz AMK, Tutunea-Fatan OR. Performance of laser polishing in finishing of metallic surfaces. The International Journal of Advanced Manufacturing Technology 2014;73:35–52. doi:10.1007/s00170-014-5761-3.
[27] Schmidt J, Scholz R, Riegel H. Laser polishing of aluminum by remelting with high energy pulses. Materialwissenschaft Und Werkstofftechnik 2015;46:686–91. doi:10.1002/mawe.201500318.
[28] Burzic B, Hofele M, Mürdter S, Riegel H. Laser polishing of ground aluminum surfaces with high continuous wave laser. Journal of Laser Applications 2016;29:011701. doi:10.2351/1.4966923.
[29] Schanz J, Hofele M, Hitzler L, Merkel M, Riegel H. Laser Polishing of Additive Manufactured AlSi10Mg Parts with an Oscillating Laser Beam. Machining, Joining and Modifications of Advanced Materials 2016:159–69. doi:10.1007/978-981-10-1082-8_16.
[30] Kaufman JG, Rooy EL. Aluminum Alloy Castings: Properties, Processes, and Applications. ASM International; 2004.
[31] Warmuzek M. ASM Handbooks: Volume 9, Metallographic Techniques for Aluminum and its Alloys, Composition and Phases. vol. 9. ASM International; 2004.
[32] Ordal MA, Bell RJ, Alexander RW, Newquist LA, Querry MR. Optical properties of Al, Fe, Ti, Ta, W, and Mo at submillimeter wavelengths. Appl Opt, AO 1988;27:1203–9. doi:10.1364/AO.27.001203.
[33] Green MA, Keevers MJ. Optical properties of intrinsic silicon at 300 K. Prog Photovolt: Res Appl 1995;3:189–92. doi:10.1002/pip.4670030303.
[34] Kearney AL. ASM Handbooks: Volume 2, Properties and Selection: Nonferrous Alloys and Special-Purpose Materials, Properties of Cast Aluminum Alloys. vol. 2. ASM International; 1990.
[35] Schneider CA, Rasband WS, Eliceiri KW. NIH Image to ImageJ: 25 years of image analysis. Nat Meth 2012;9:671–5. doi:10.1038/nmeth.2089.
[36] Schindelin J, Arganda-Carreras I, Frise E, Kaynig V, Longair M, Pietzsch T, et al. Fiji: an open-source platform for biological-image analysis. Nat Meth 2012;9:676–82. doi:10.1038/nmeth.2019.
[37] Ma C, Vadali M, Duffie NA, Pfefferkorn FE, Li X. Melt Pool Flow and Surface Evolution During Pulsed Laser Micro Polishing of Ti6Al4V. J Manuf Sci Eng 2013;135:061023–061023. doi:10.1115/1.4025819.

Figure 1 - color

Click here to download high resolution image

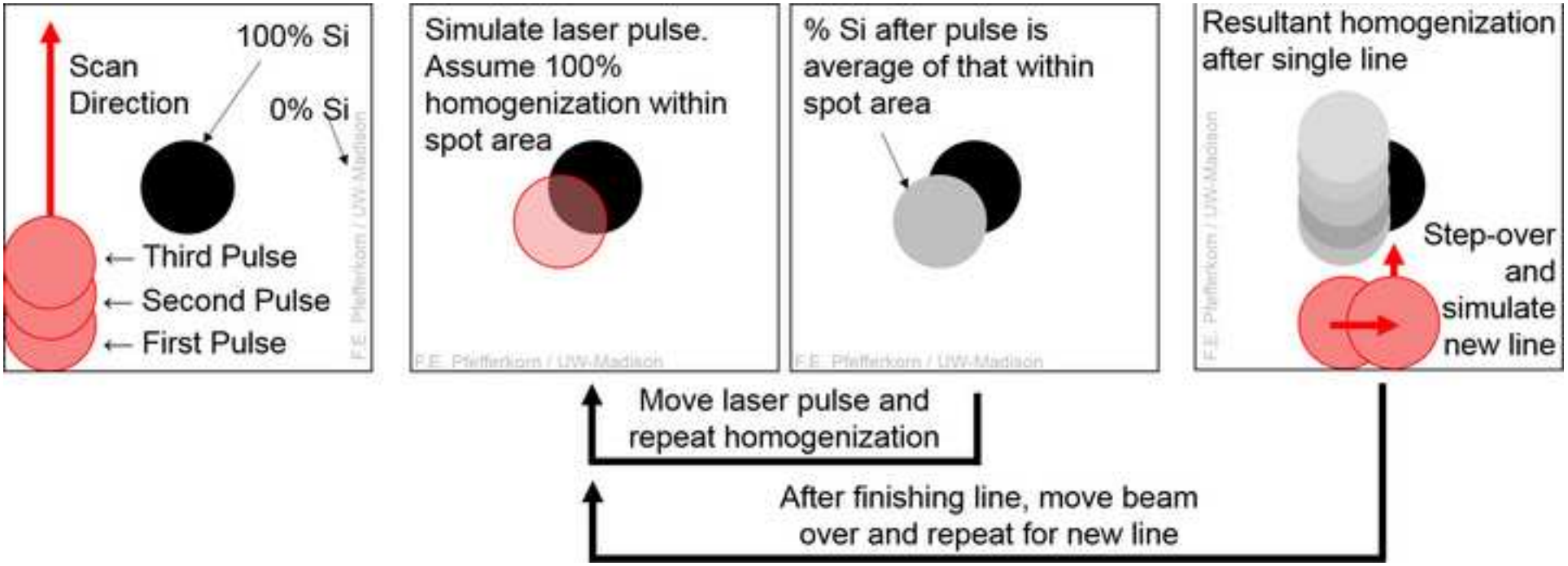

Figure 2a - color
Click here to download high resolution image

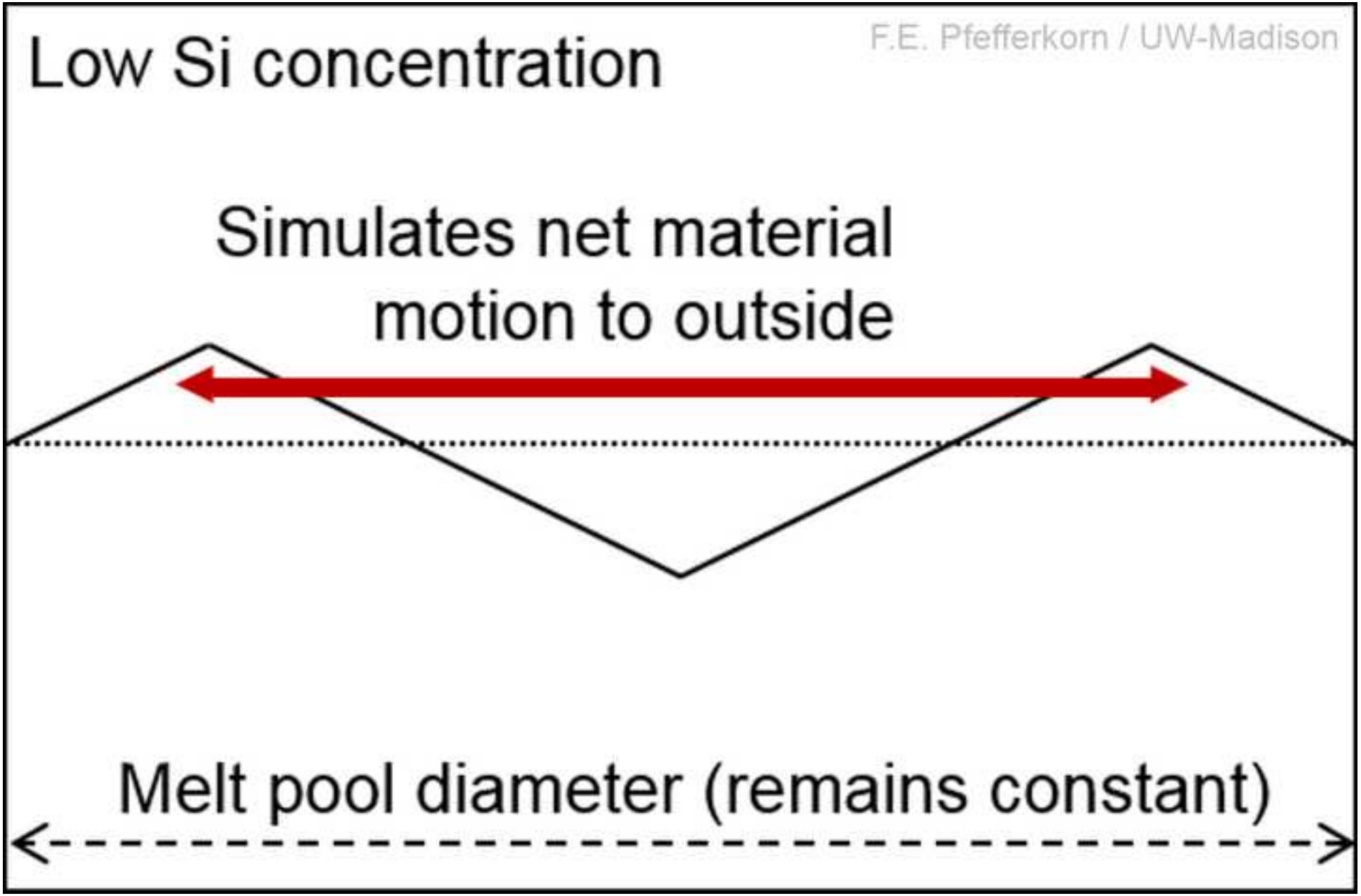

Figure 2b
Click here to download high resolution image

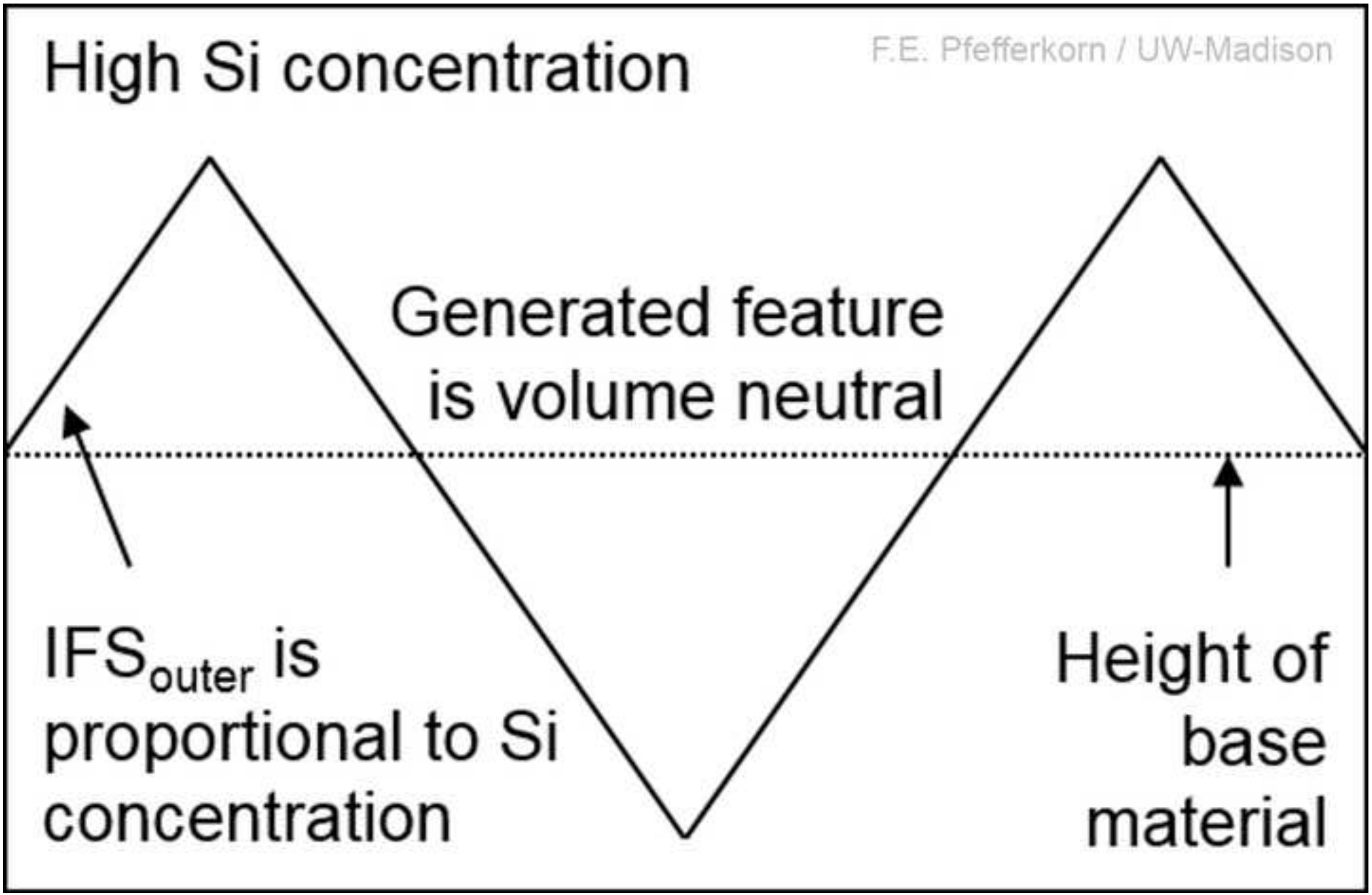

Figure 2c - color

Click here to download high resolution image

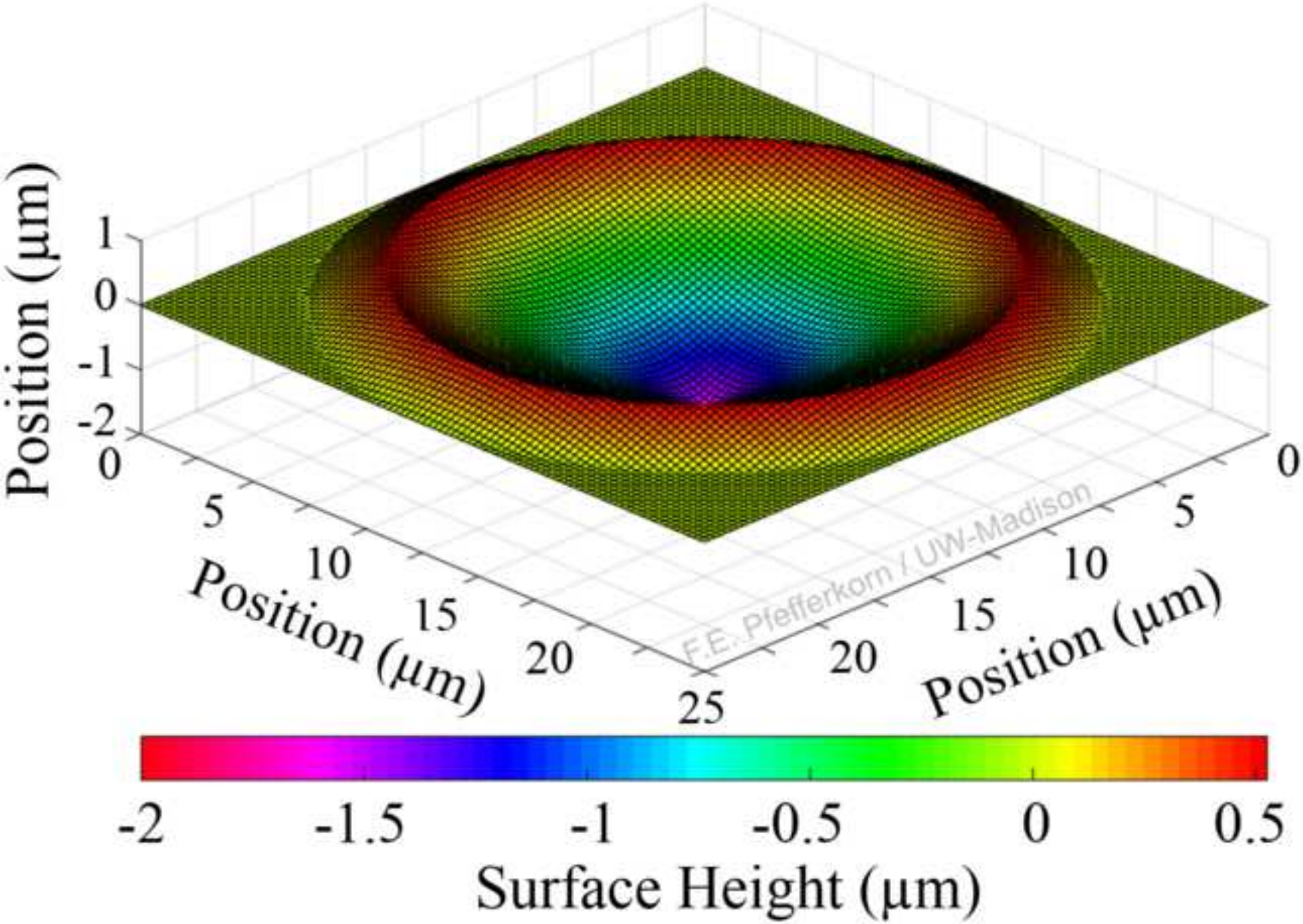

Figure 3ab - color

Click here to download high resolution image

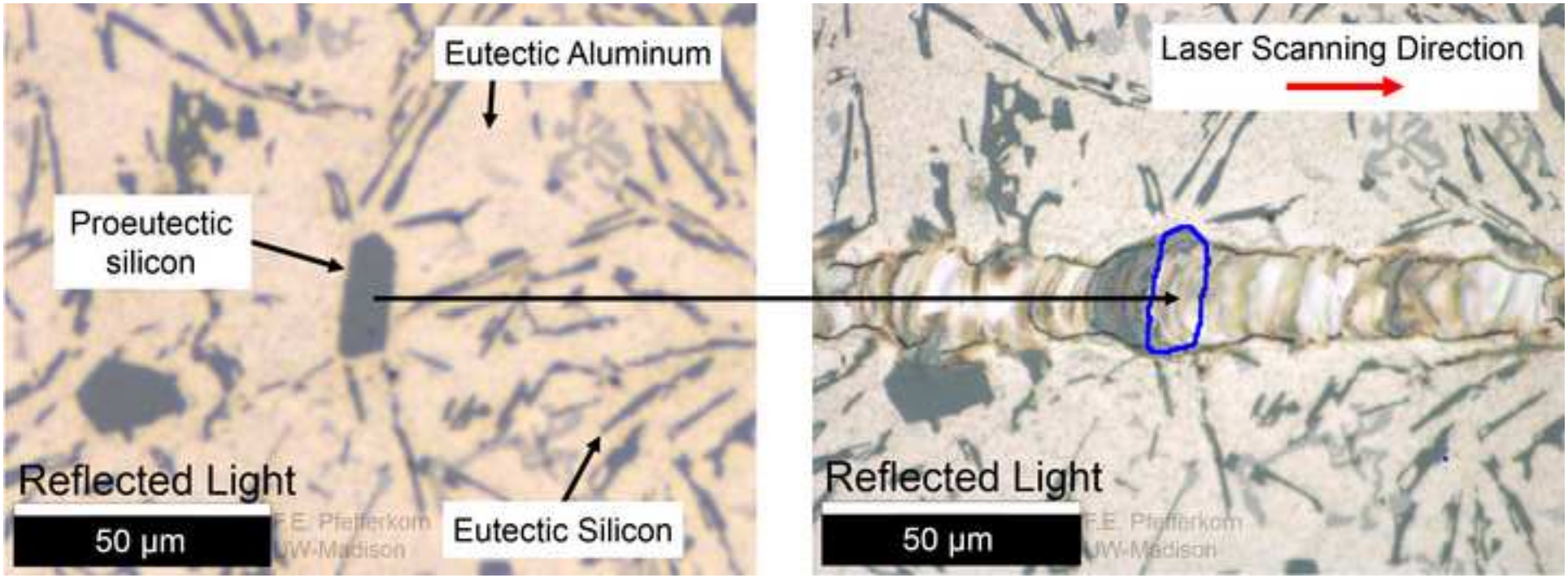

Figure 3cd - color

Click here to download high resolution image

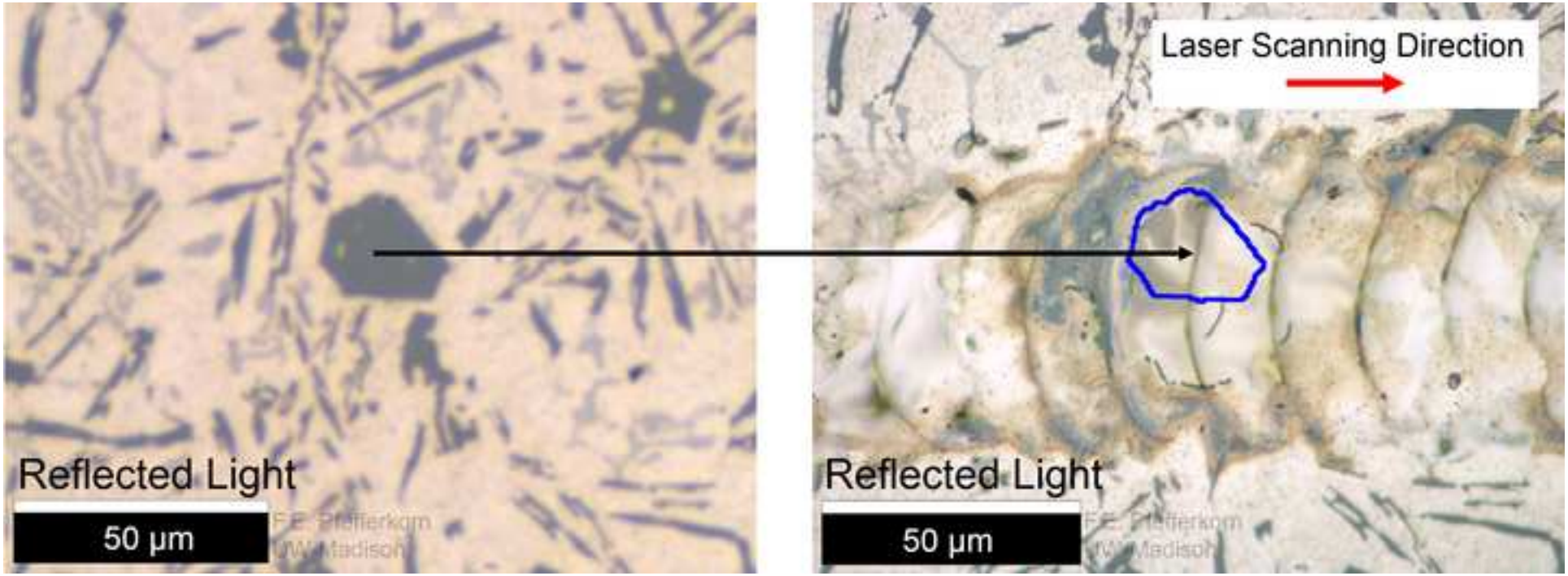

Figure 4a - color

Click here to download high resolution image

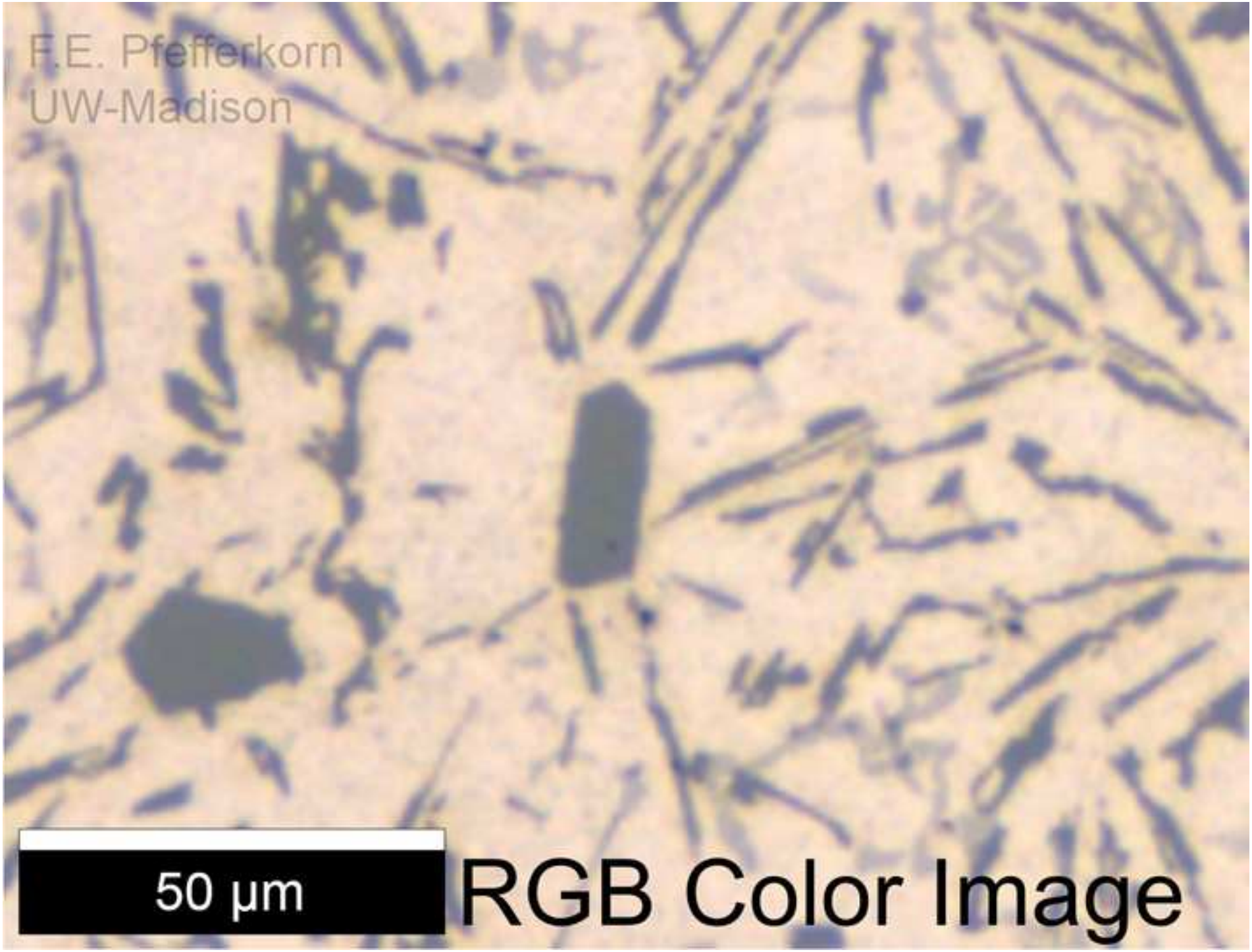

Figure 4b
Click here to download high resolution image

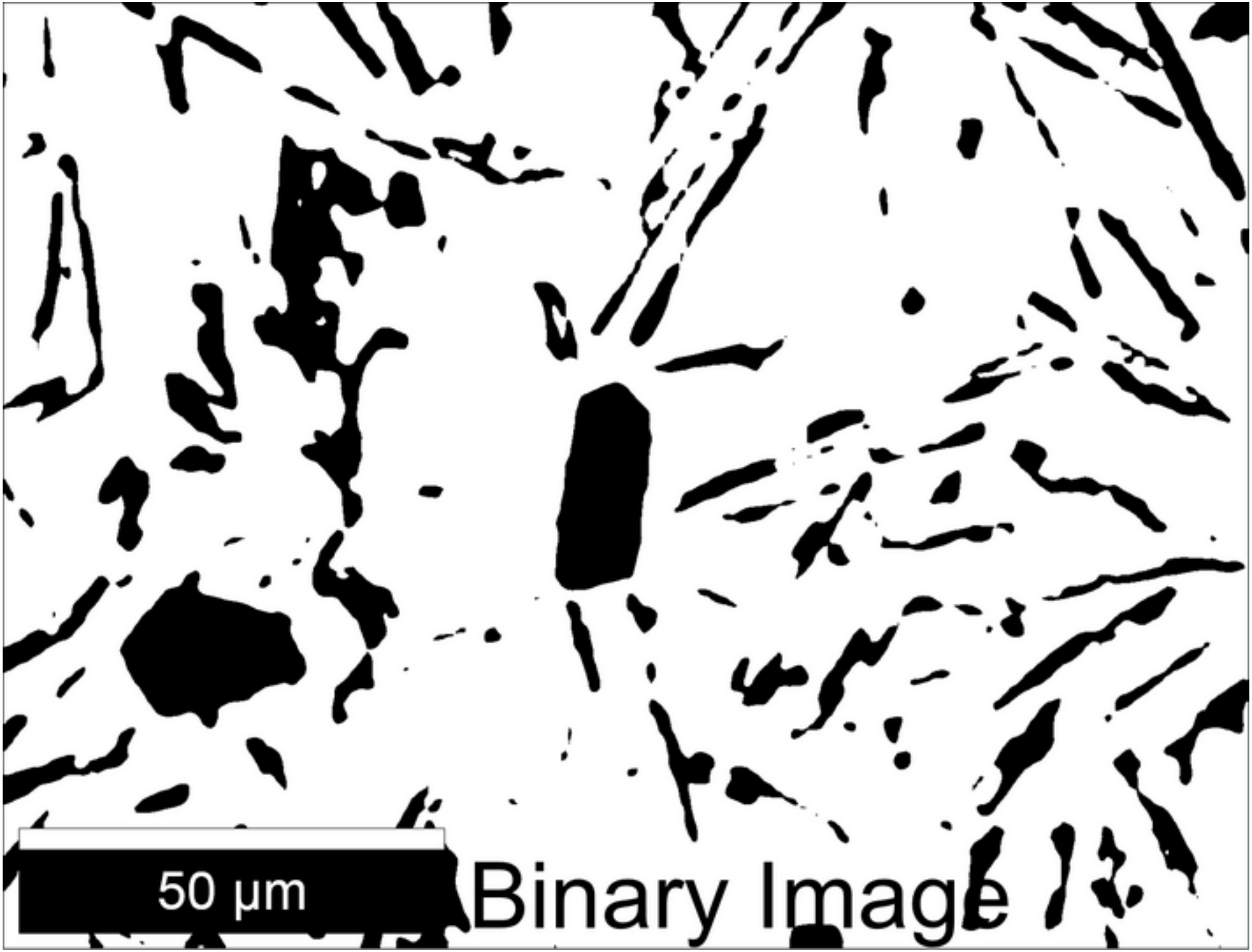

Figure 4c

Click here to download high resolution image

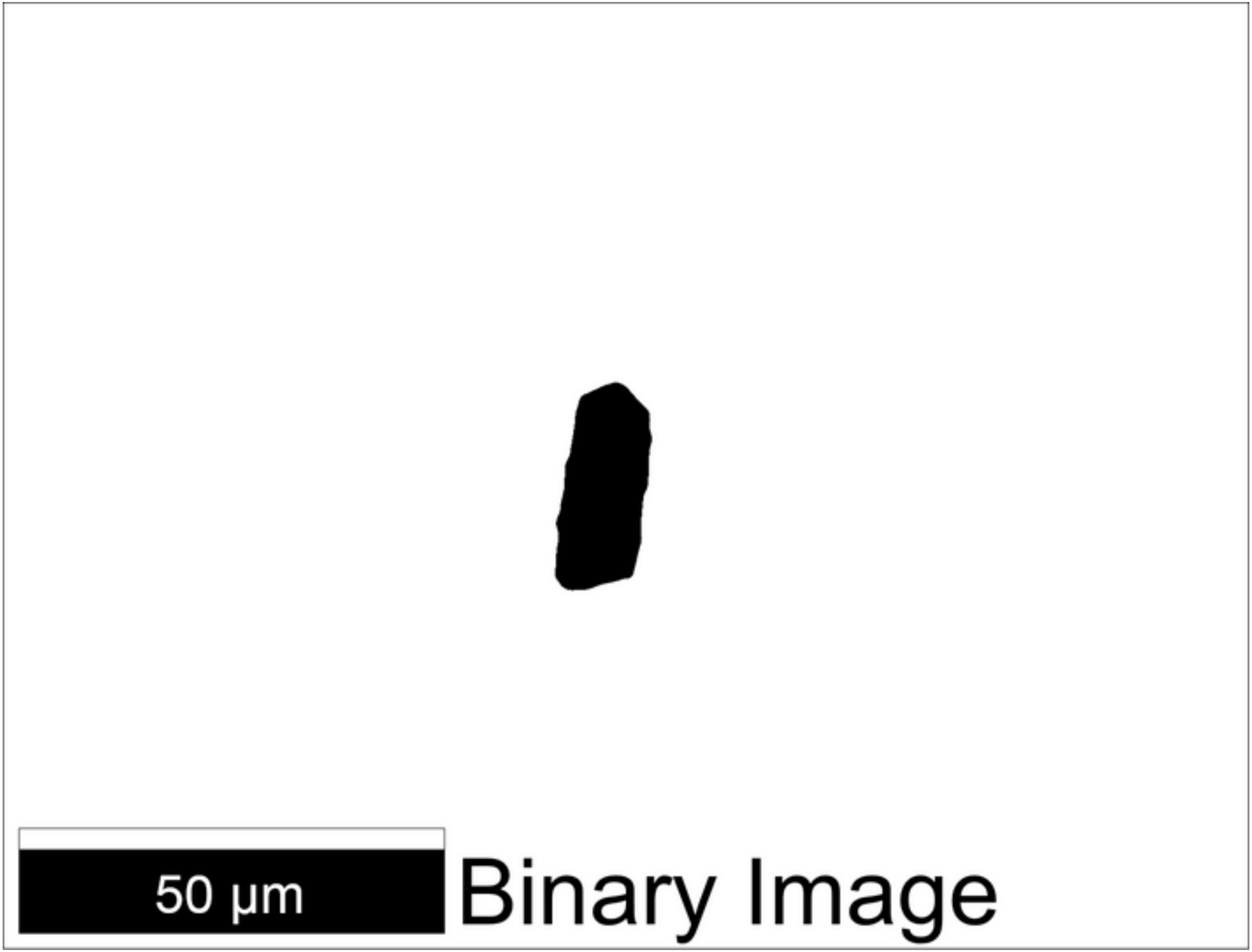

Figure 5a - color

Click here to download high resolution image

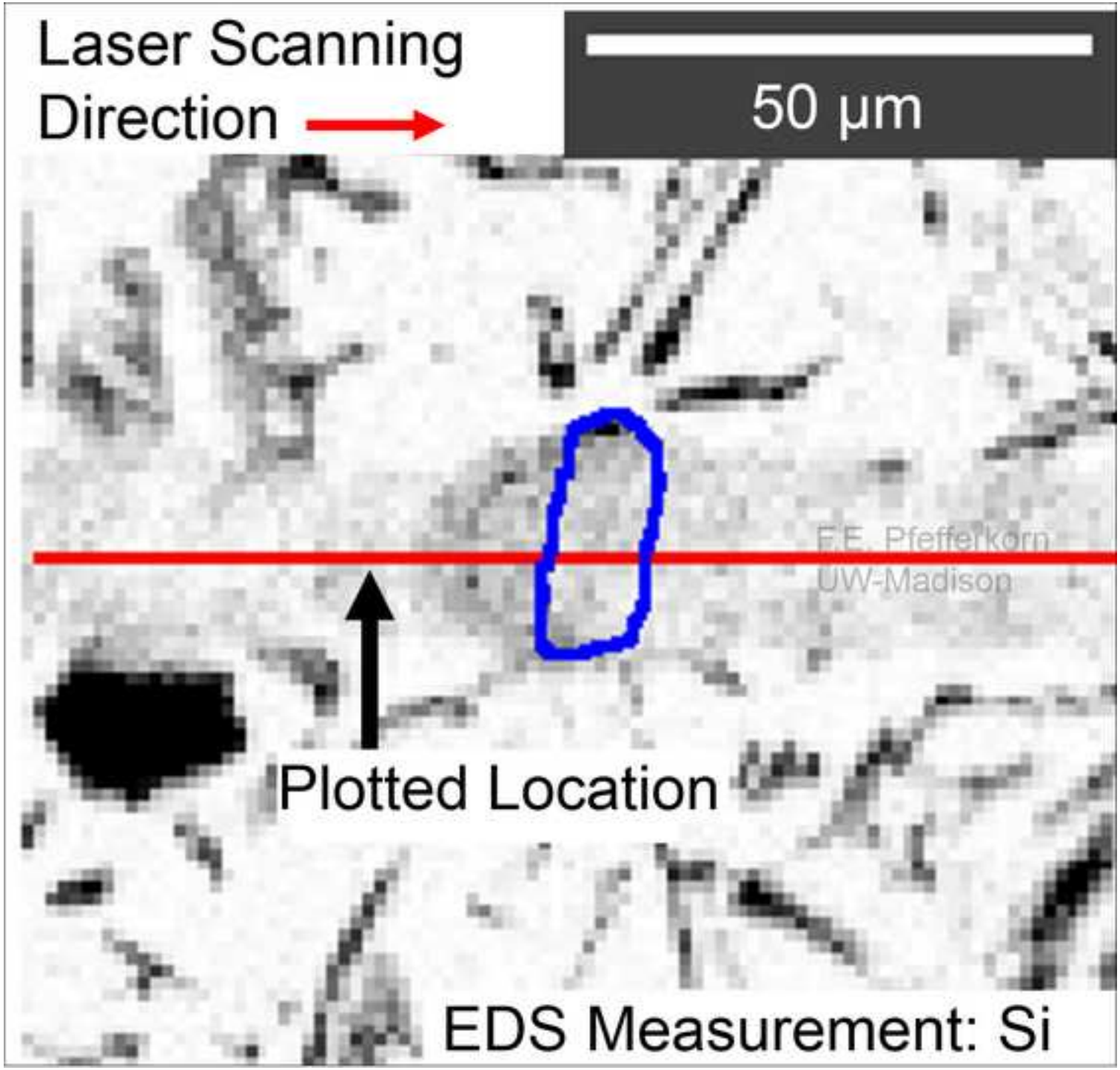

Figure 5b - color
Click here to download high resolution image

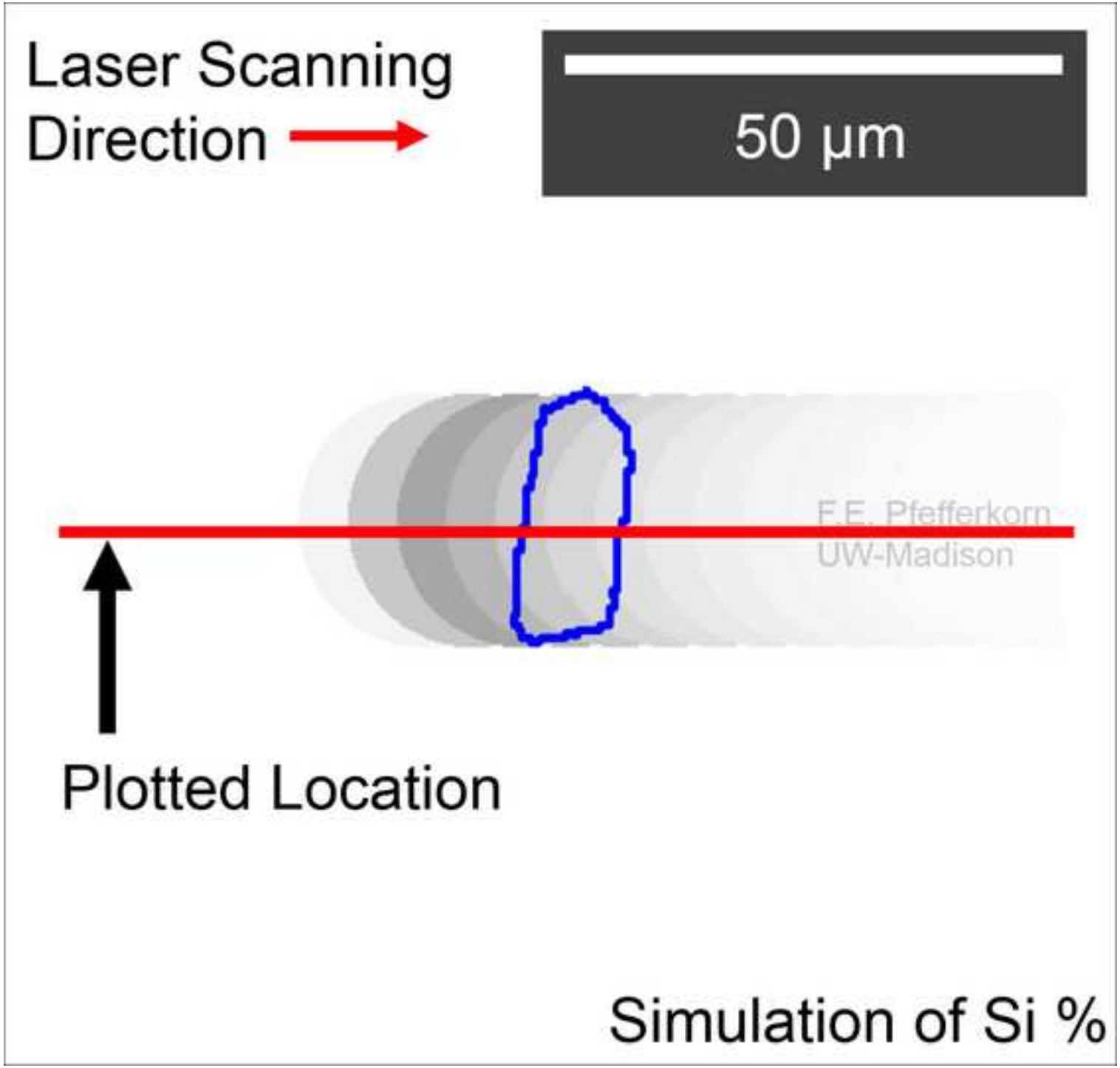

Figure 5c - color

Click here to download high resolution image

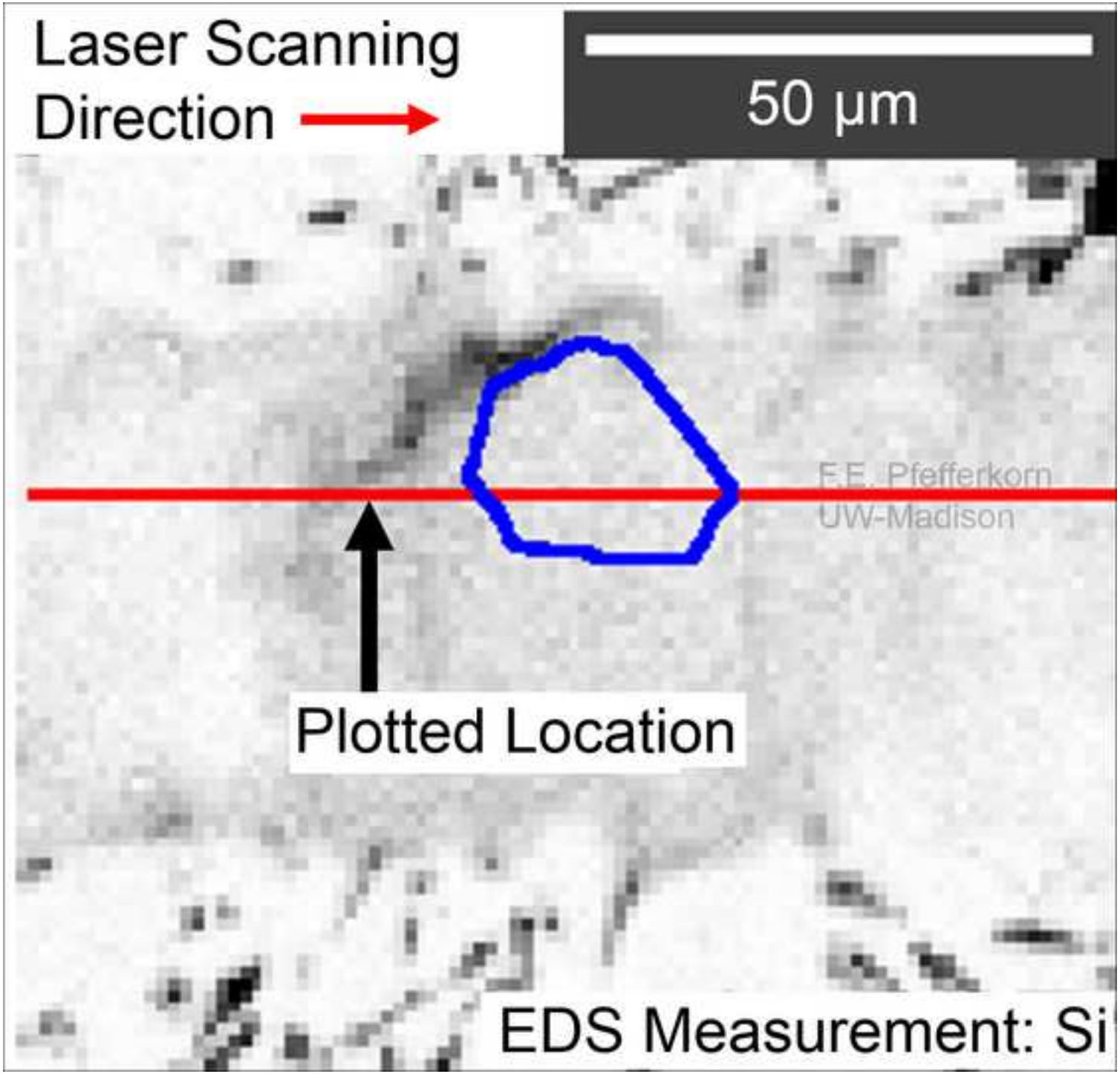

Figure 6a - color

Click here to download high resolution image

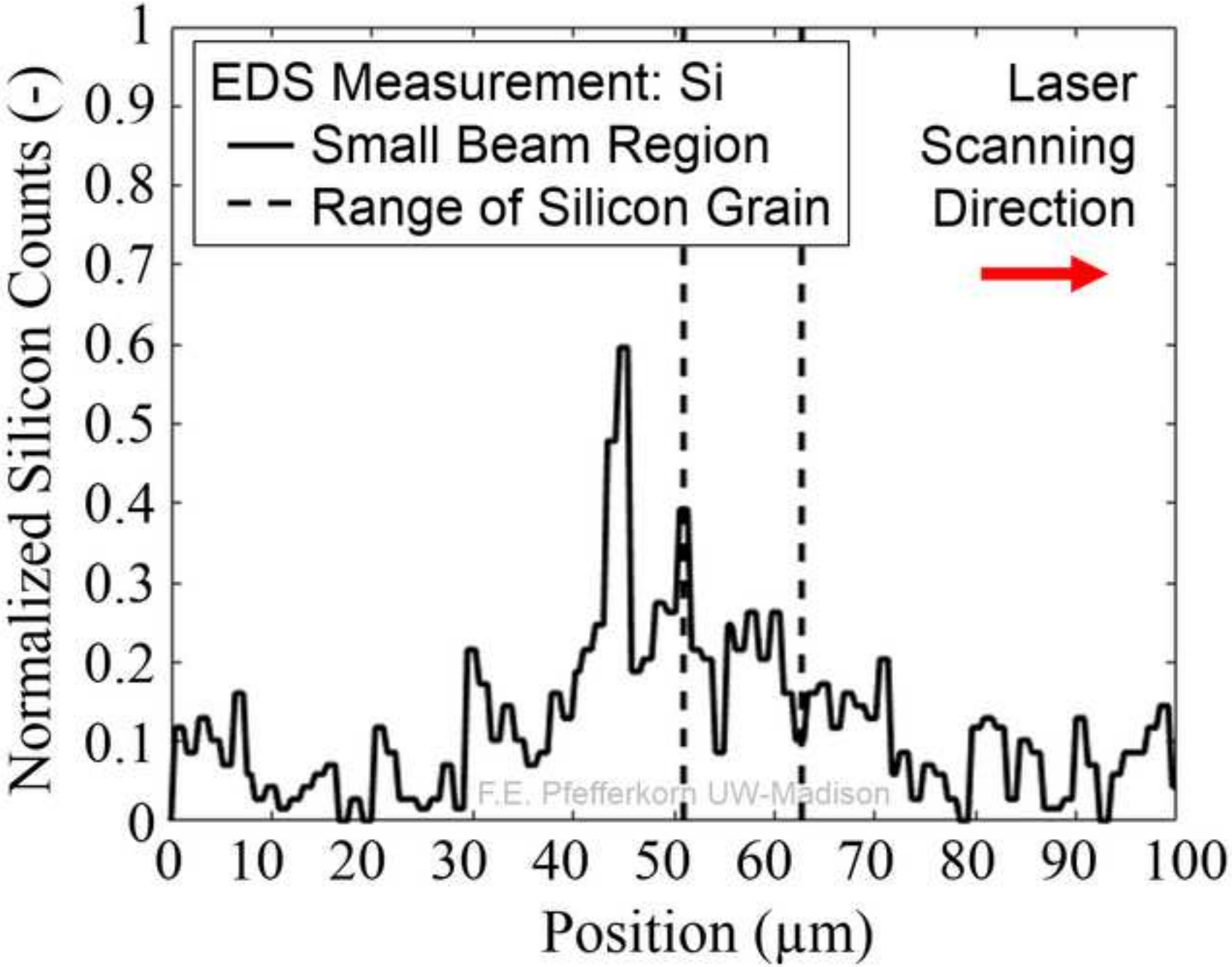

Figure 6b - color

Click here to download high resolution image

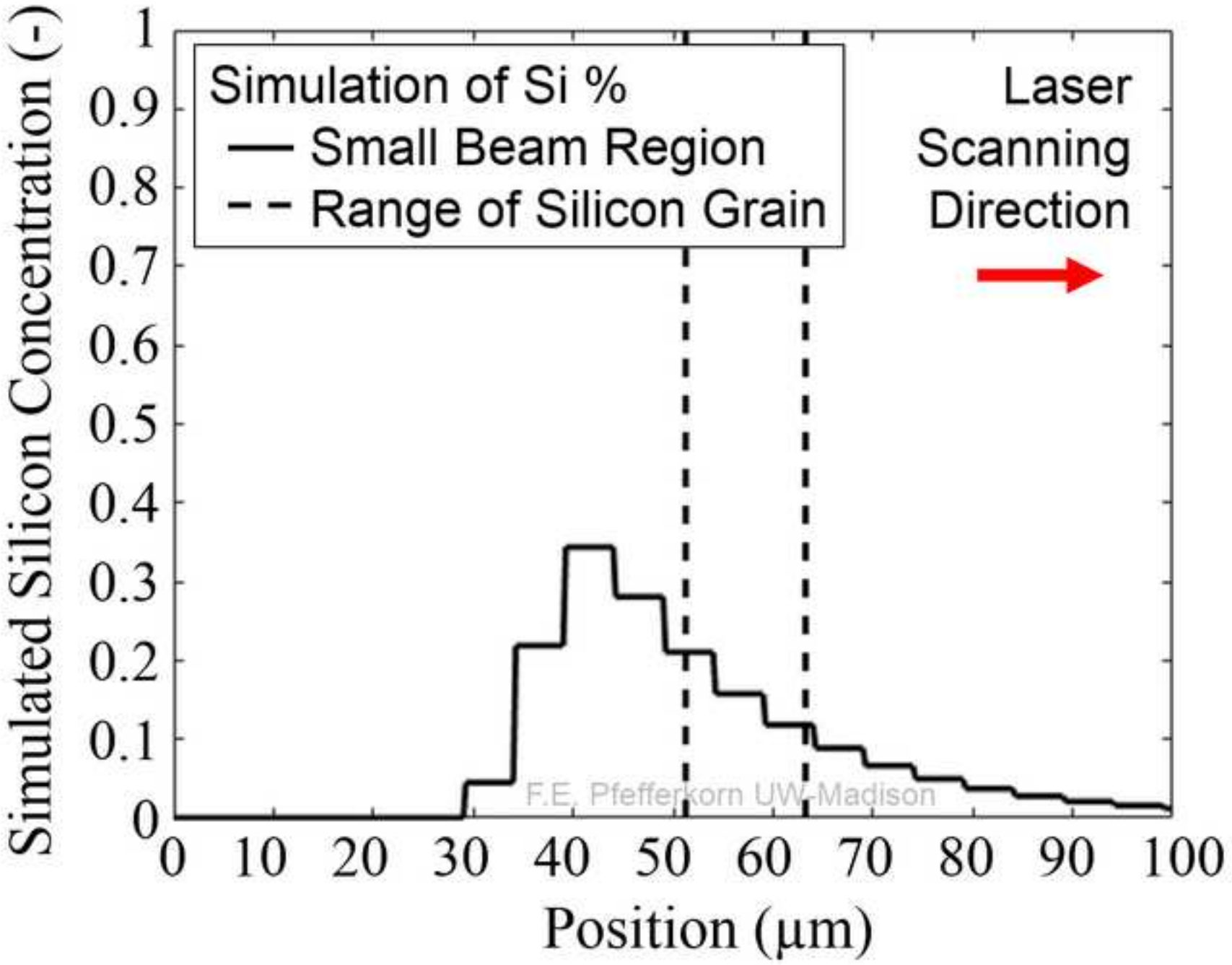

Figure 6c - color

Click here to download high resolution image

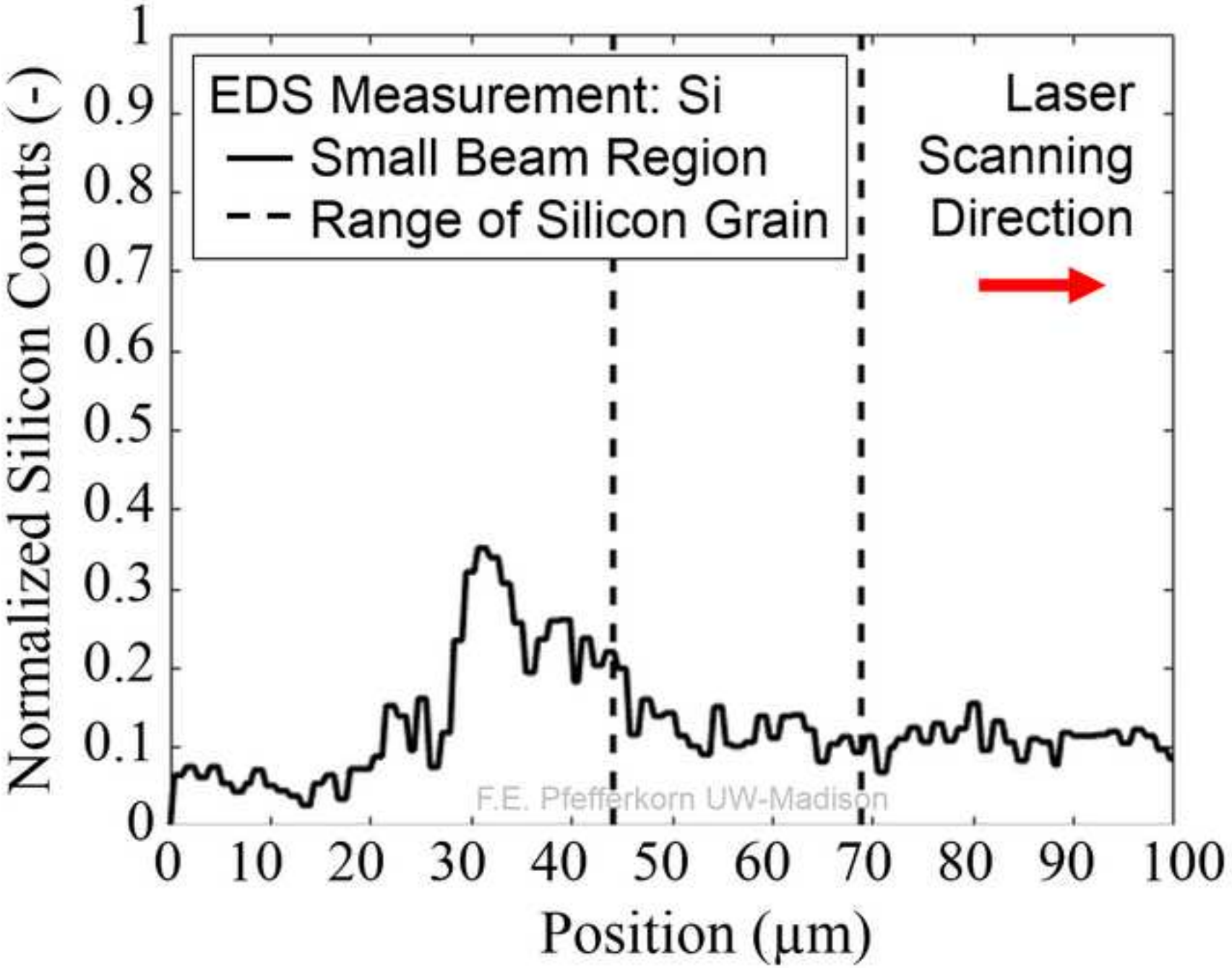

Figure 6d - color

Click here to download high resolution image

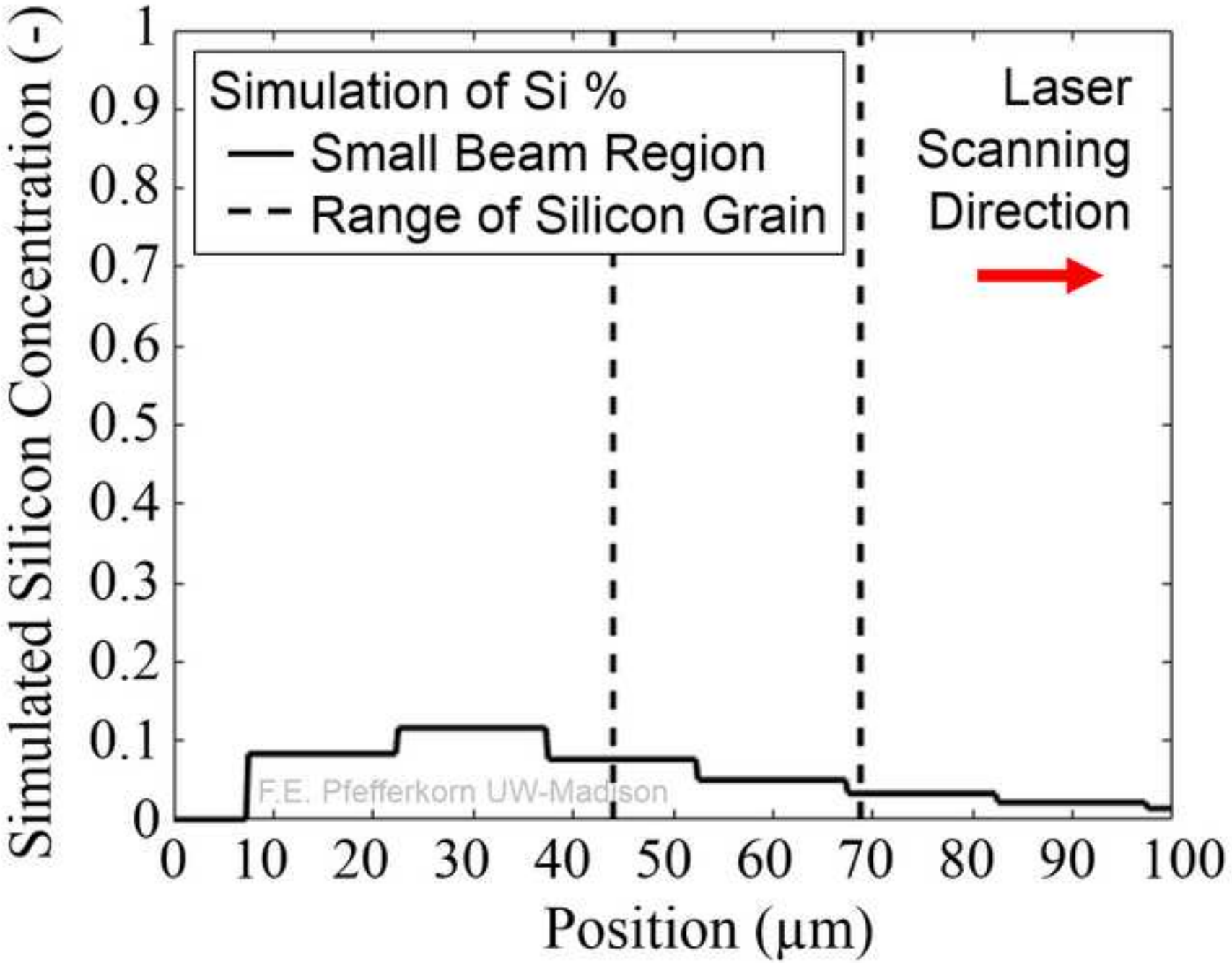

Figure 7a - color

Click here to download high resolution image

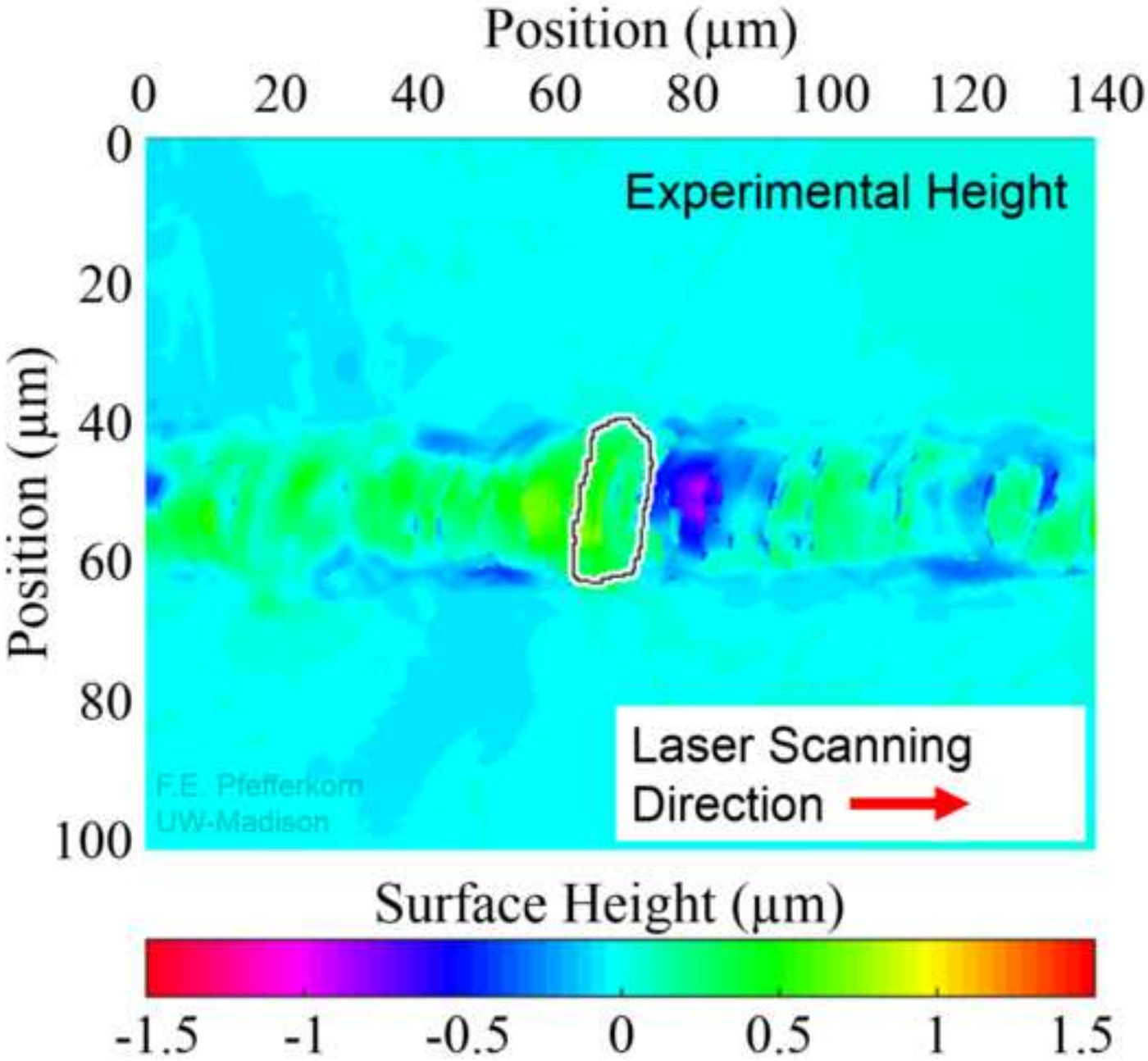

Figure 7b - color

Click here to download high resolution image

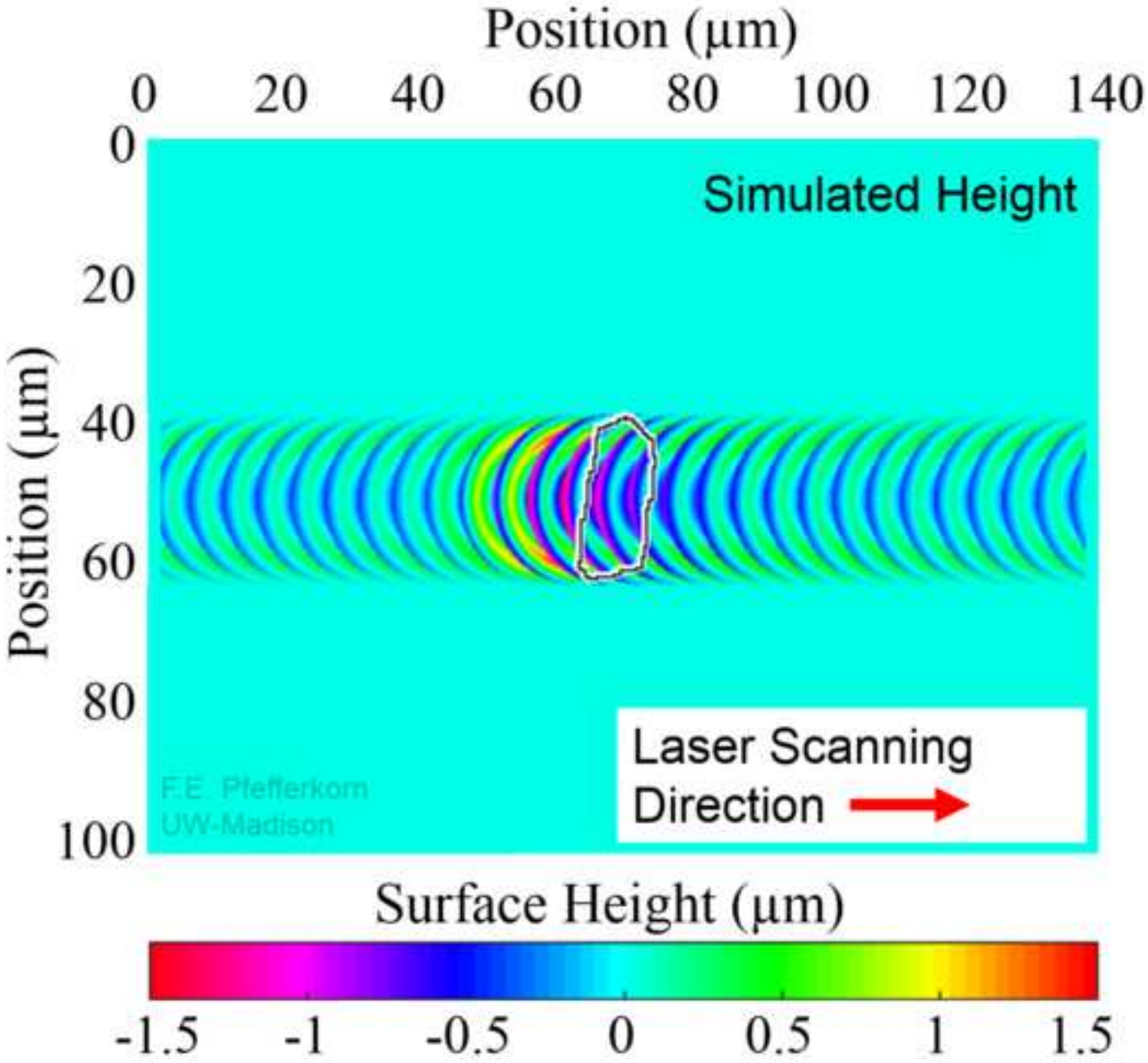

Figure 7c - color

Click here to download high resolution image

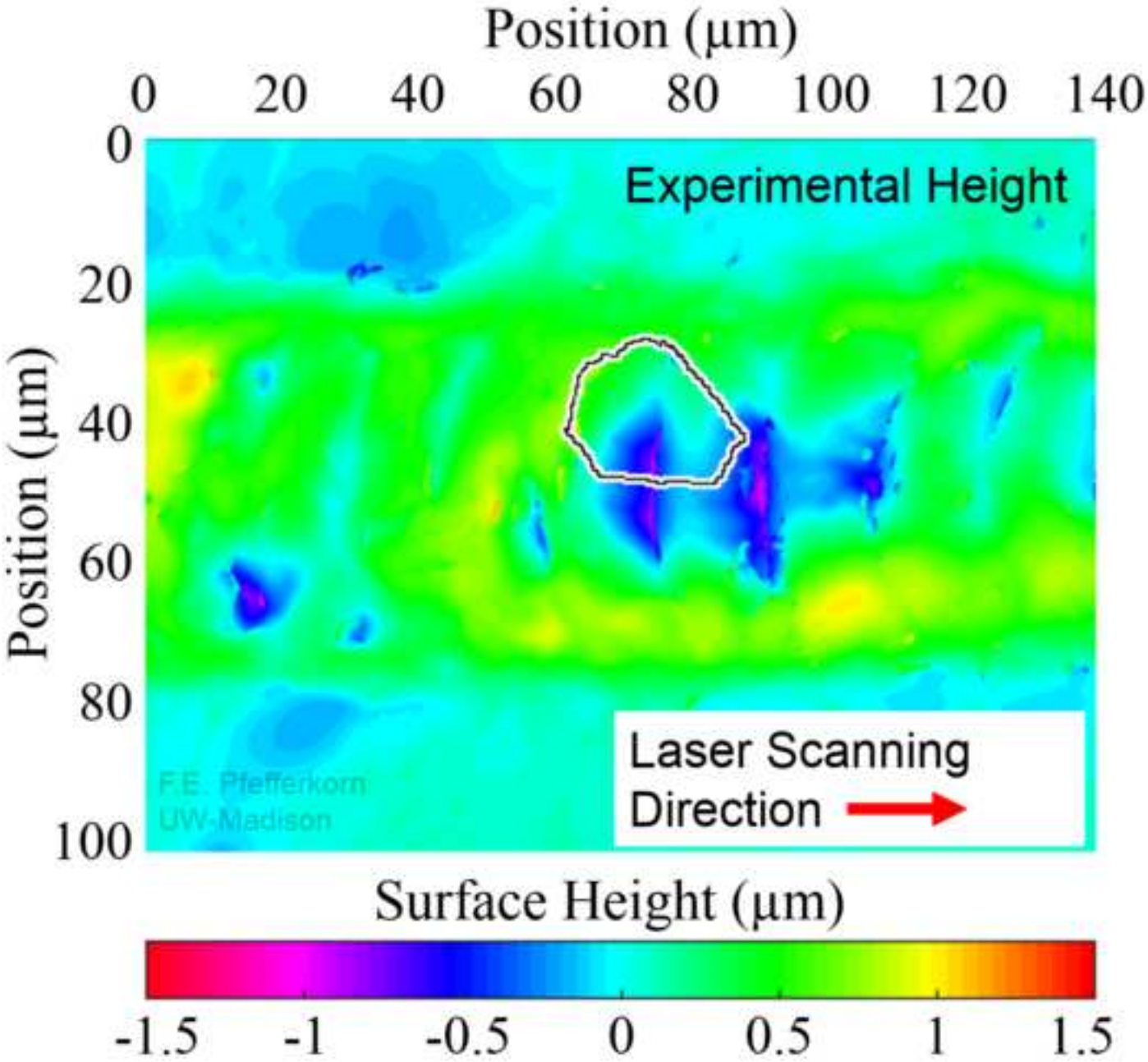

Figure 7d - color

Click here to download high resolution image

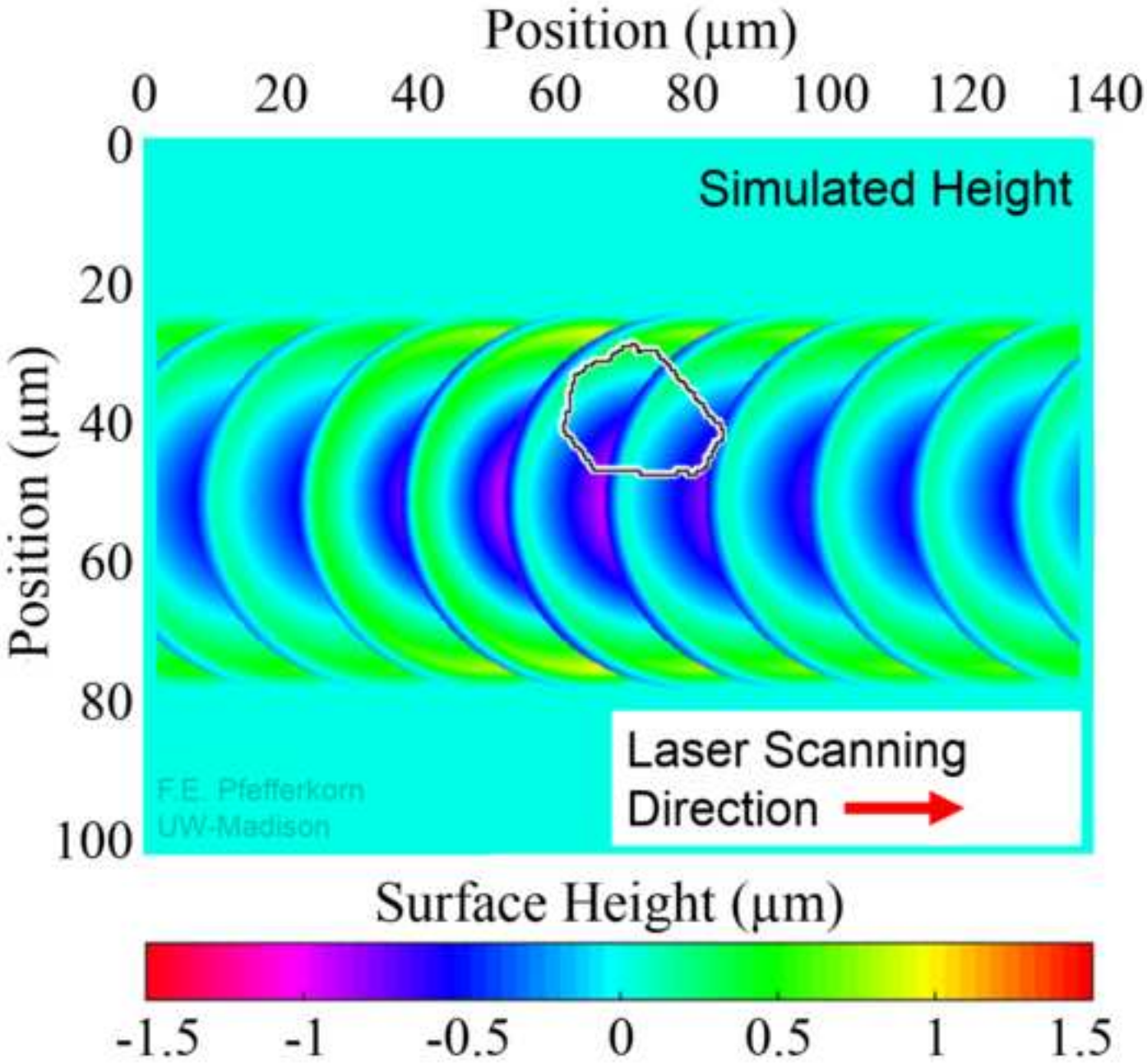

Figure 8a - color
Click here to download high resolution image

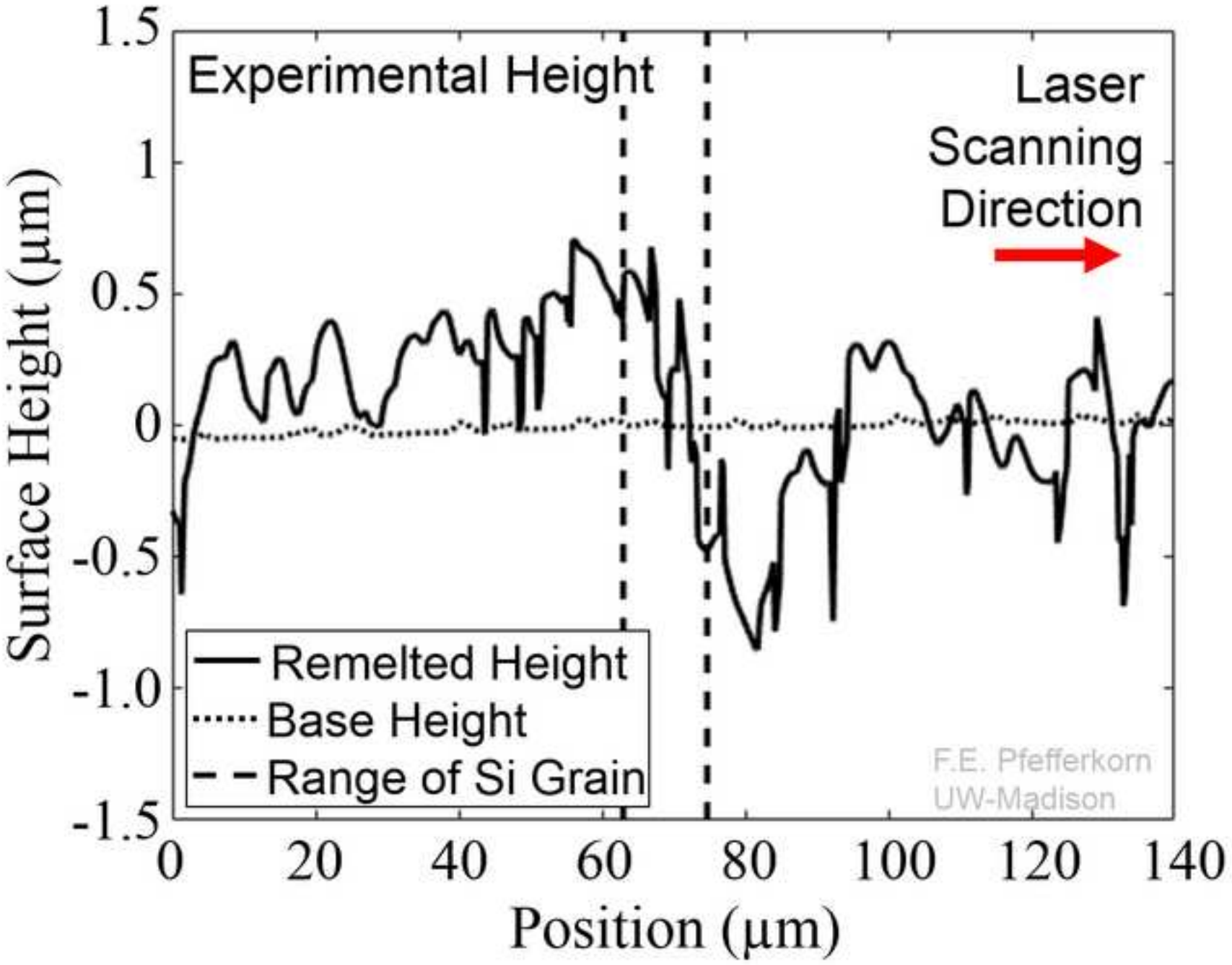

Figure 8b - color

Click here to download high resolution image

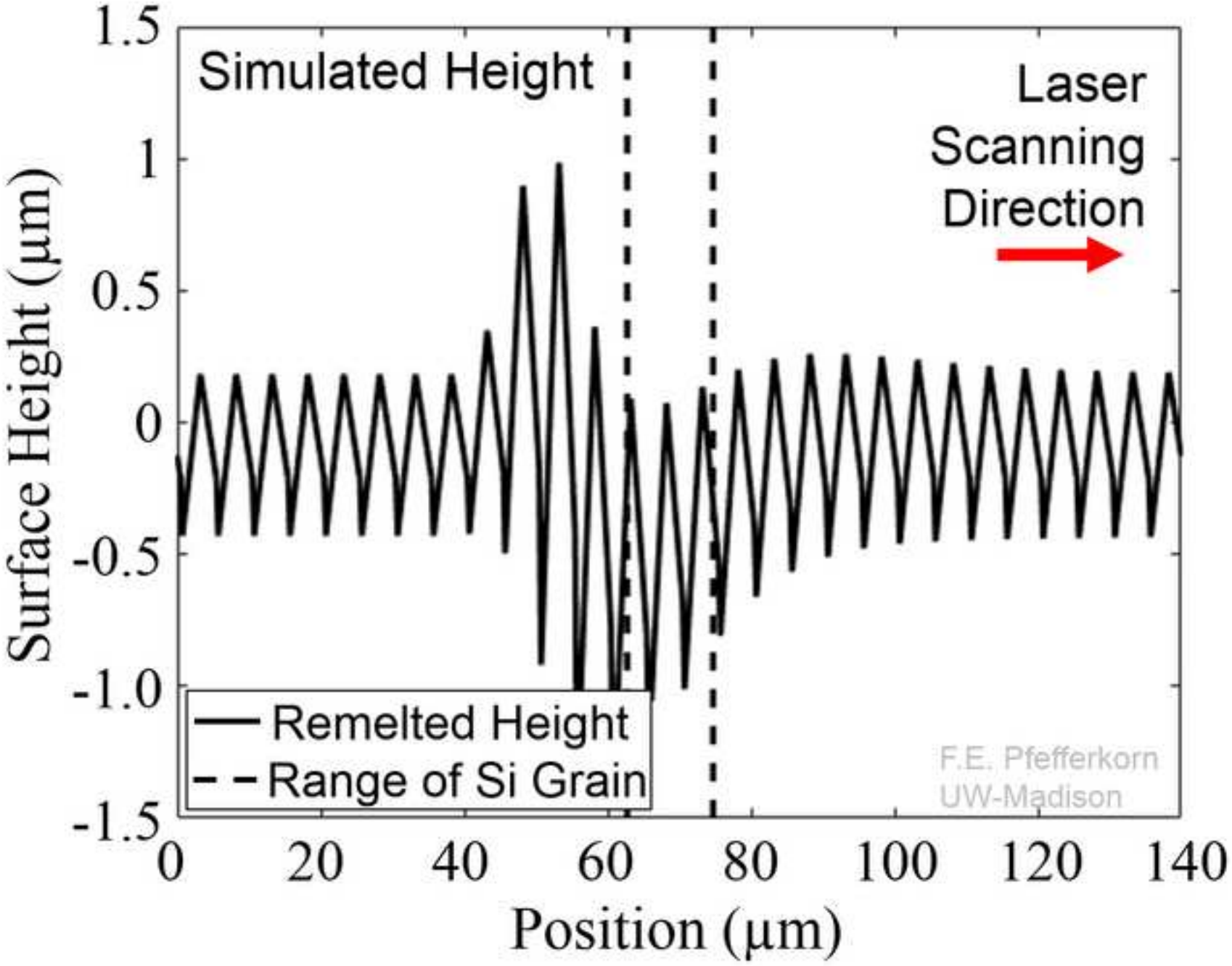

Figure 8c - color

Click here to download high resolution image

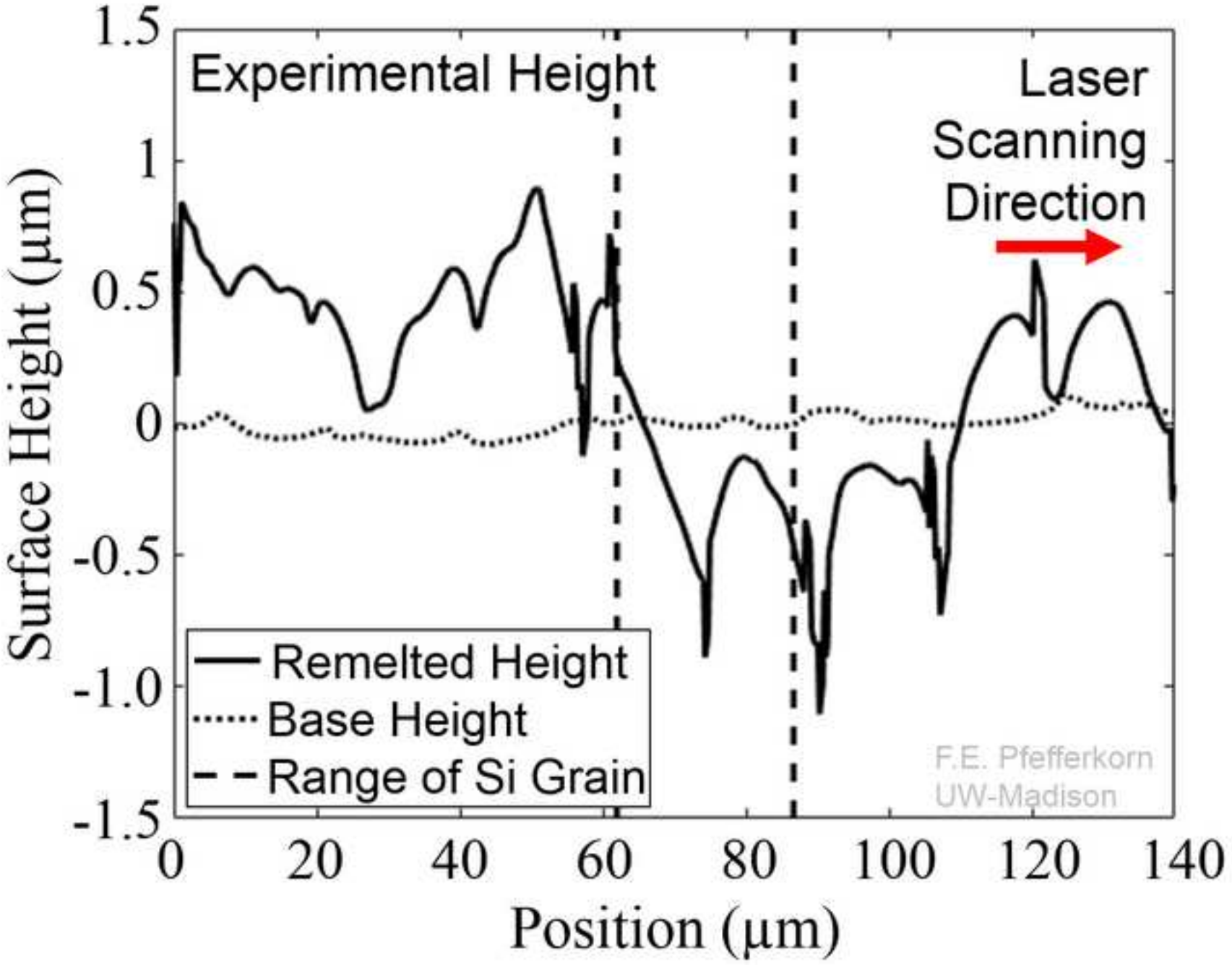

Figure 8d - color

Click here to download high resolution image

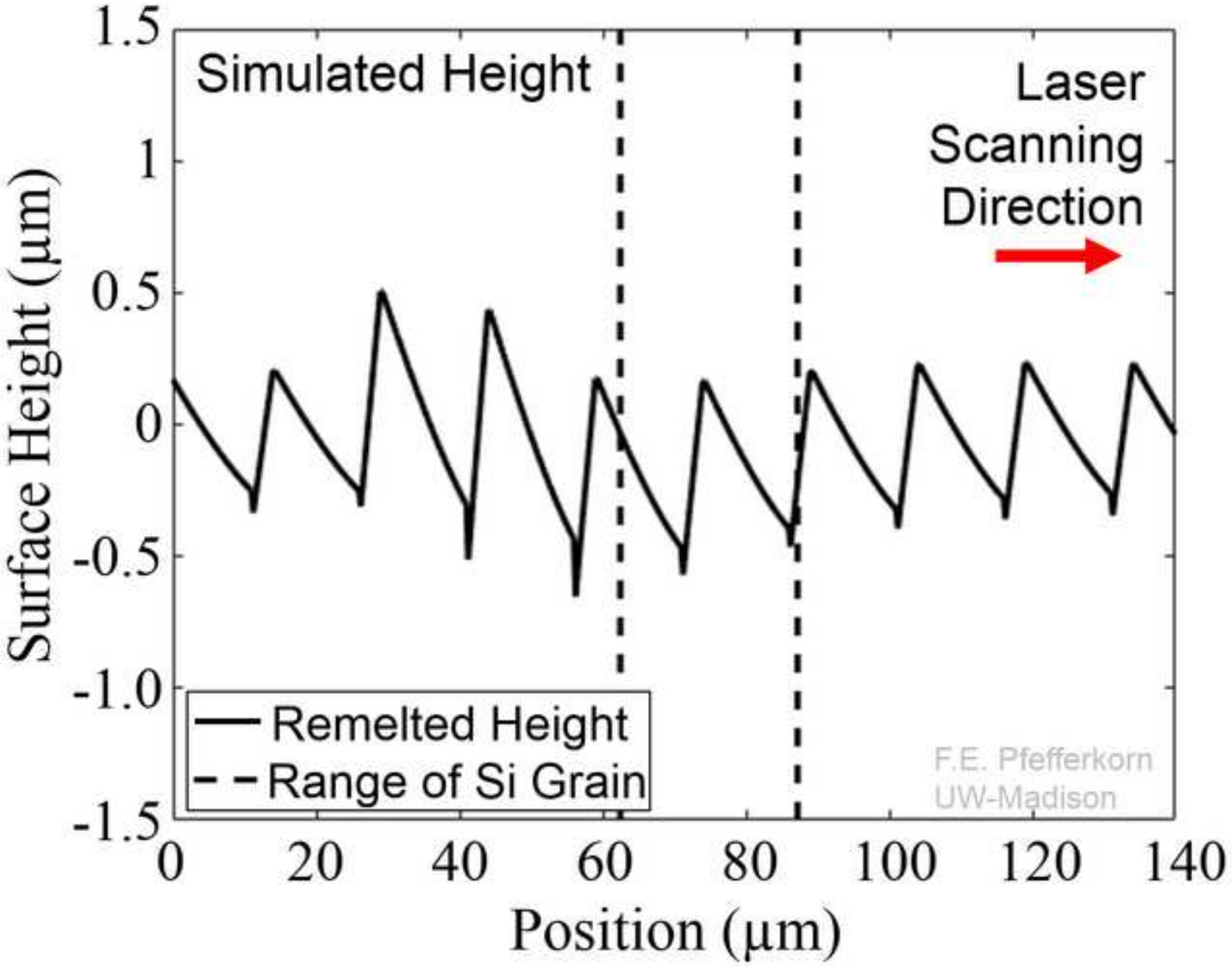

Figure 9a - color

Click here to download high resolution image

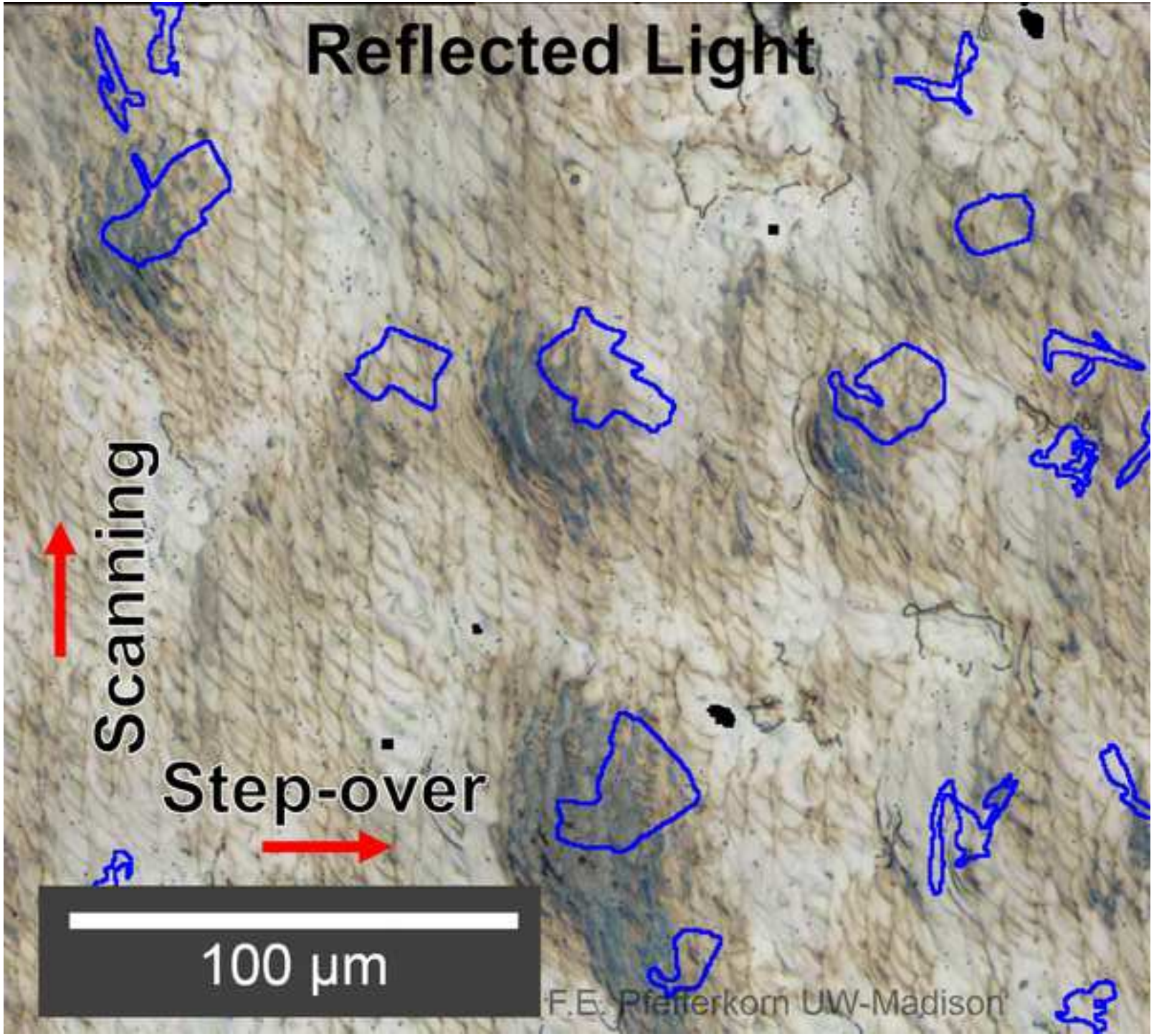

Figure 9b - color

Click here to download high resolution image

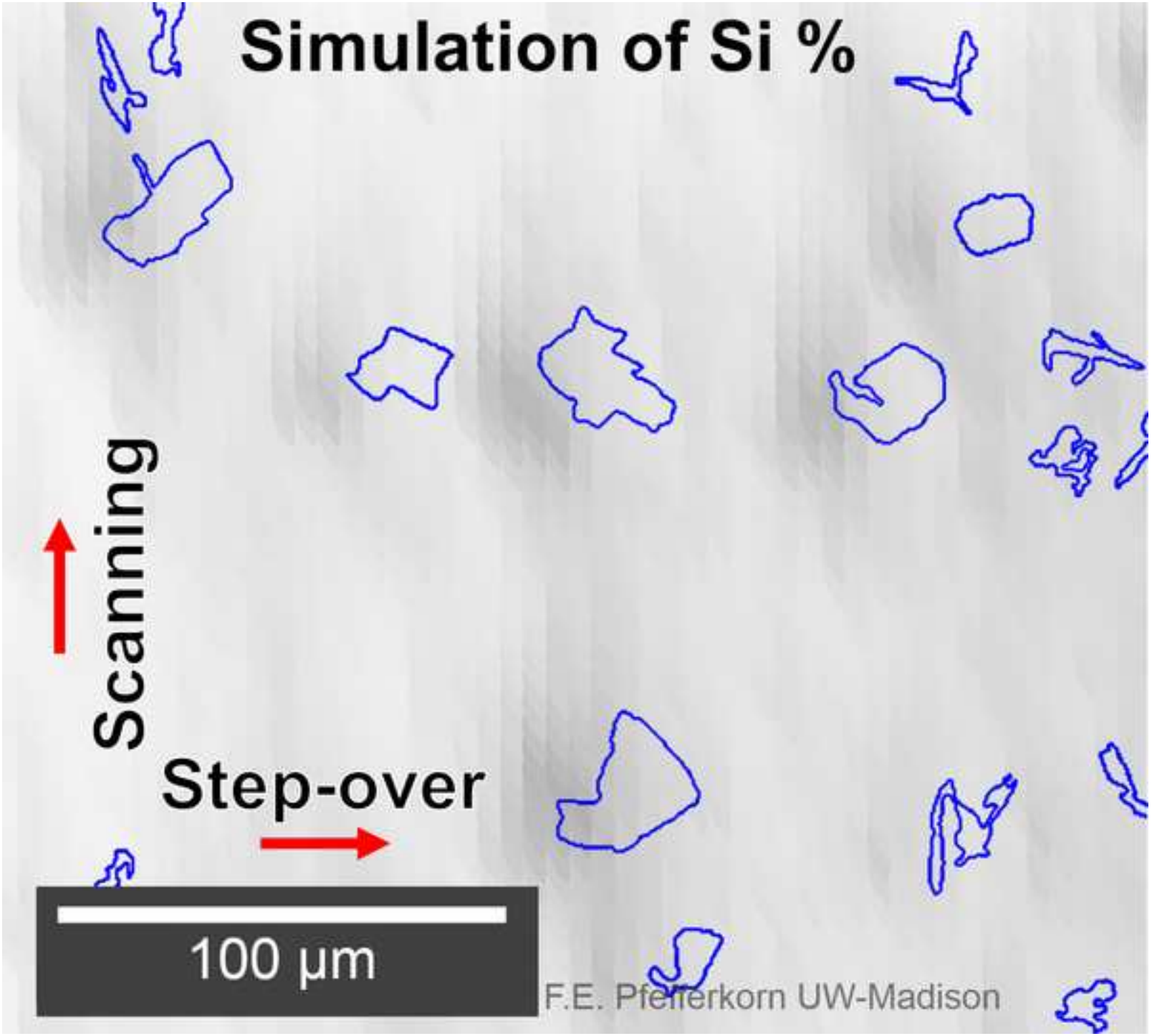

Figure 10a - color

Click here to download high resolution image

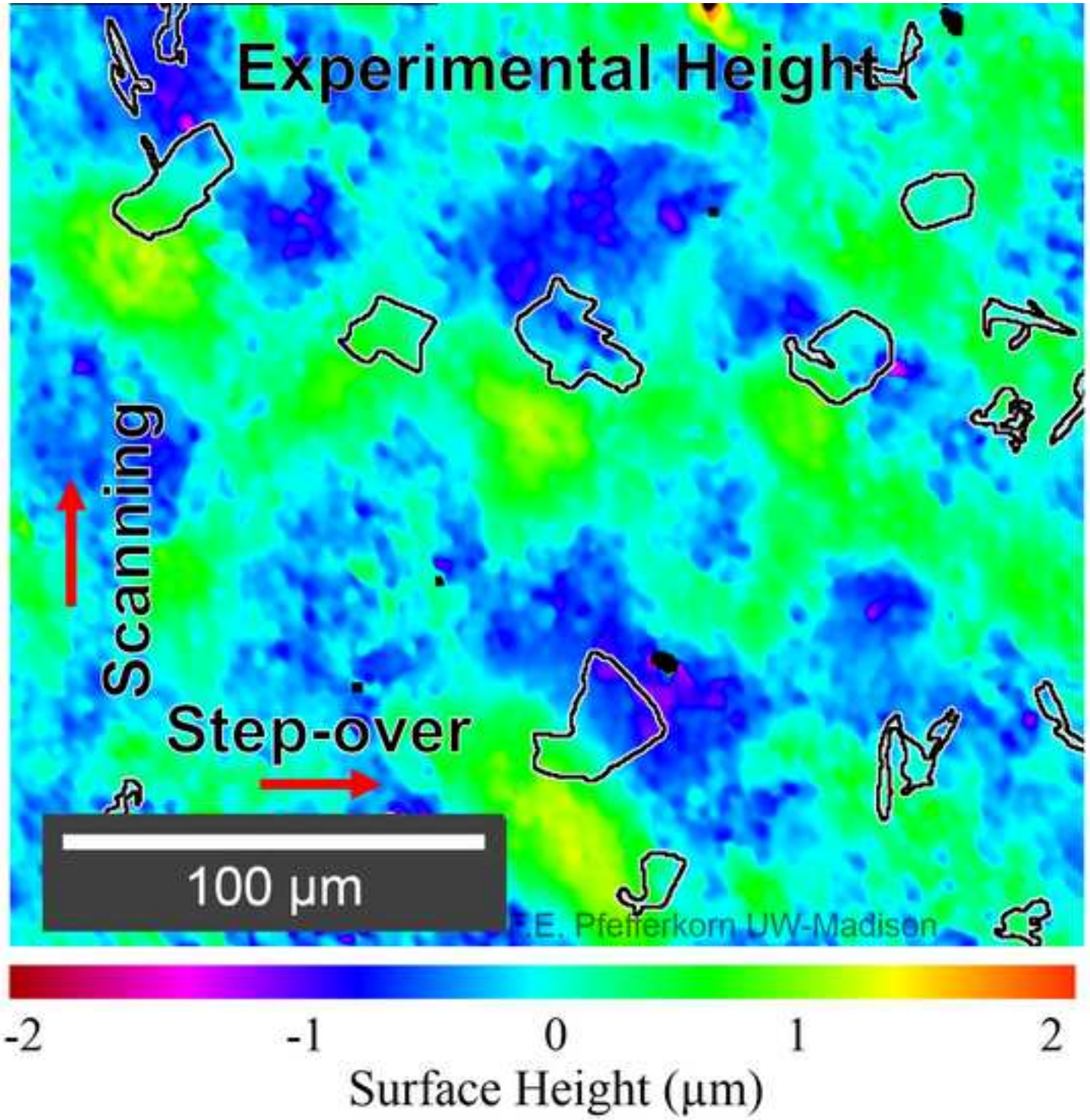

Figure 10b - color

Click here to download high resolution image

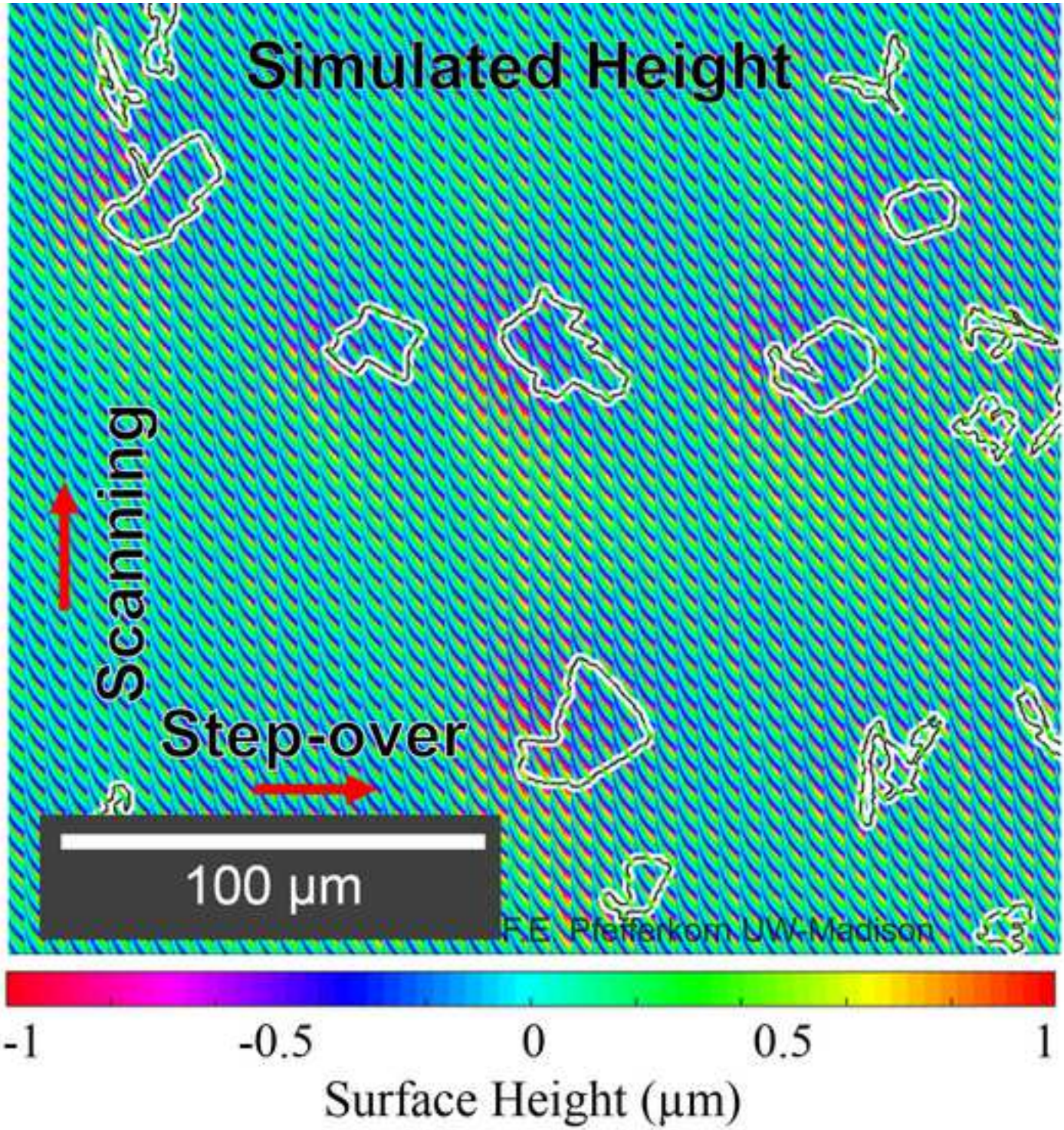

Figure 11a - color

Click here to download high resolution image

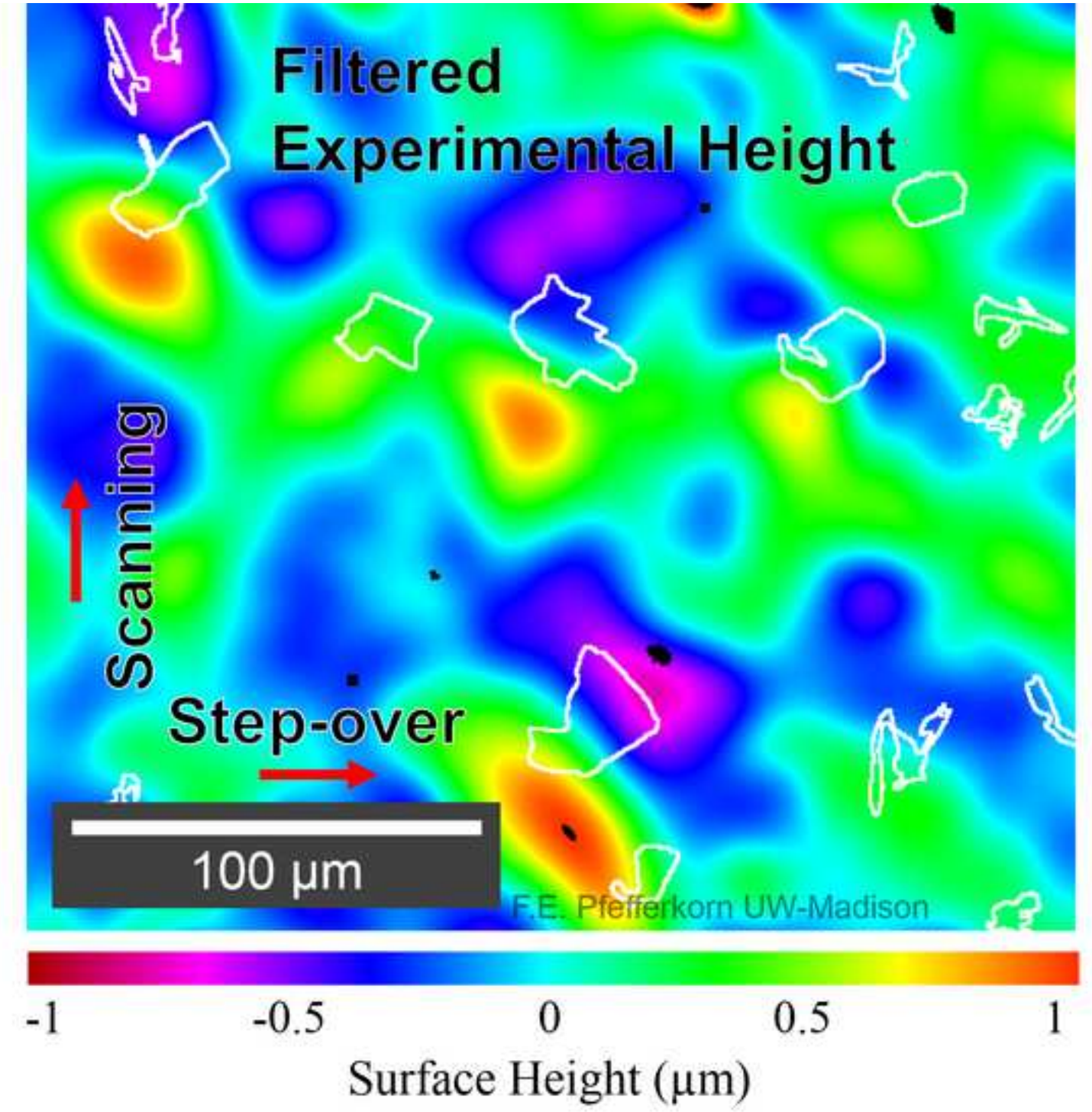

Figure 11b - color

Click here to download high resolution image

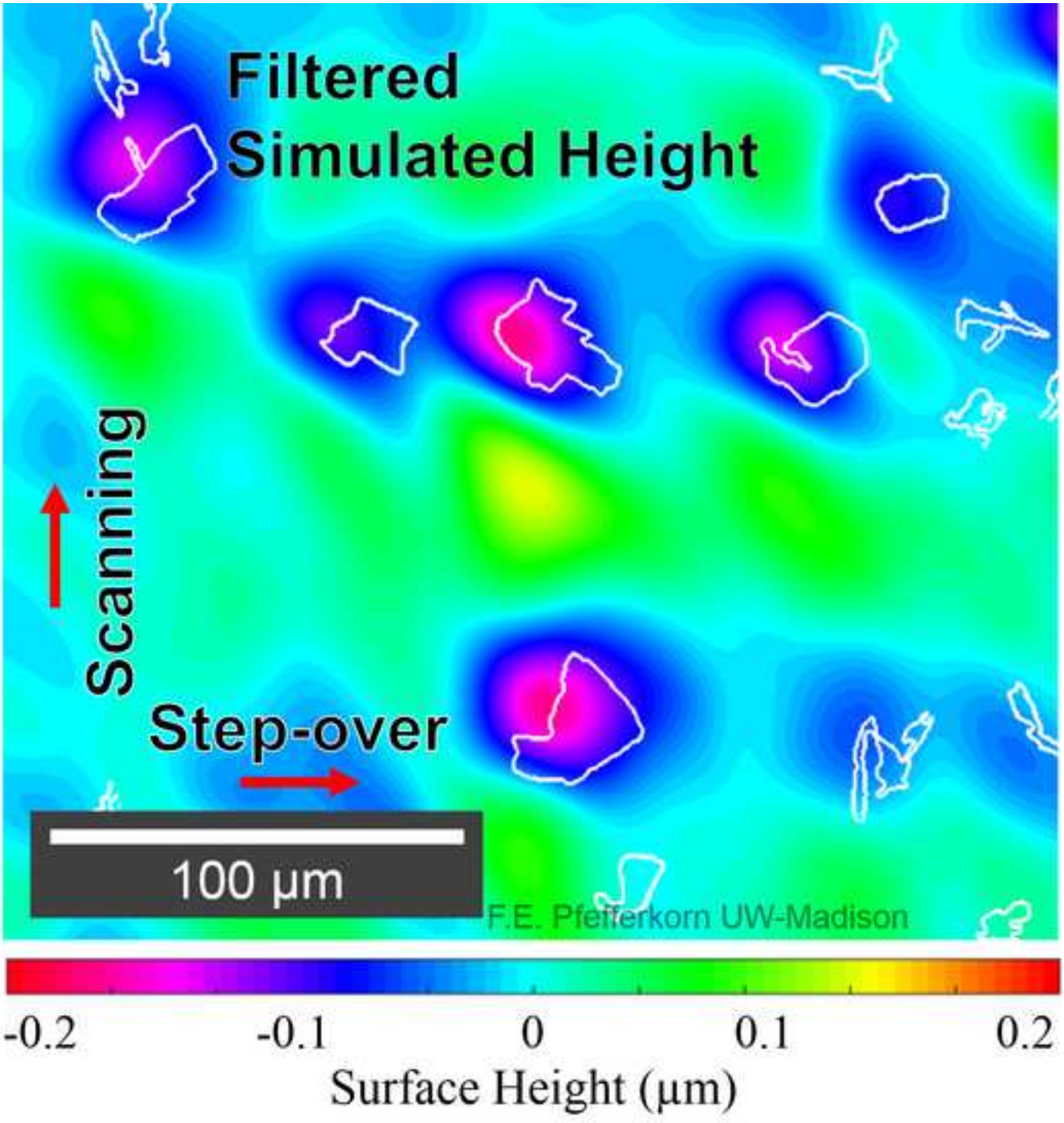

Figure 1 - grayscale

Click here to download high resolution image

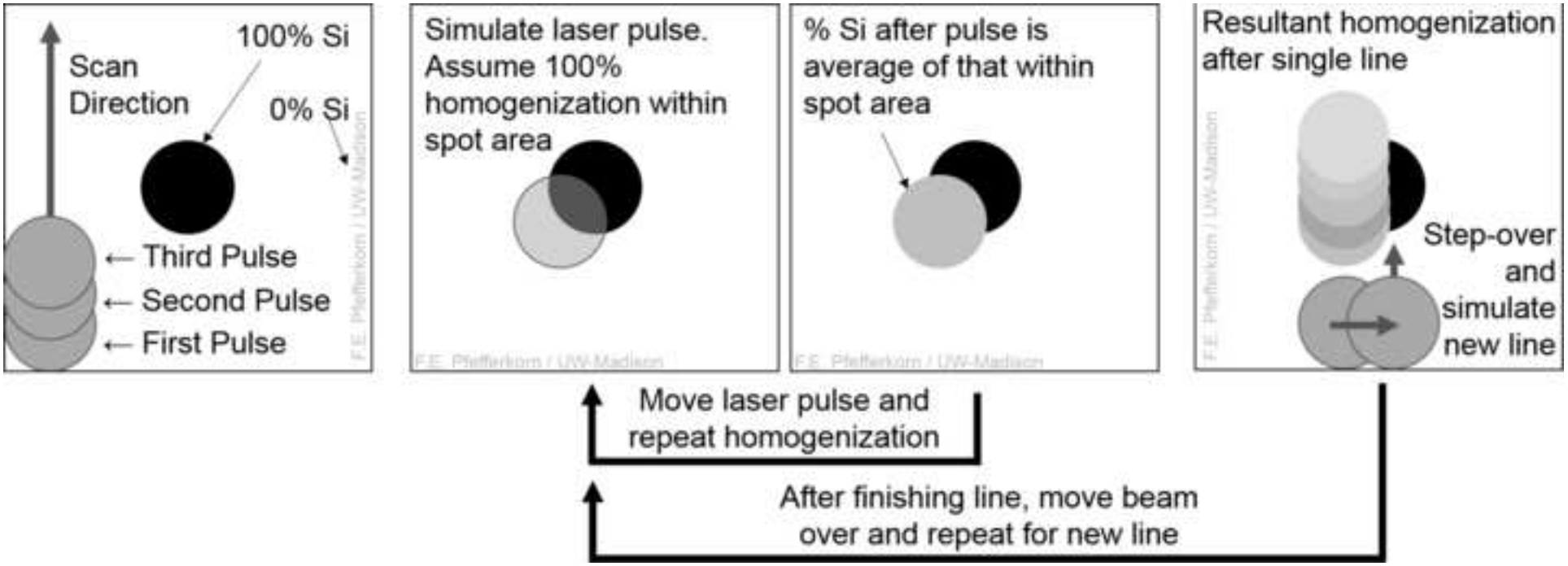

Figure 2a - grayscale
Click here to download high resolution image

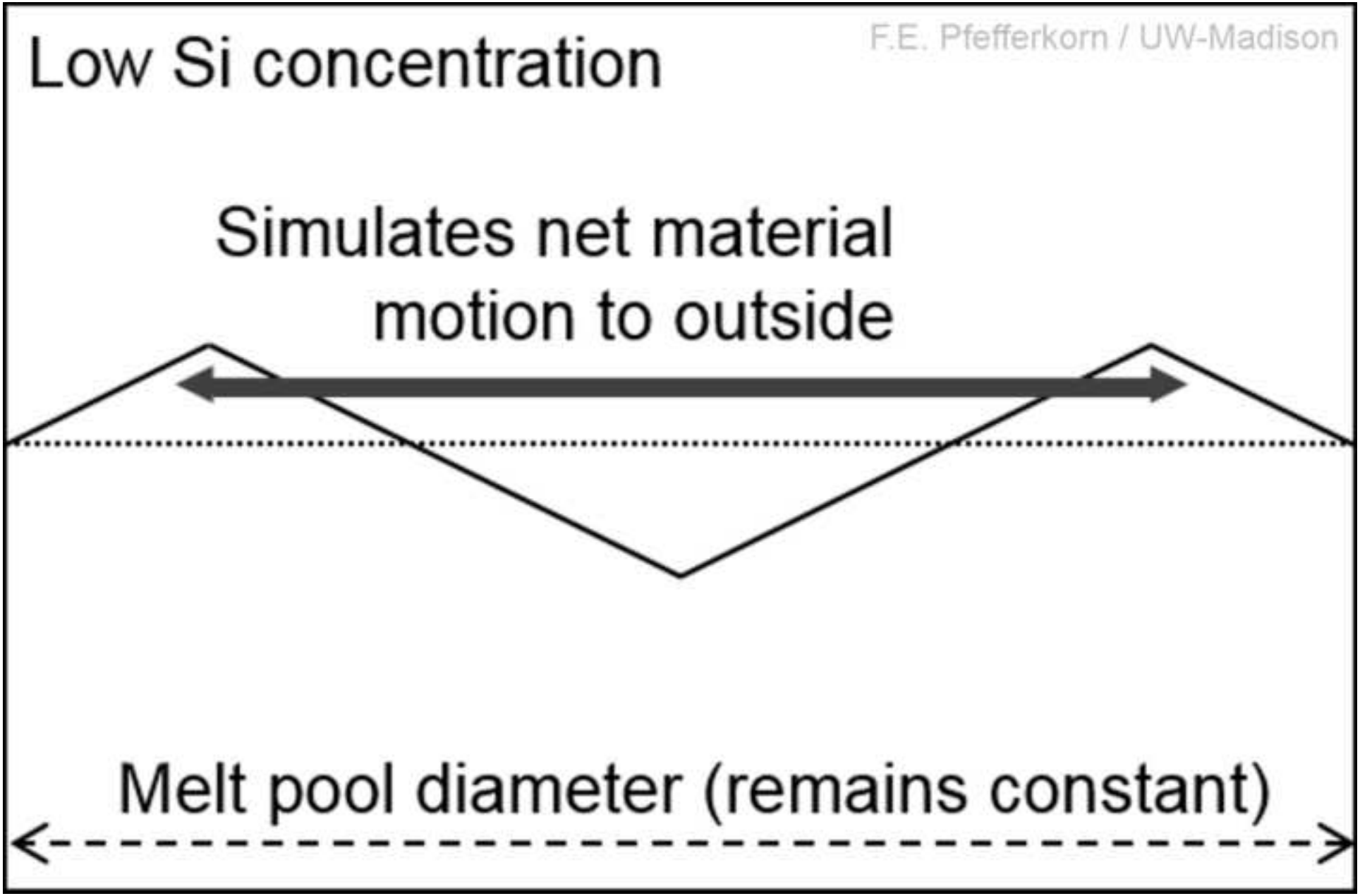

Figure 2c - grayscale

Click here to download high resolution image

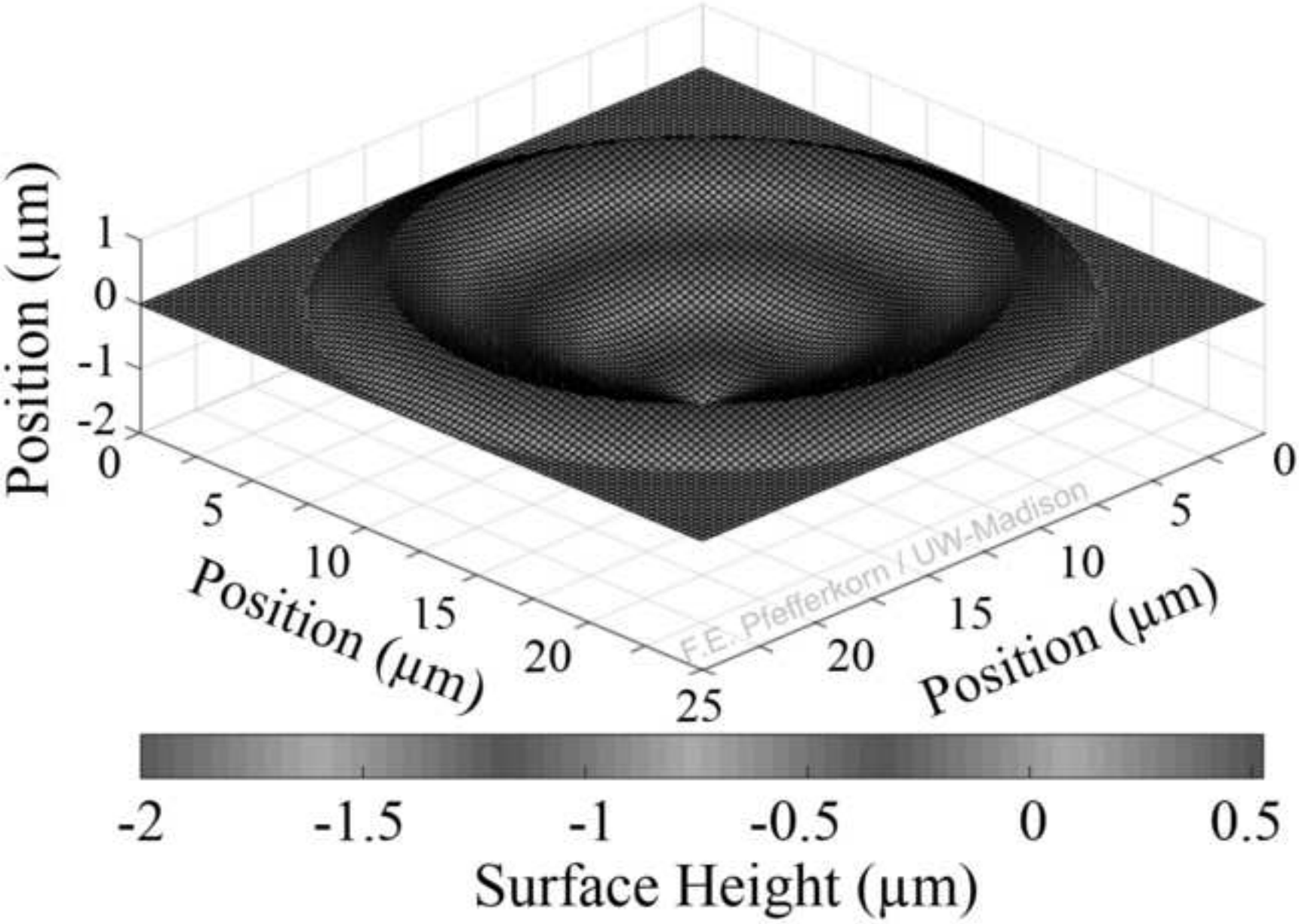

Figure 3ab - grayscale

Click here to download high resolution image

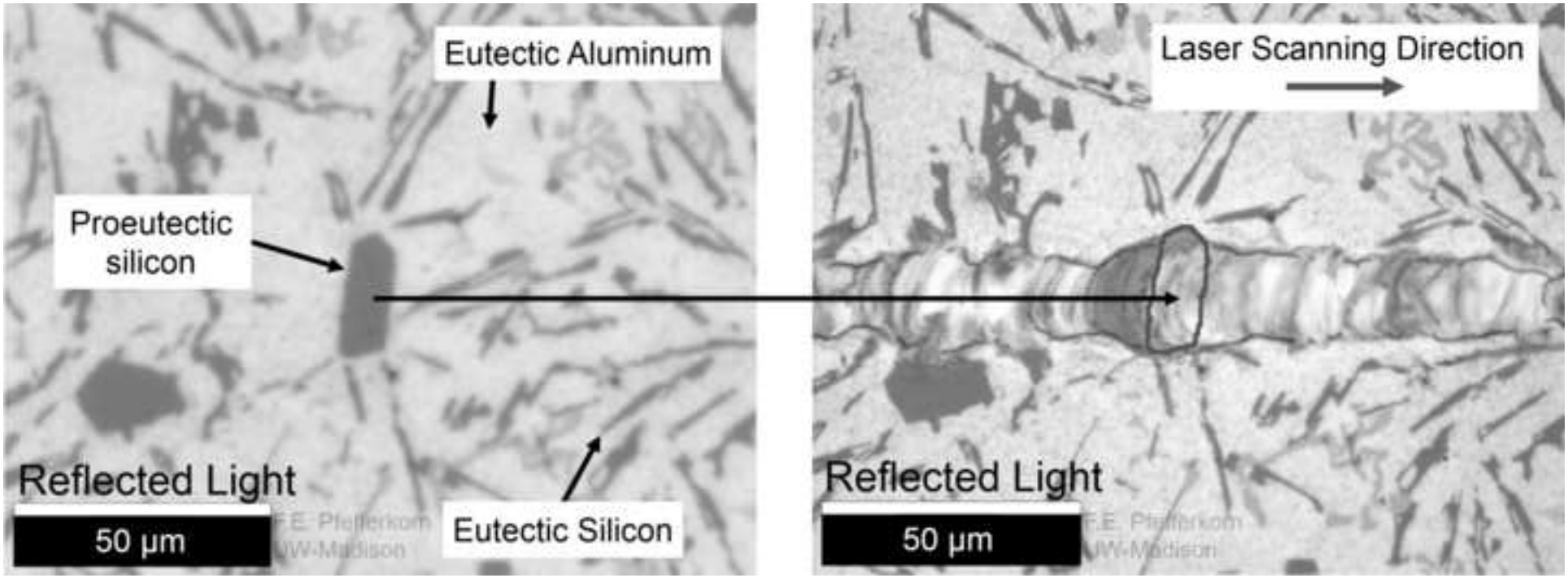

Figure 3cd - grayscale
Click here to download high resolution image

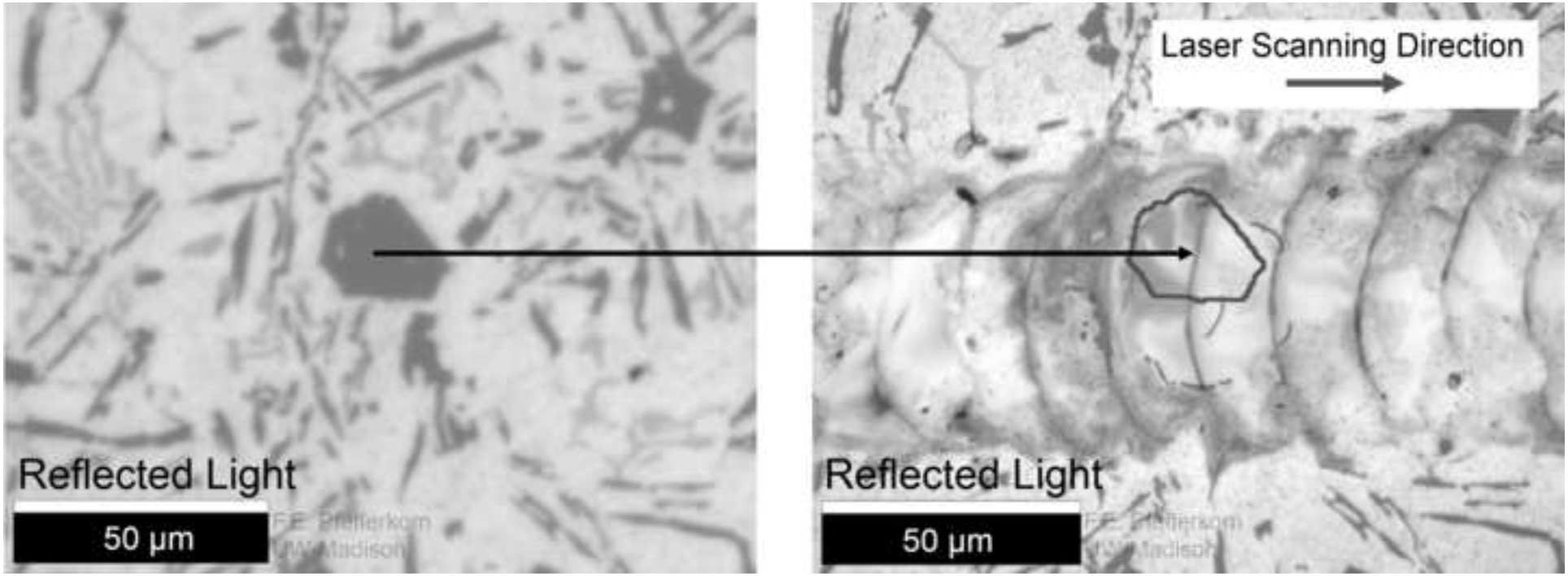

Figure 4a - grayscale

Click here to download high resolution image

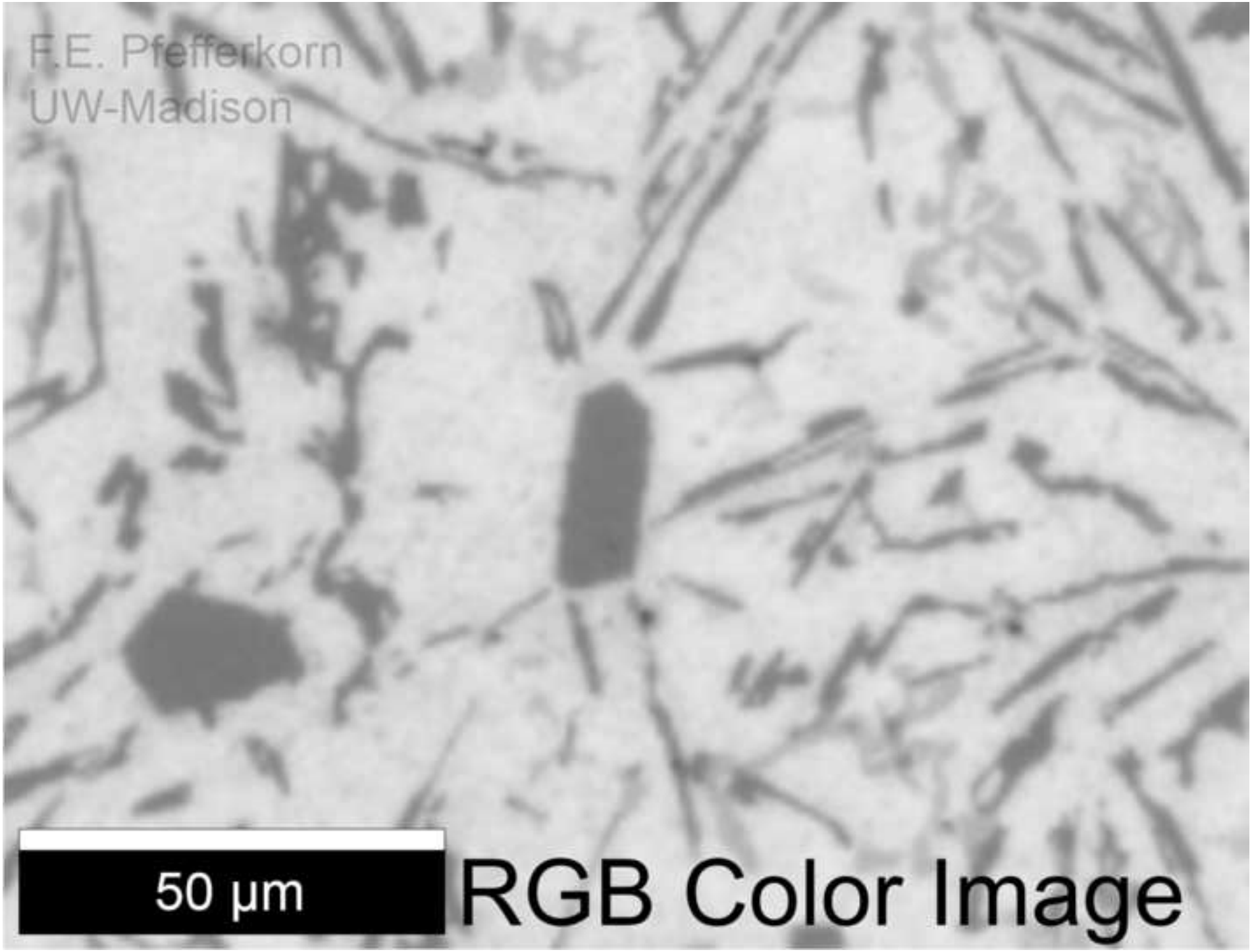

Figure 5a - grayscale
Click here to download high resolution image

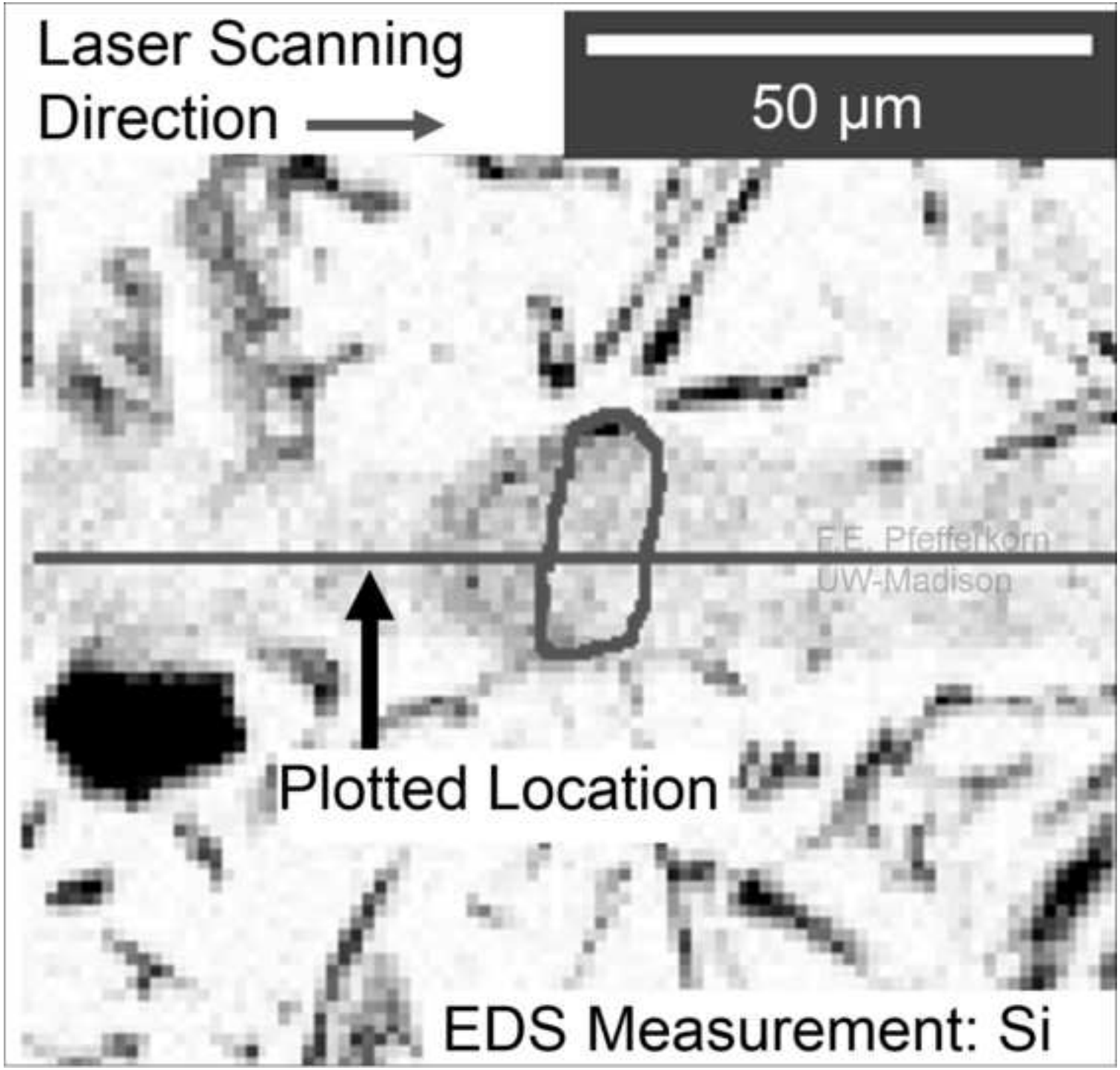

Figure 5b - grayscale
Click here to download high resolution image

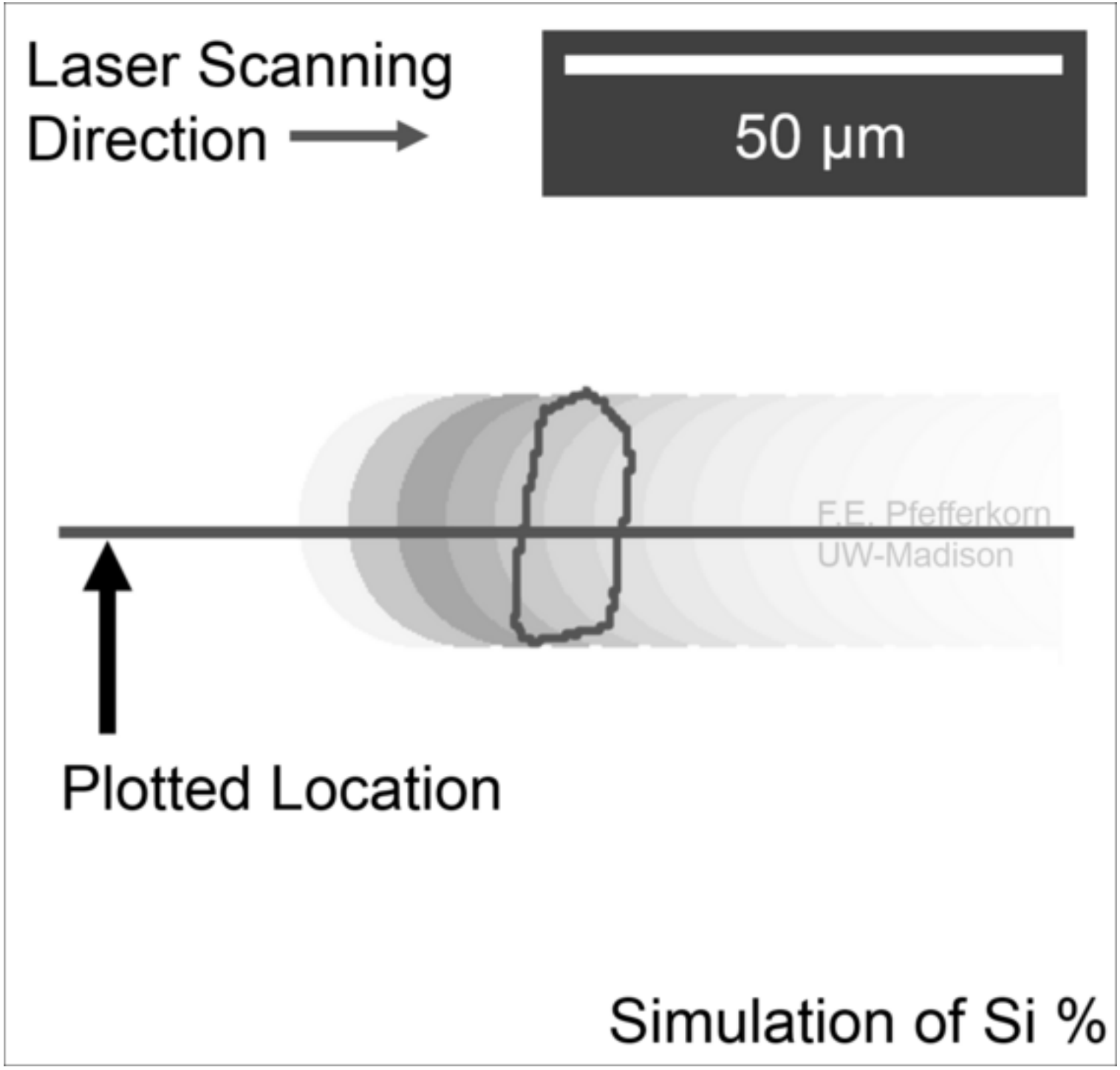

Figure 5c - grayscale
Click here to download high resolution image

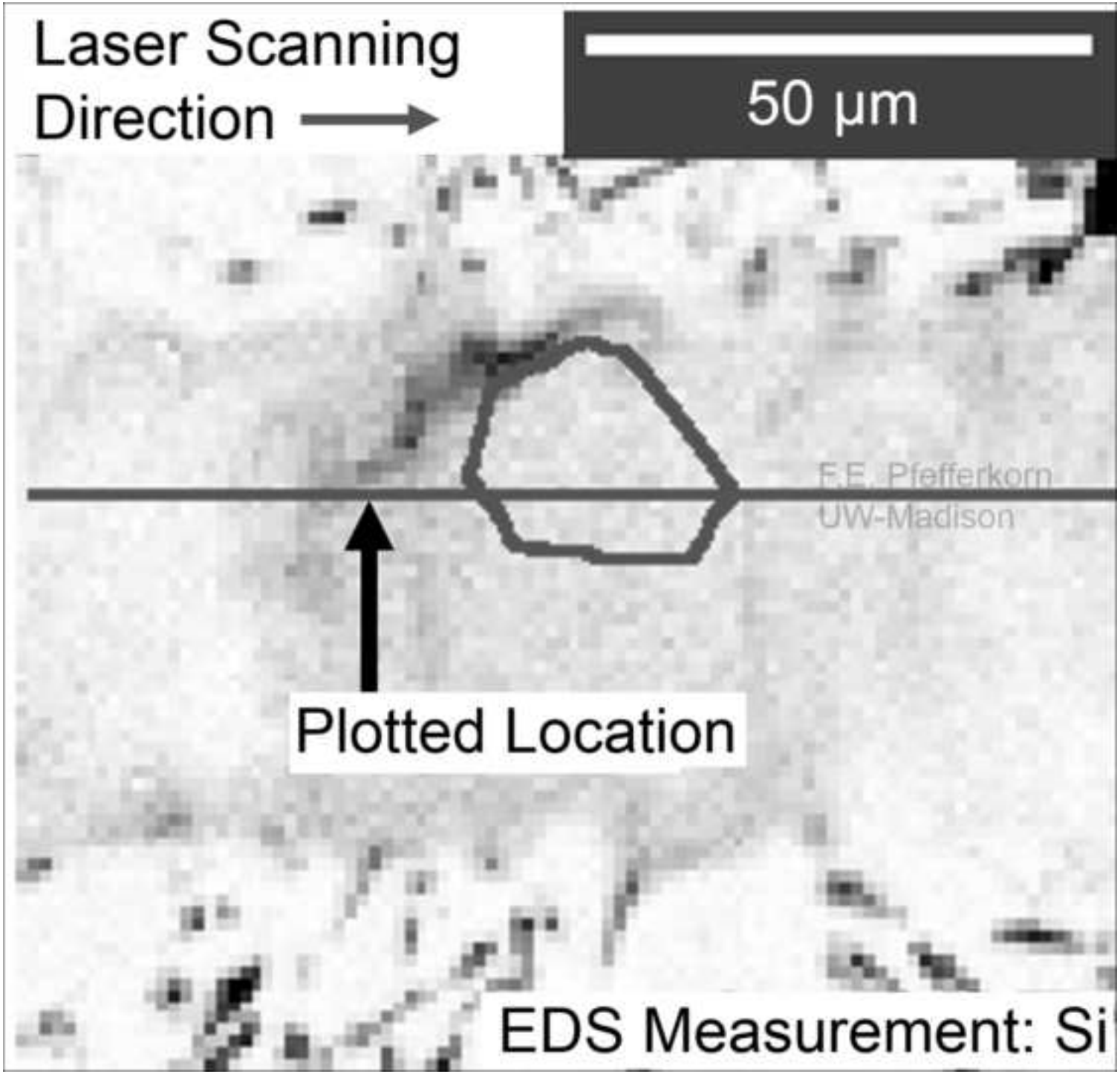

Figure 5d - grayscale
Click here to download high resolution image

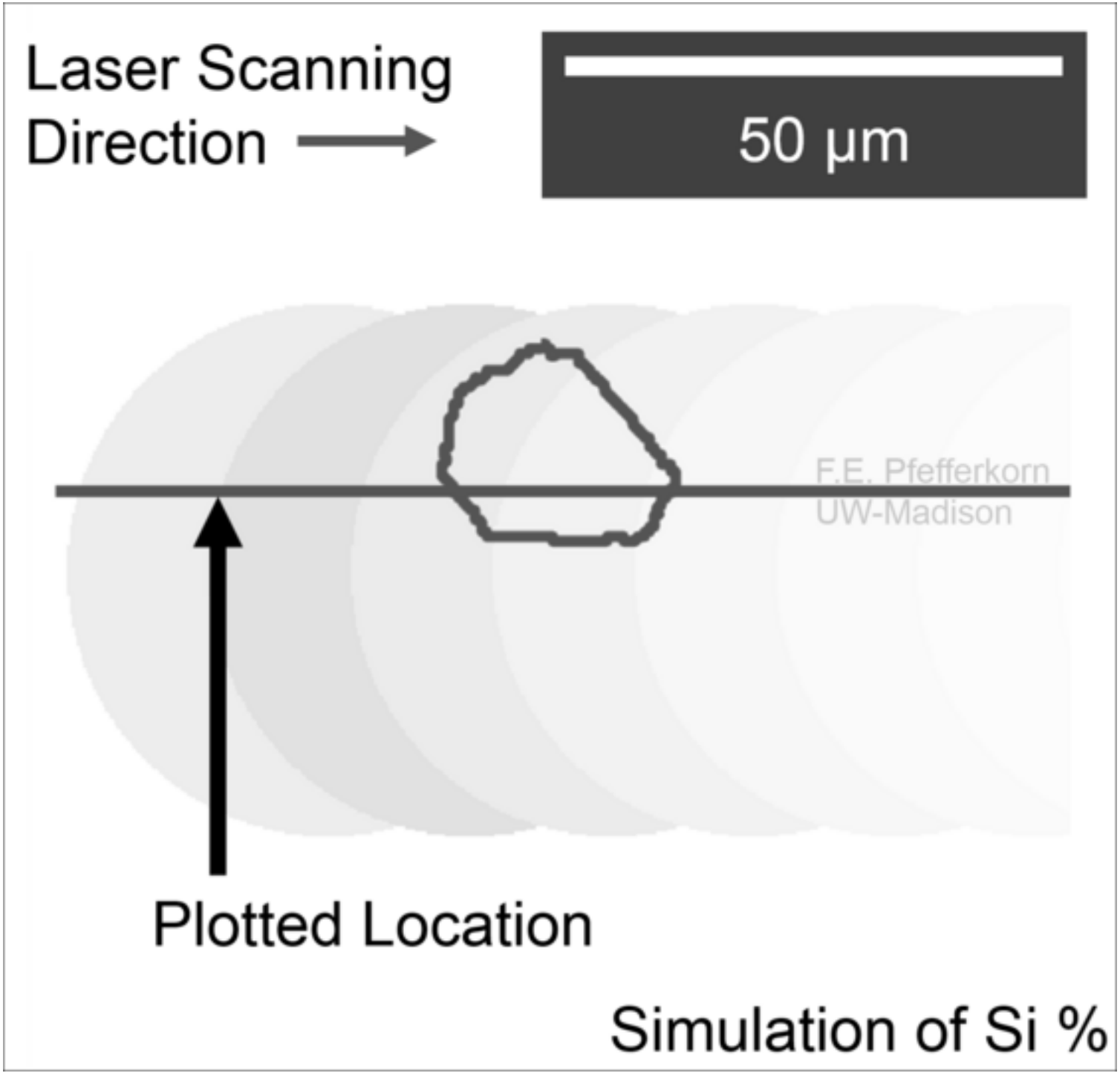

Figure 6a - grayscale
Click here to download high resolution image

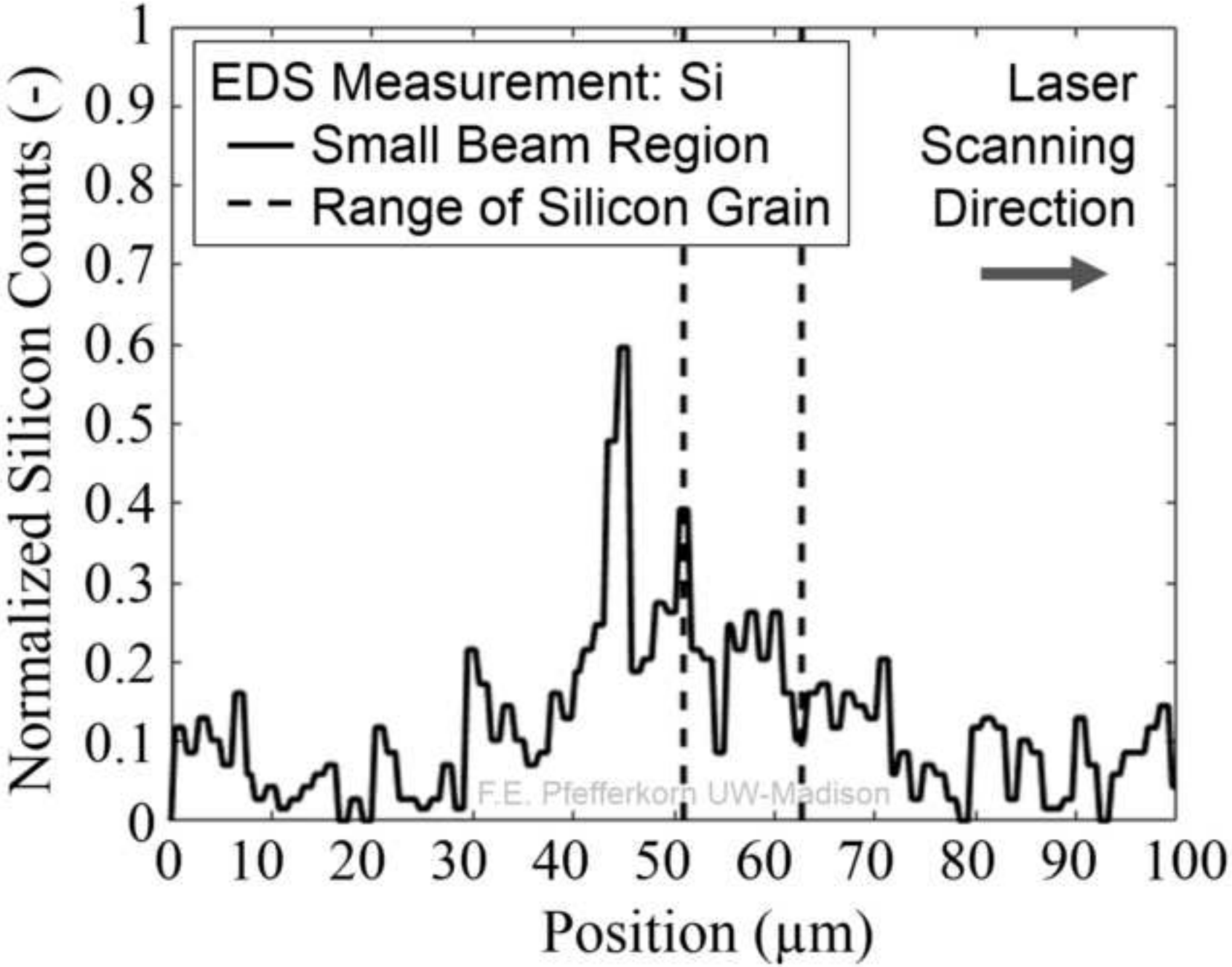

Figure 6b - grayscale
Click here to download high resolution image

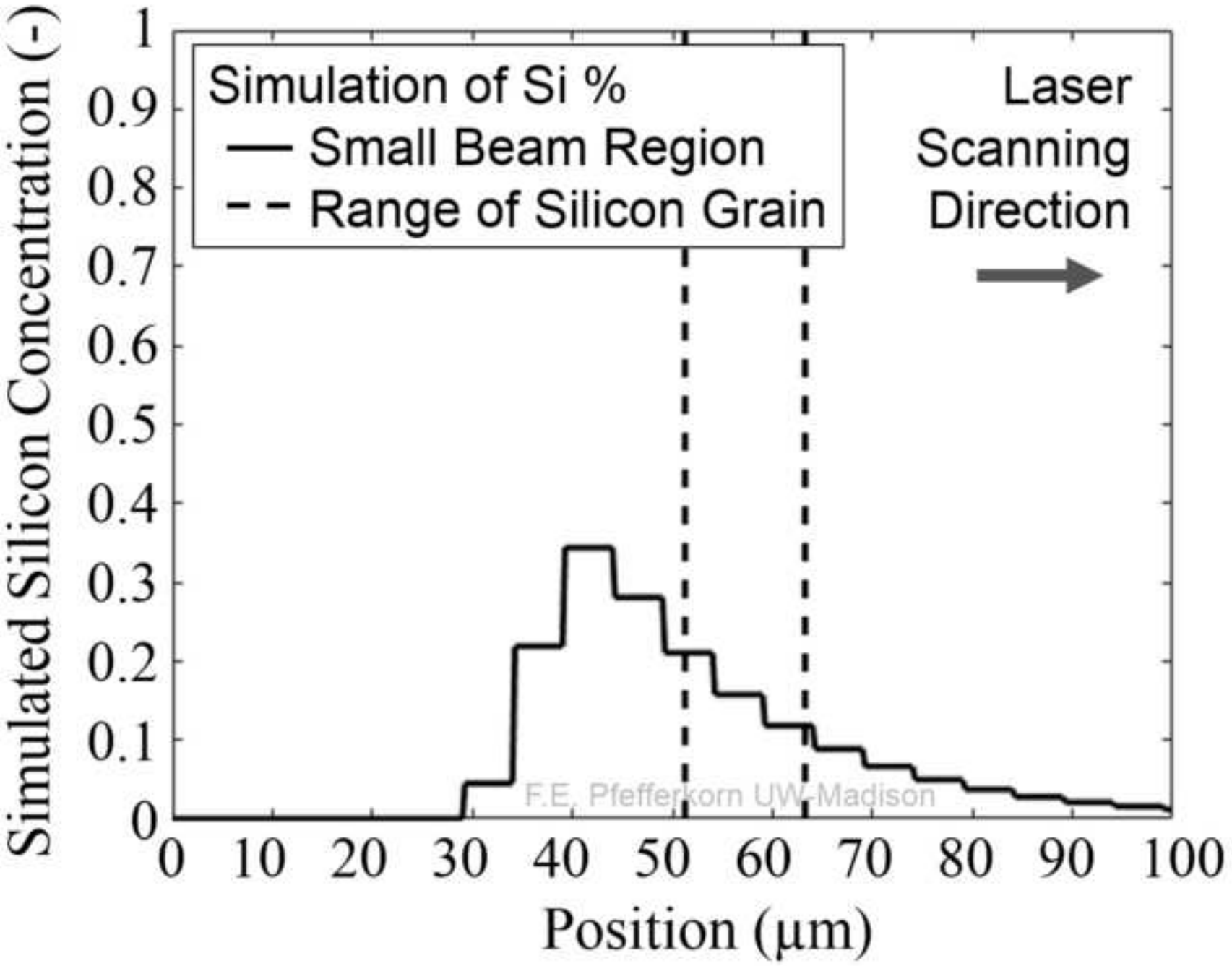

Figure 6c - grayscale
Click here to download high resolution image

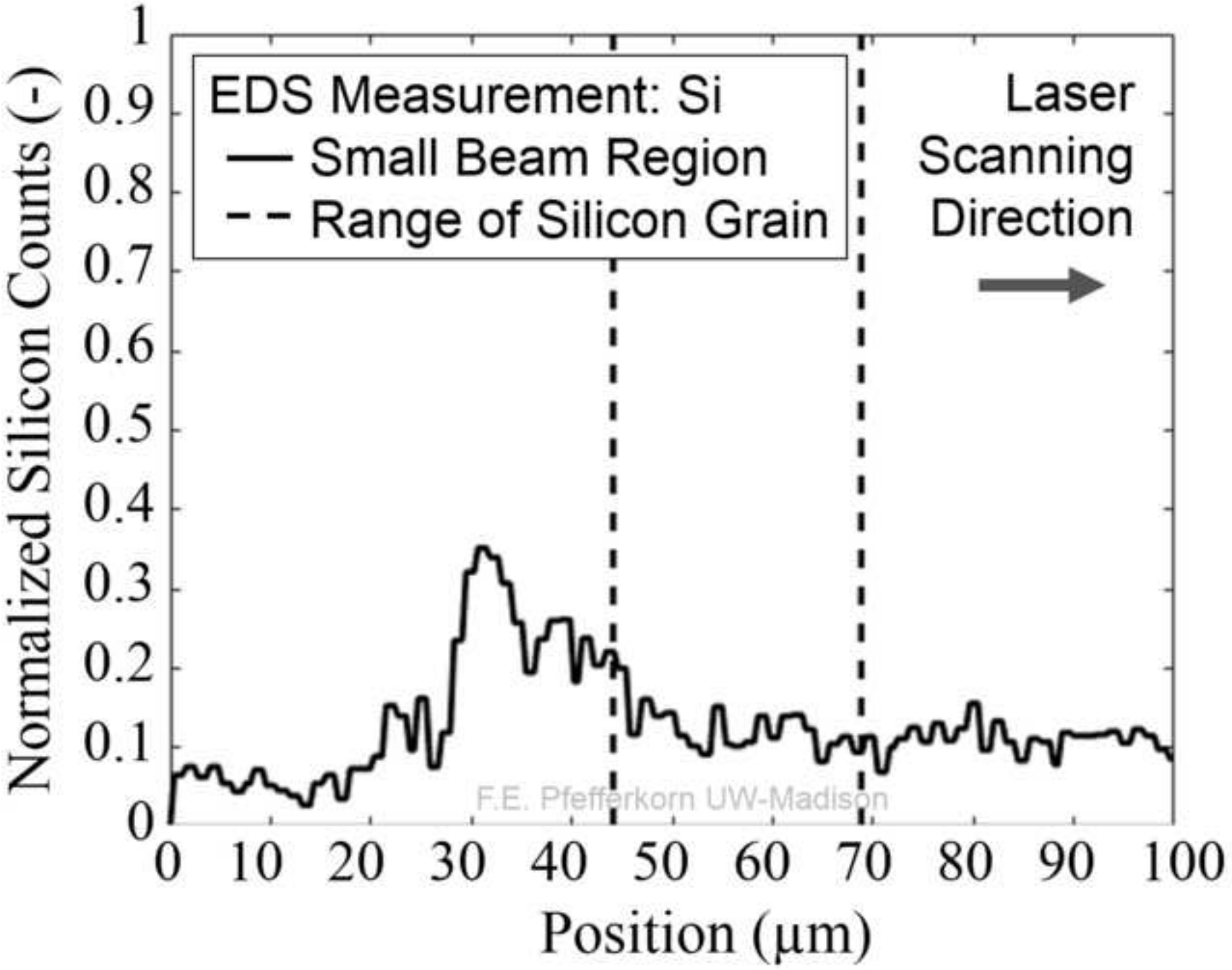

Figure 6d - grayscale
Click here to download high resolution image

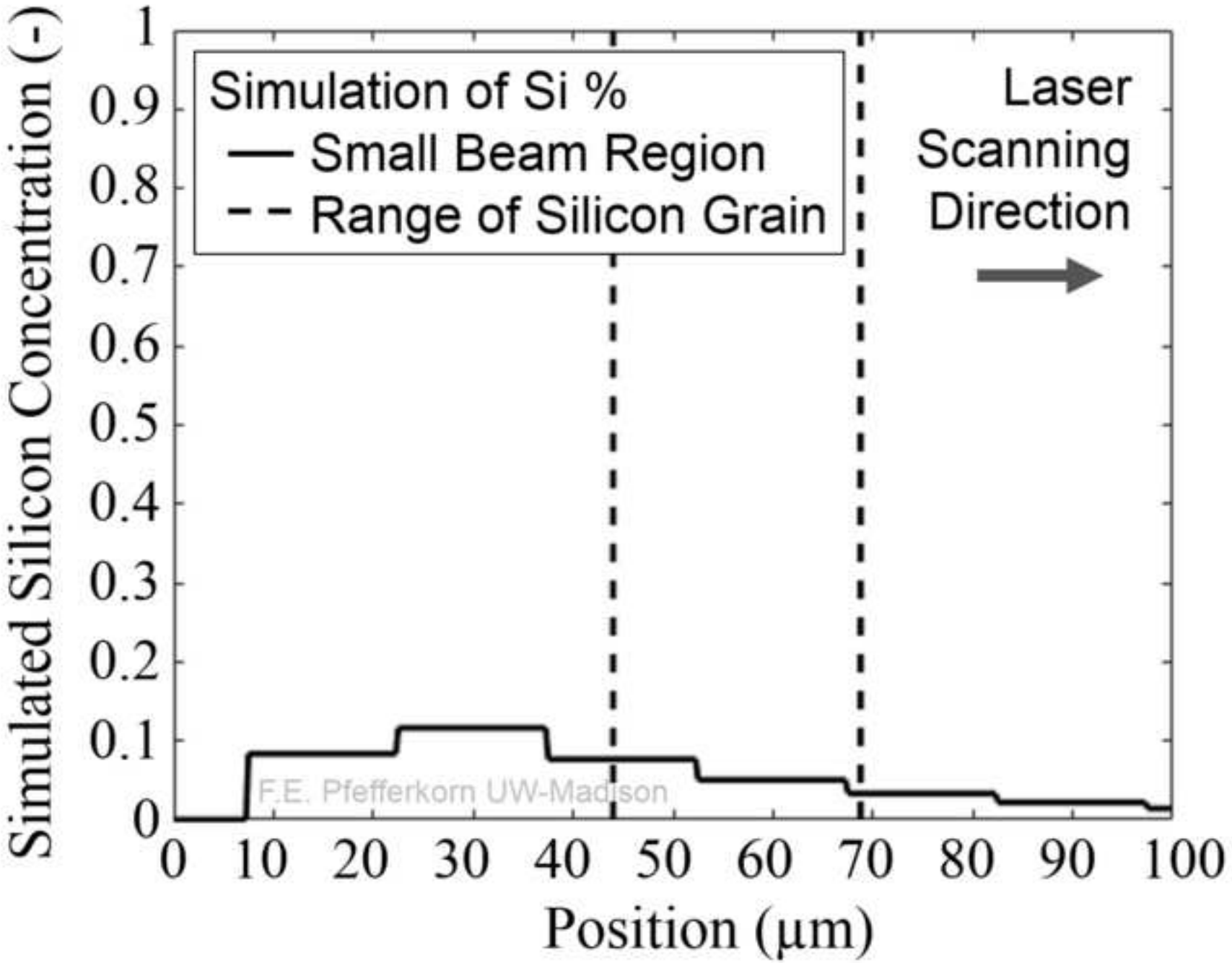

Figure 7a - grayscale
Click here to download high resolution image

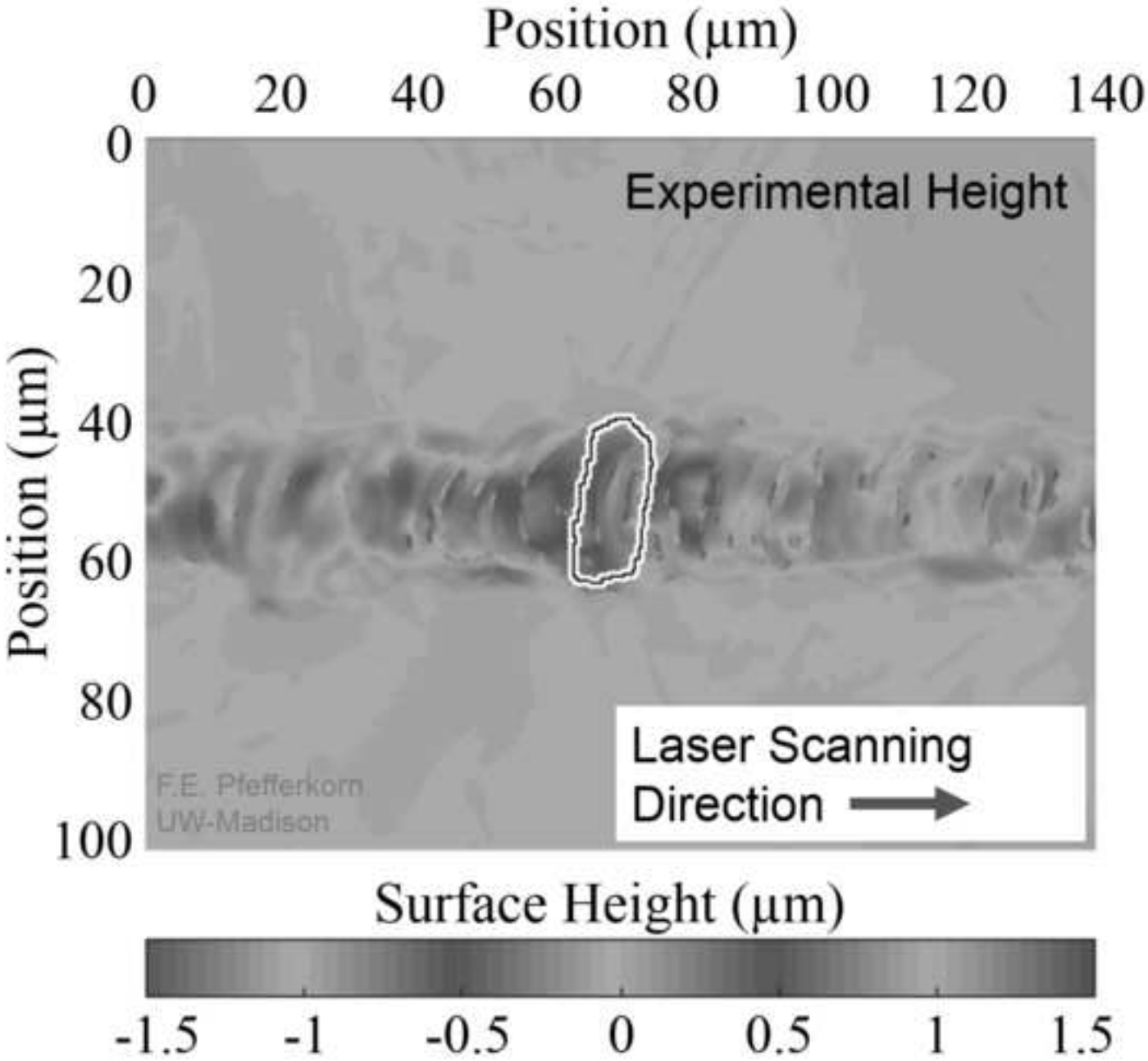

Figure 7b - grayscale
Click here to download high resolution image

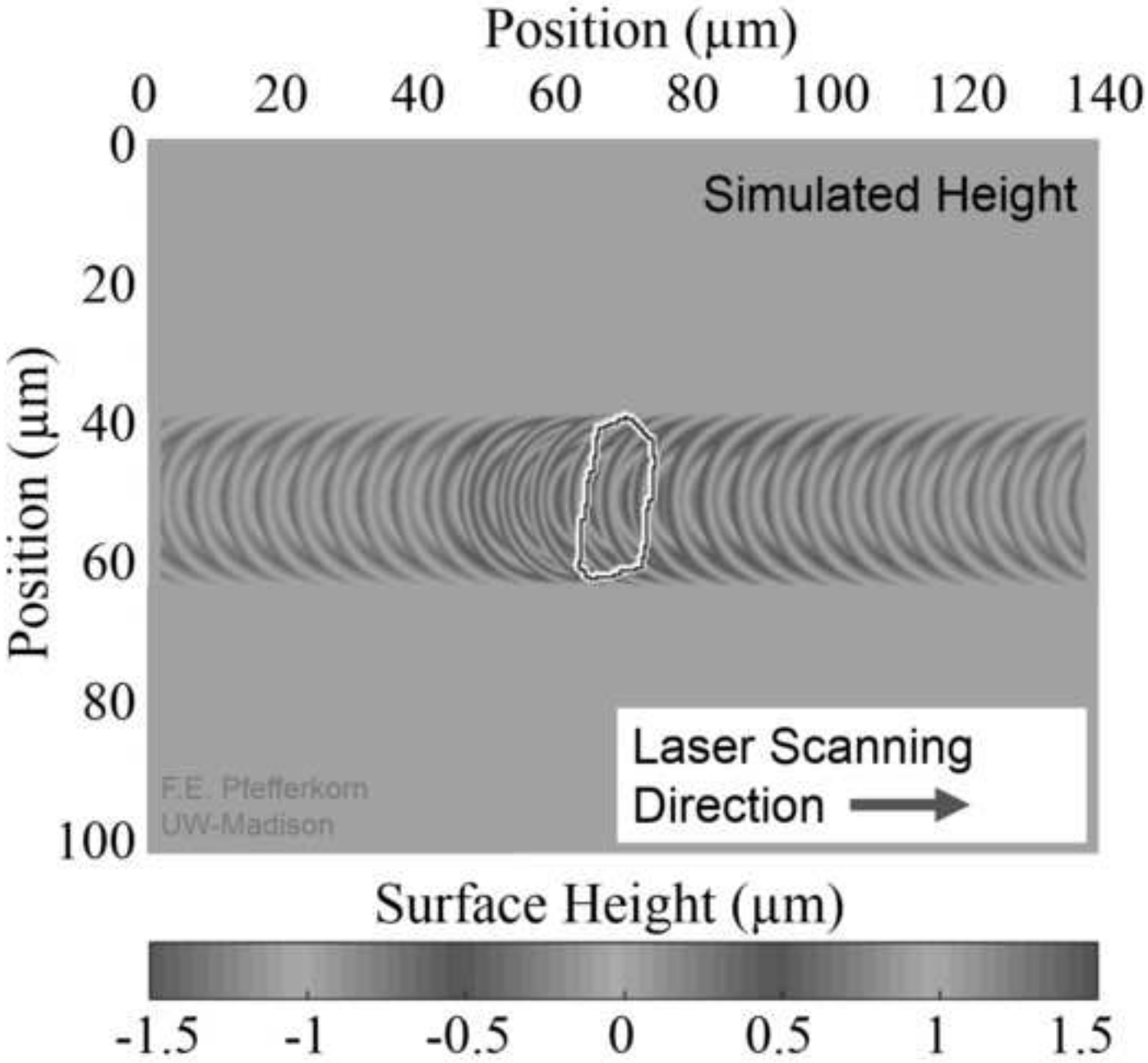

Figure 7c - grayscale
Click here to download high resolution image

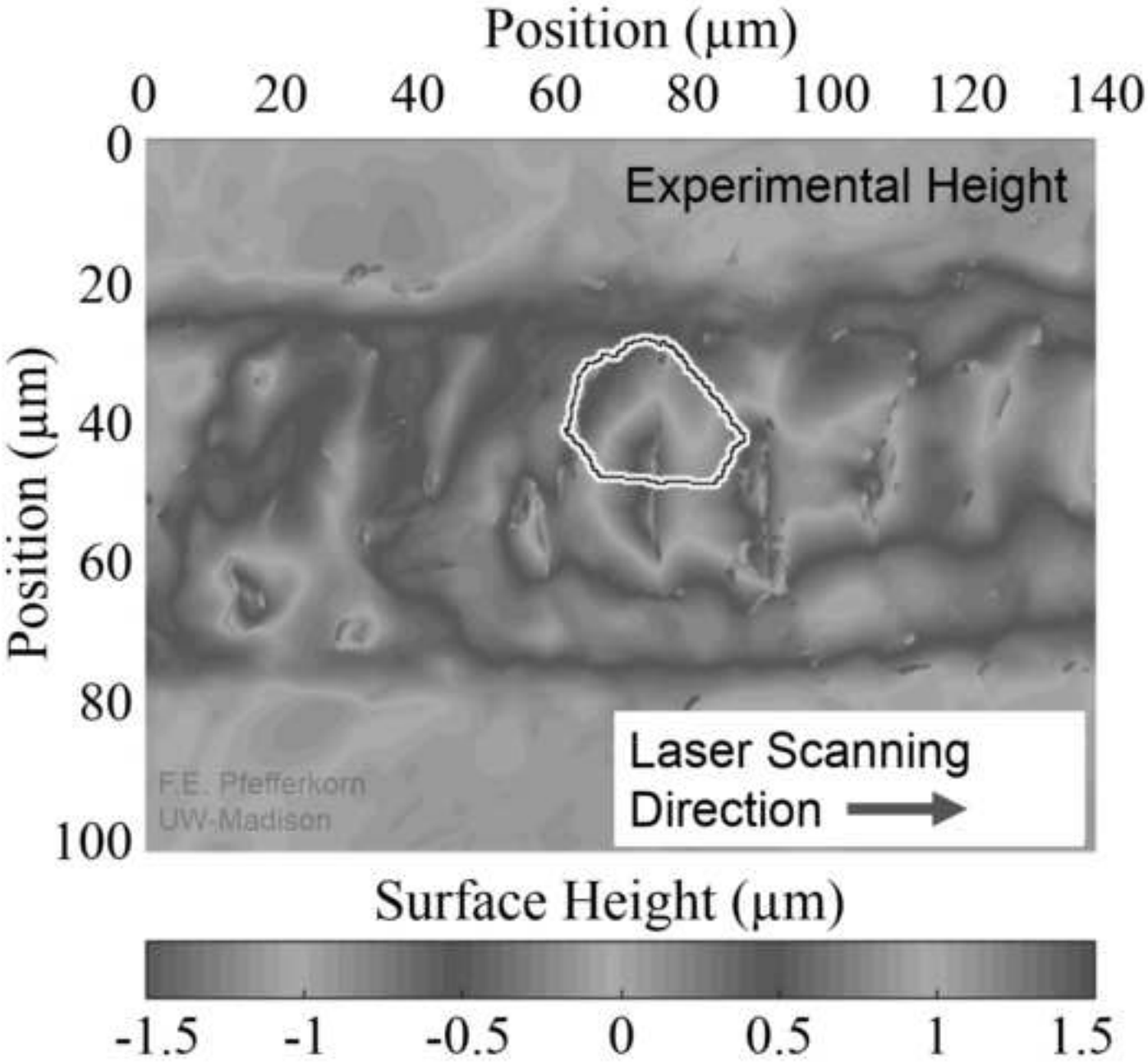

Figure 7d - grayscale
Click here to download high resolution image

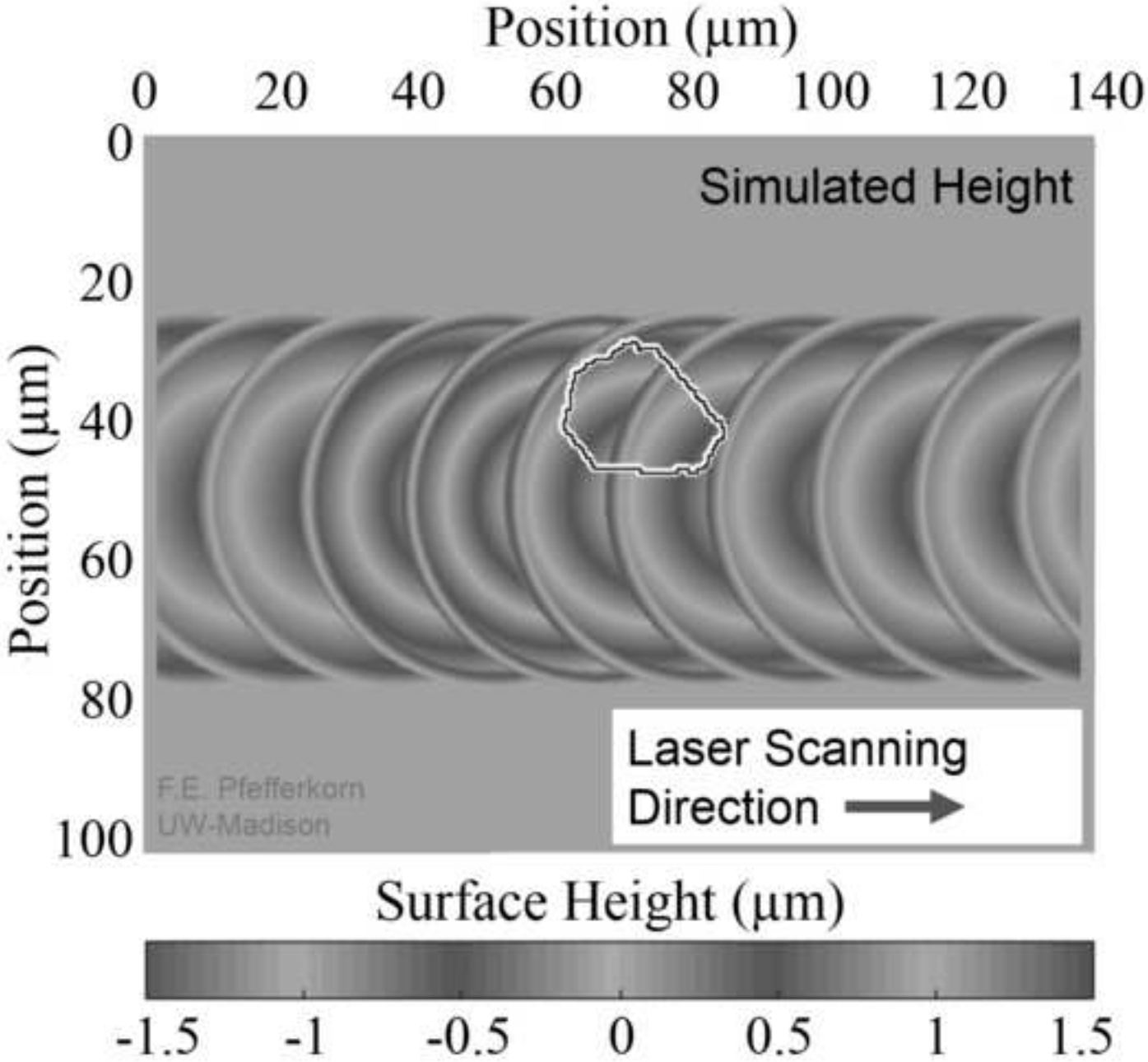

Figure 8a - grayscale
Click here to download high resolution image

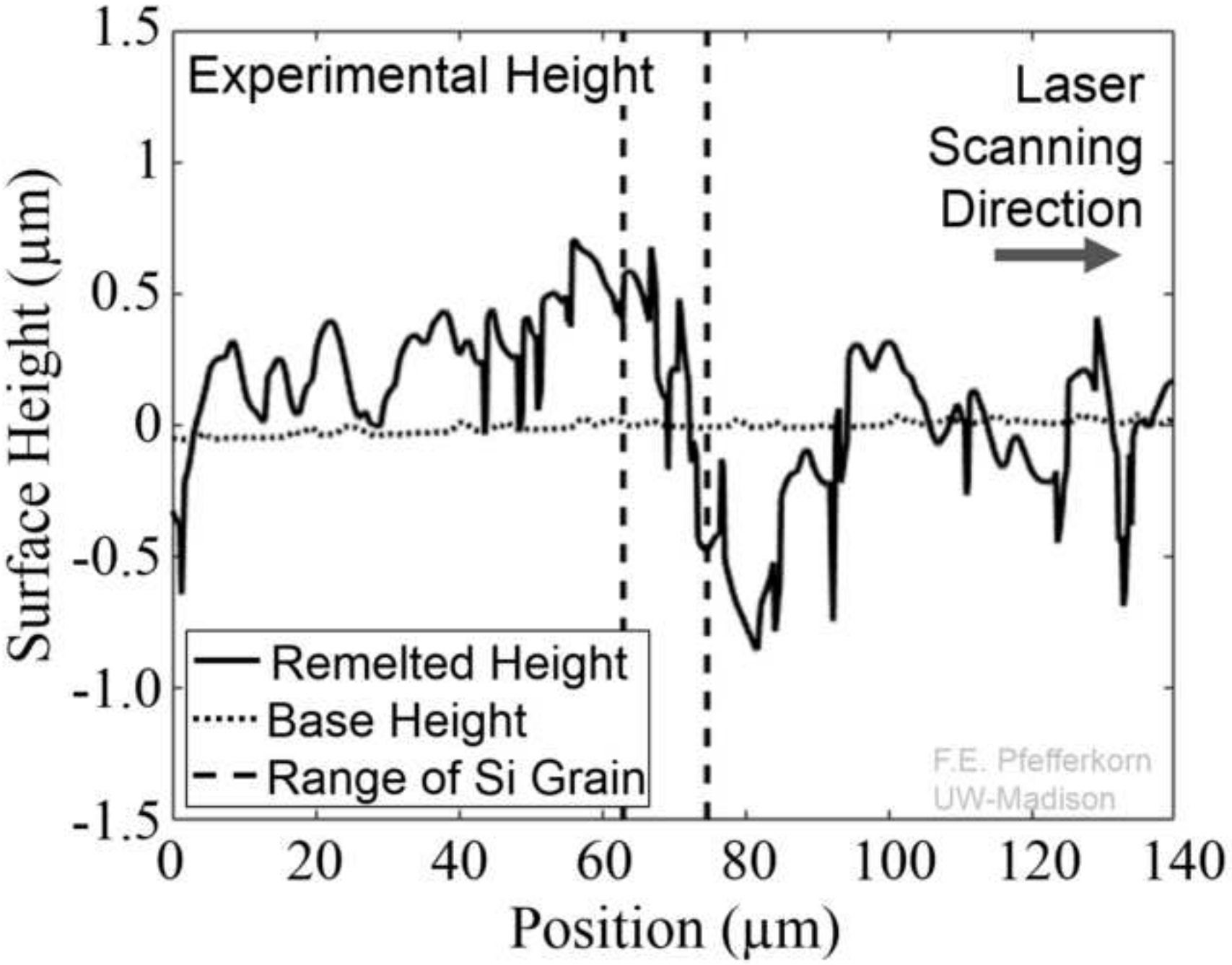

Figure 8b - grayscale
Click here to download high resolution image

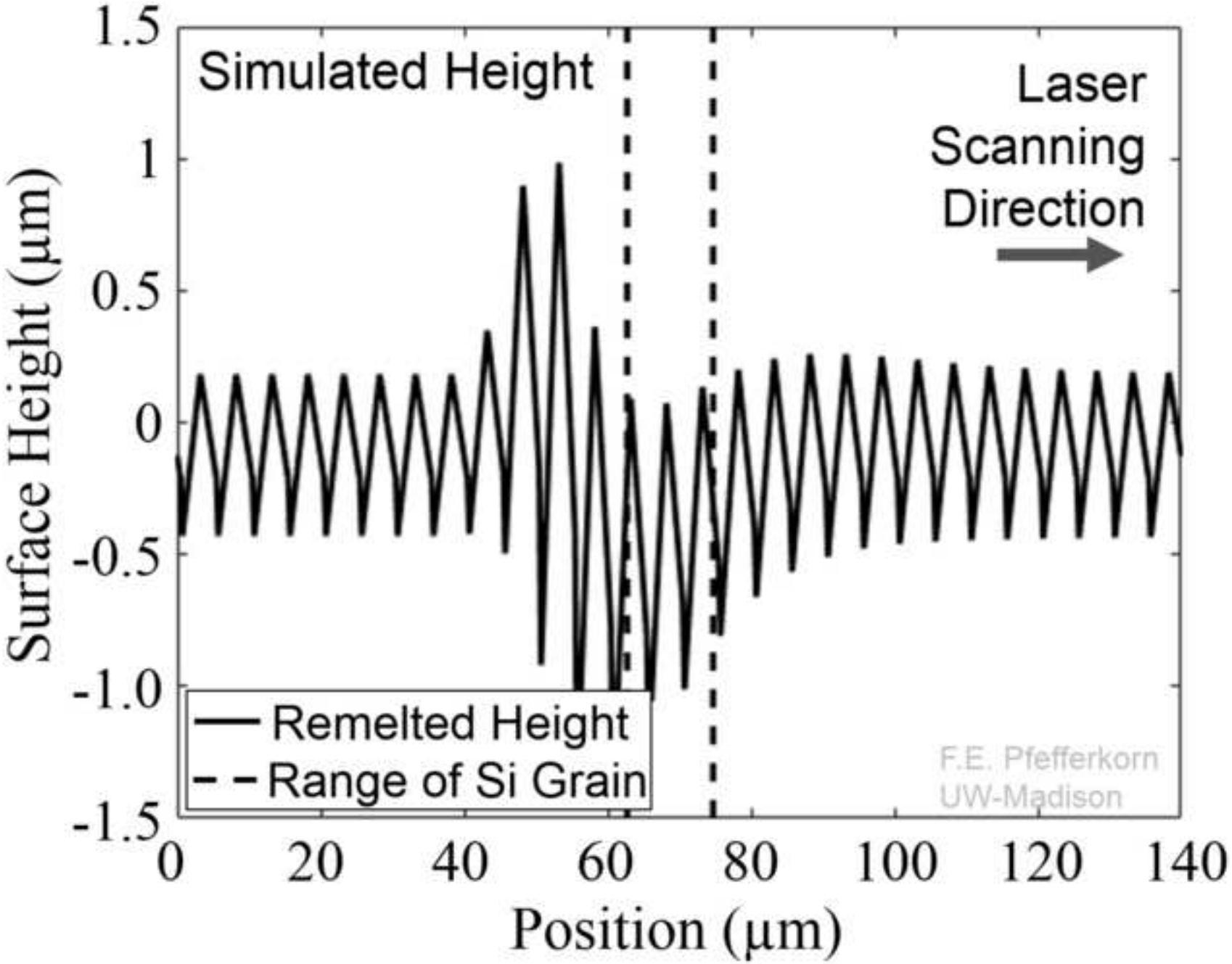

Figure 8c - grayscale
Click here to download high resolution image

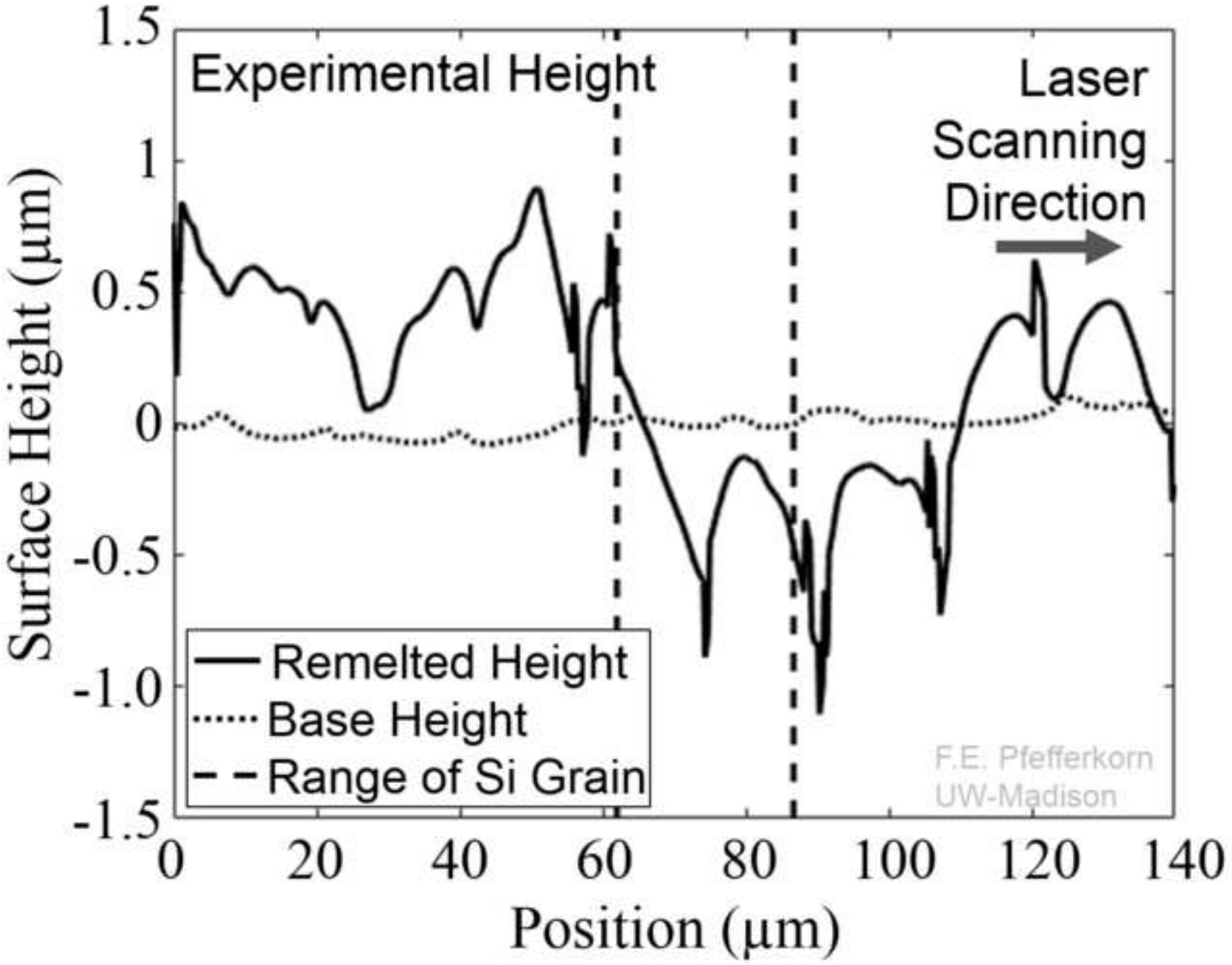

Figure 8d - grayscale
Click here to download high resolution image

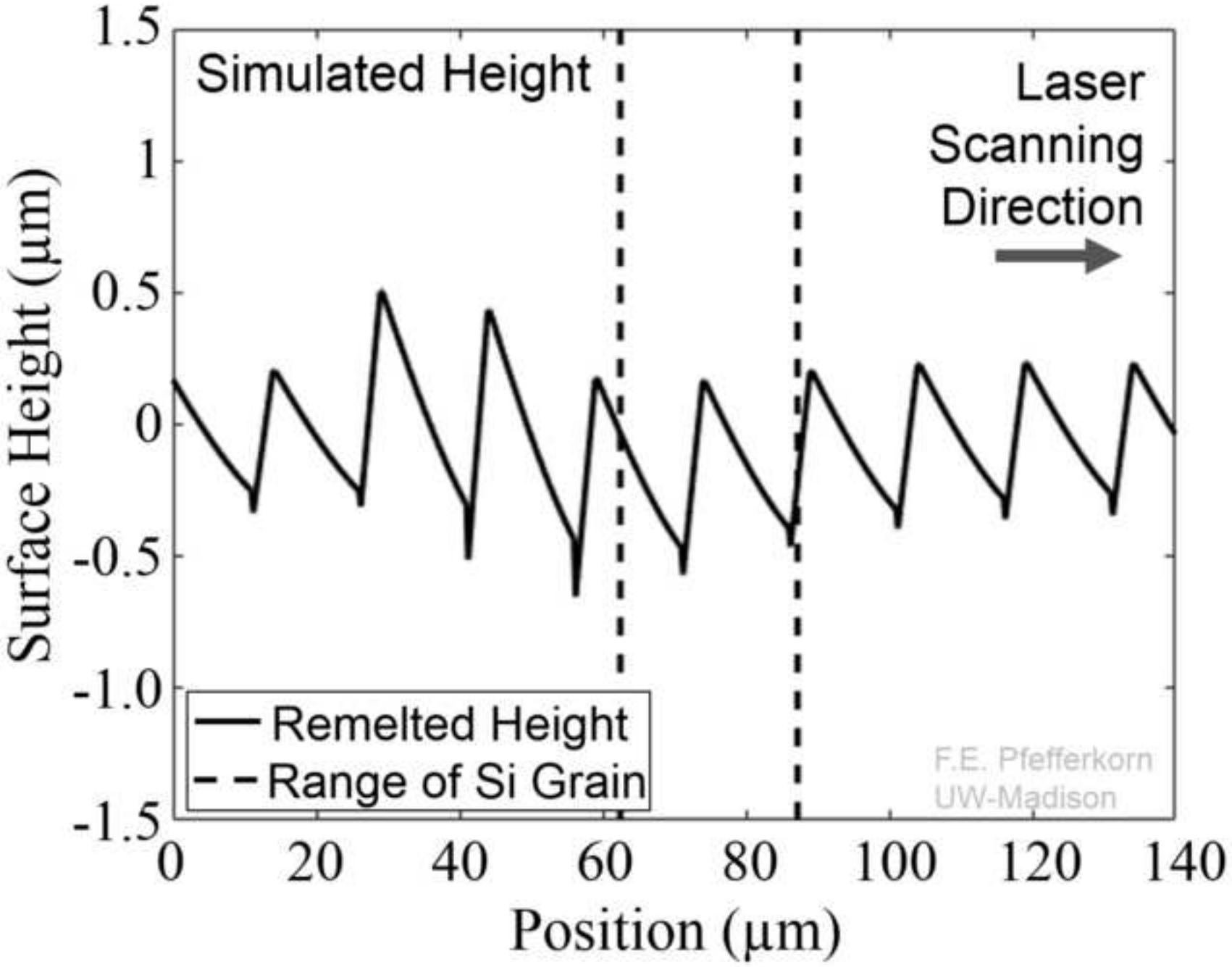

Figure 9a - grayscale
Click here to download high resolution image

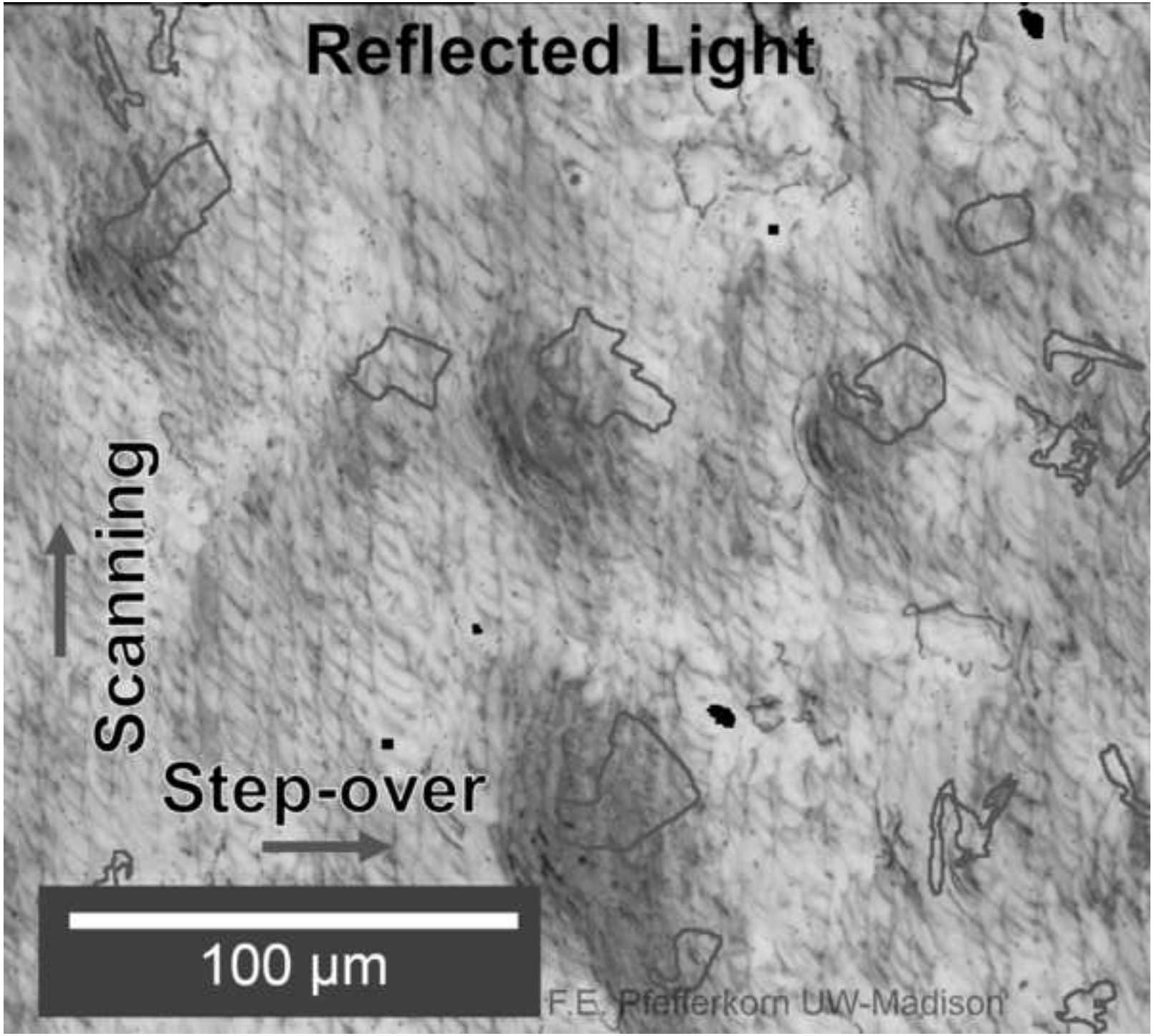

Figure 9b - grayscale
Click here to download high resolution image

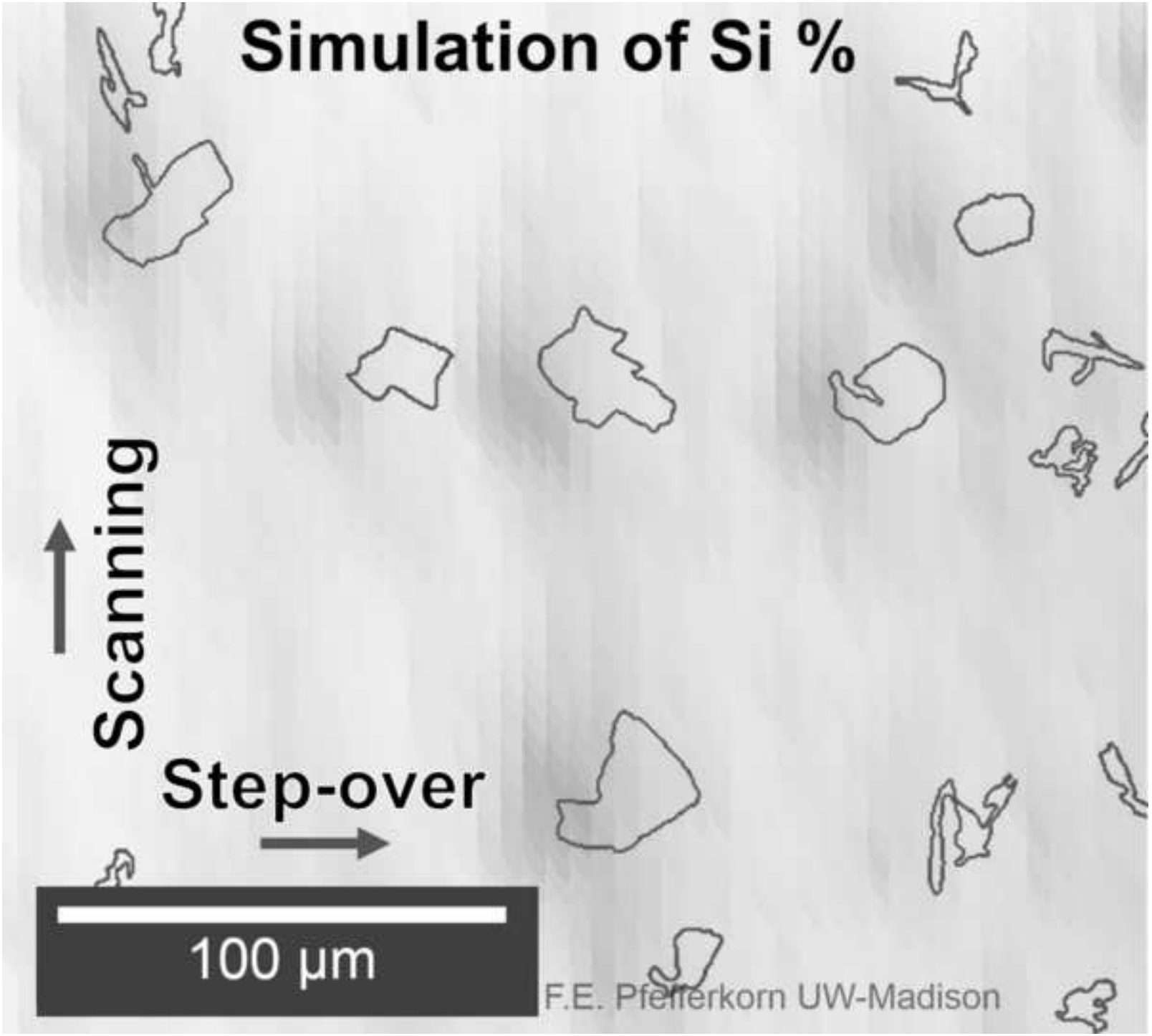

Figure 10a - grayscale
Click here to download high resolution image

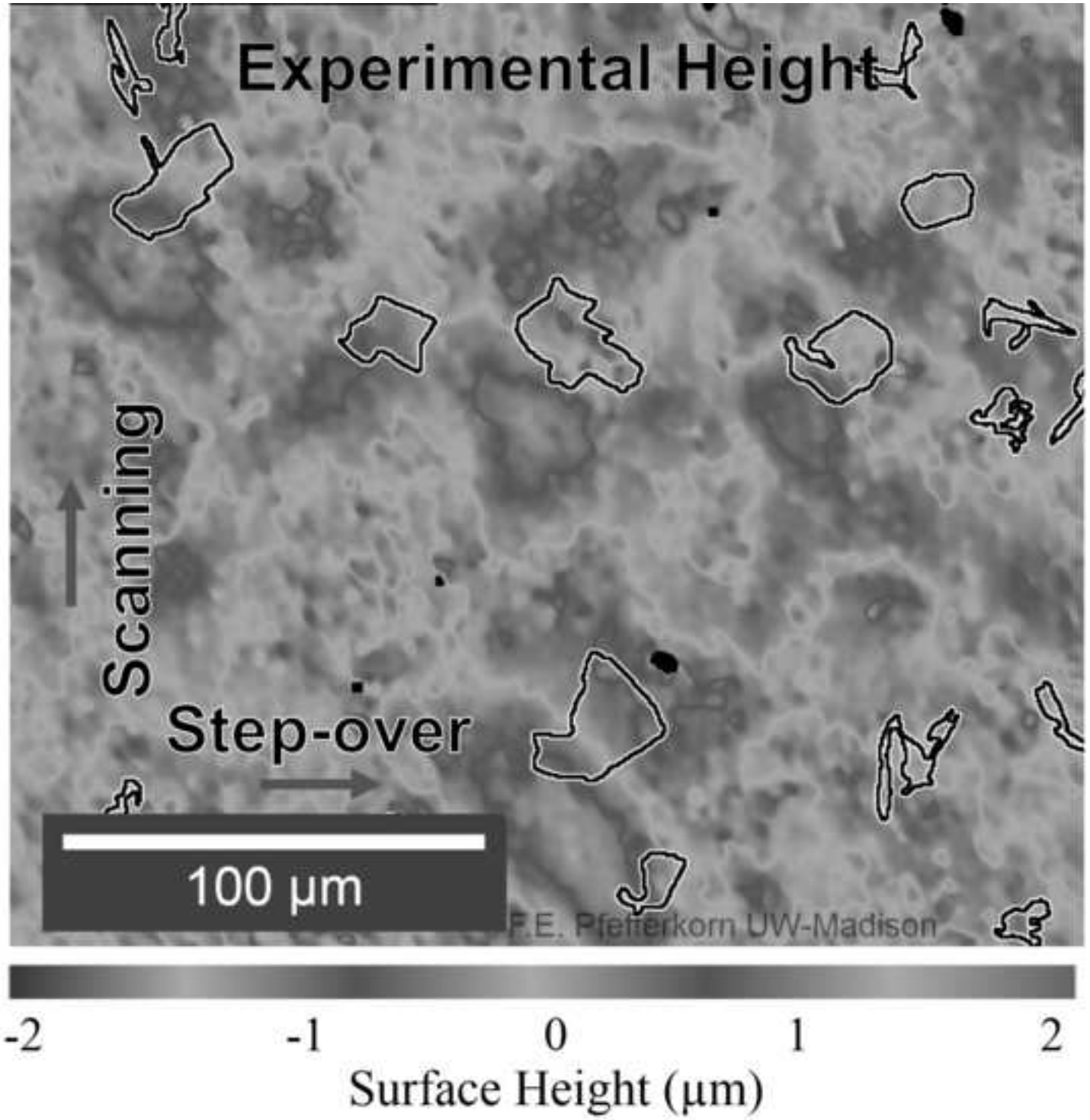

Figure 10b - grayscale
Click here to download high resolution image

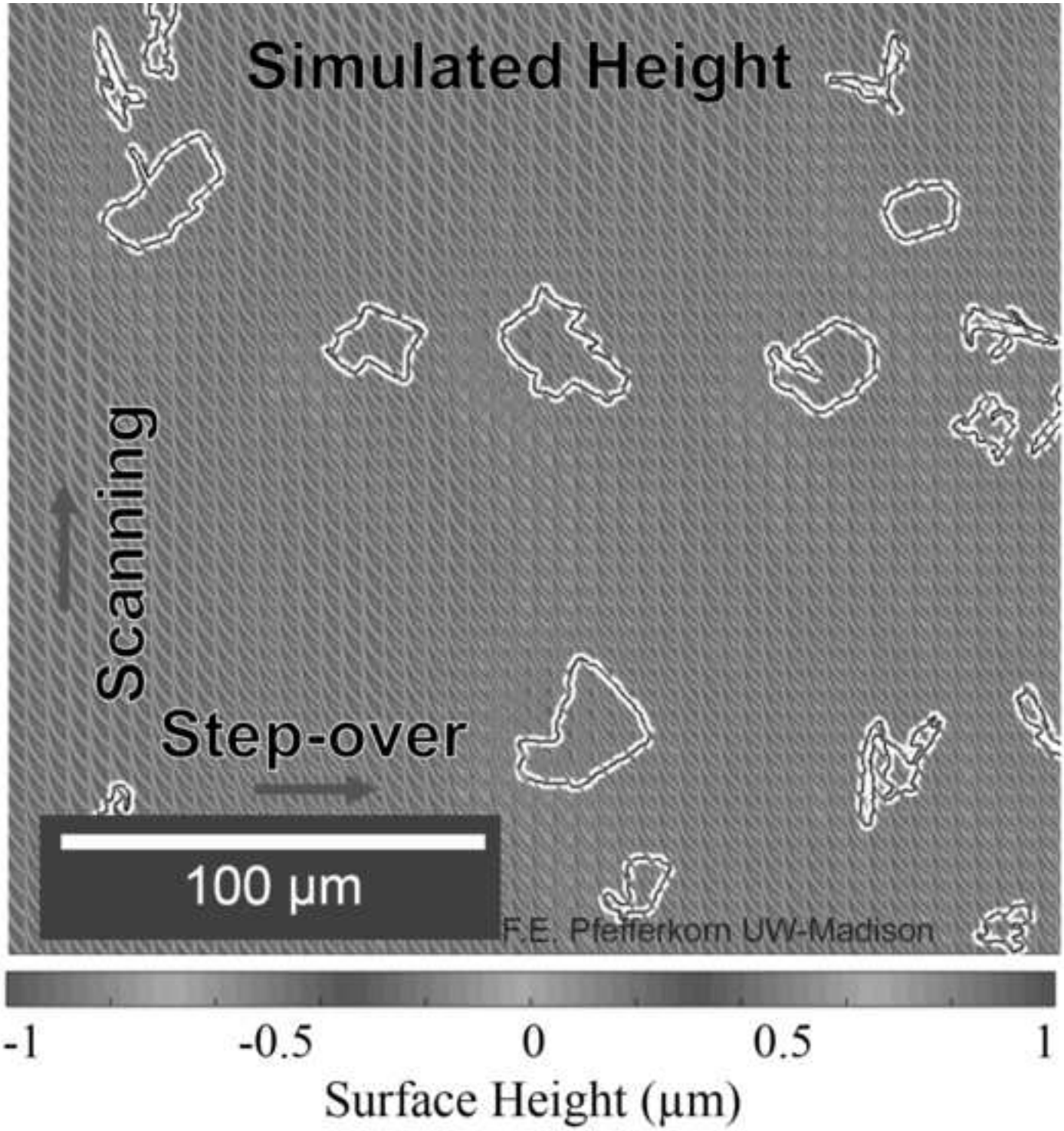

Figure 11a - grayscale
Click here to download high resolution image

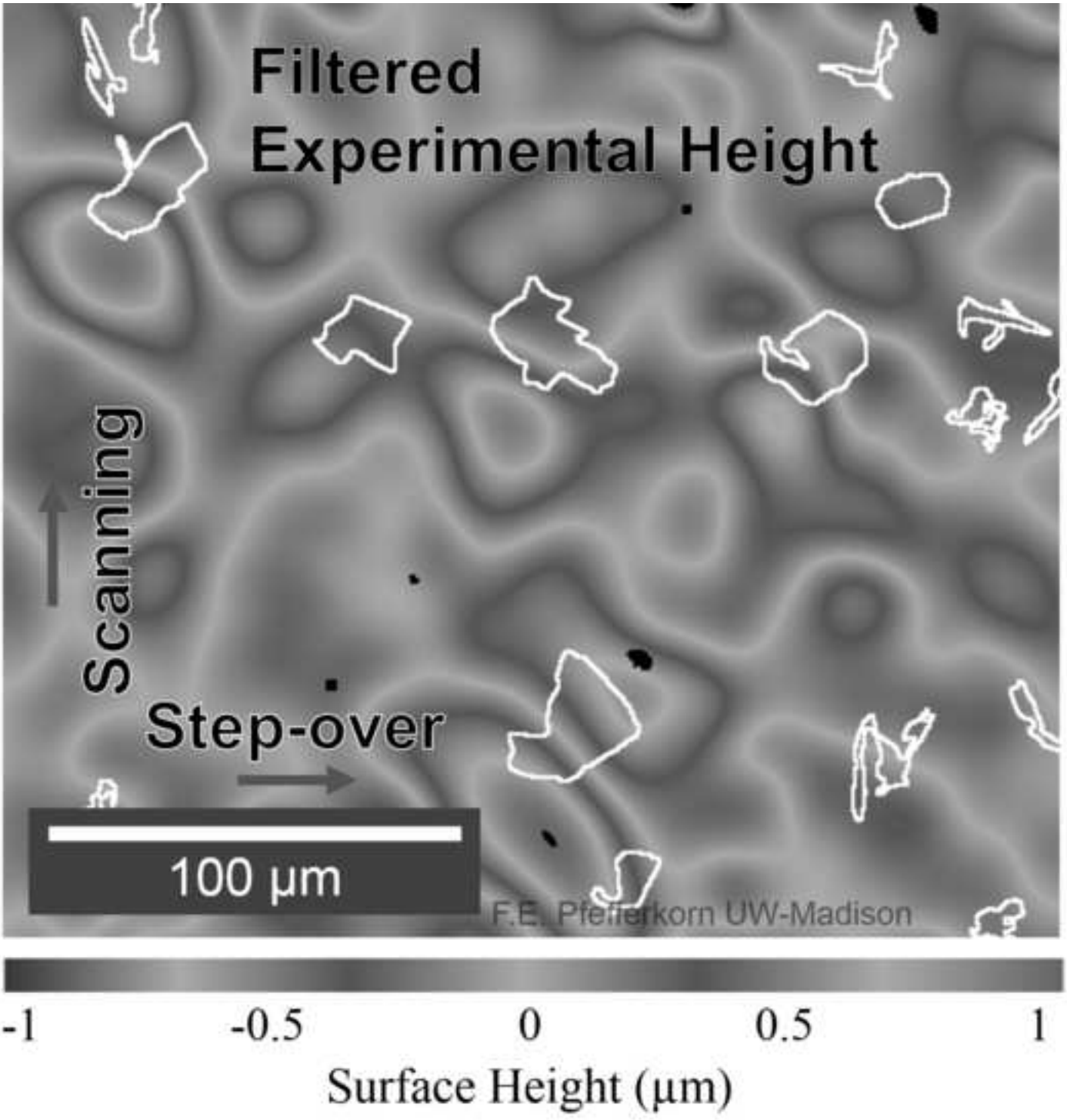

Figure 11b - grayscale
Click here to download high resolution image

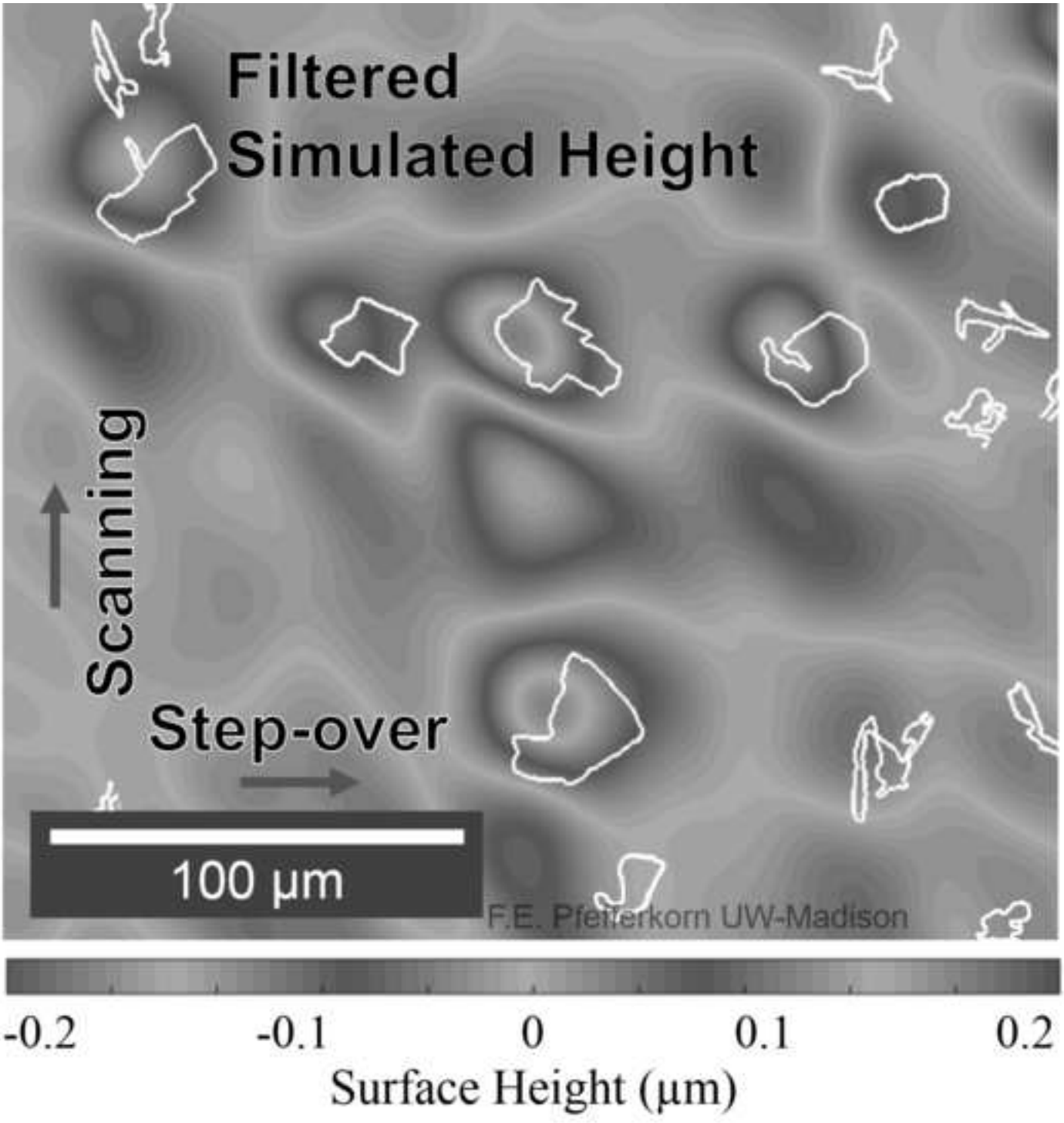

Supplement - Figure 1
Click here to download high resolution image

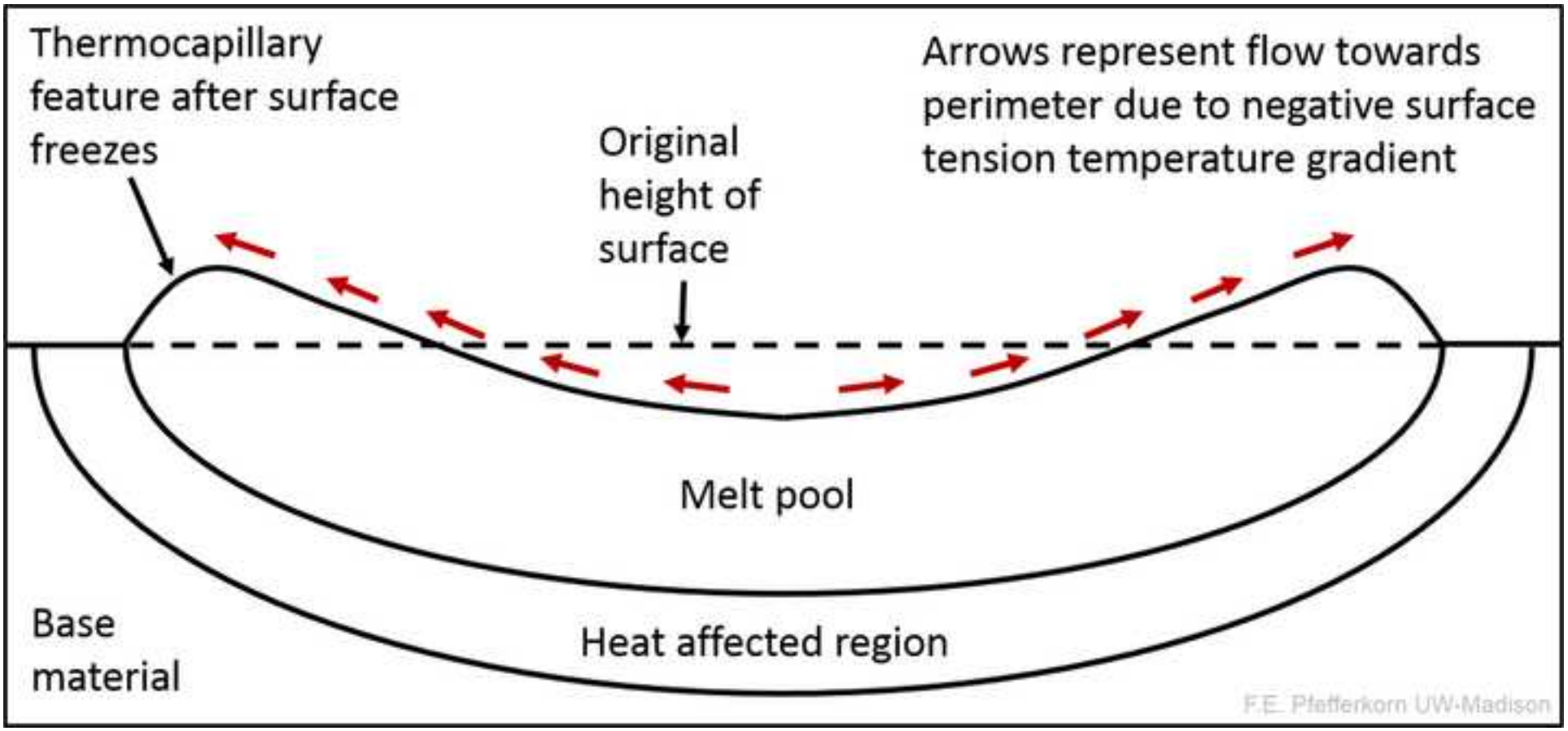

Supplement - Figure 2
Click here to download high resolution image

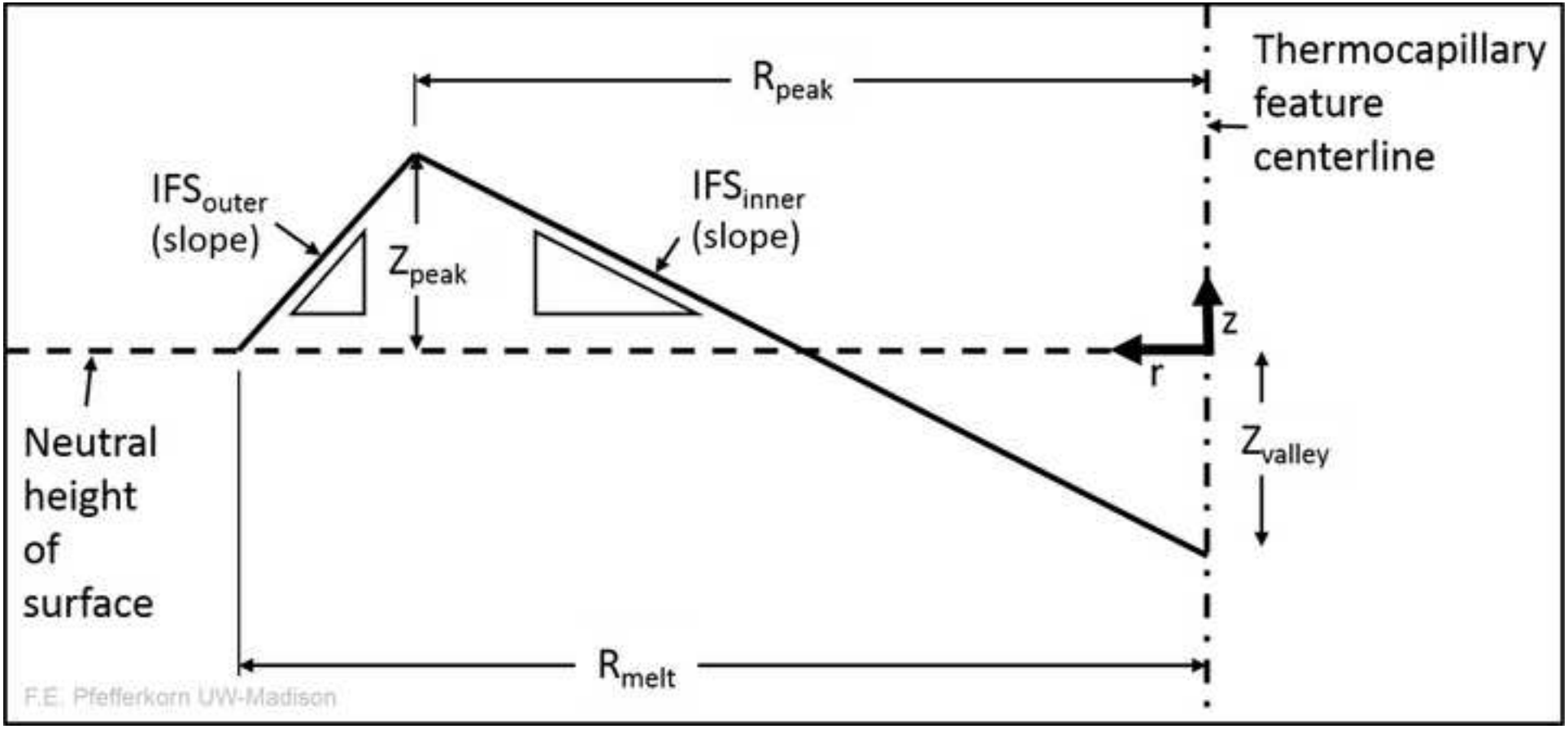

Supplement - Figure 3
Click here to download high resolution image

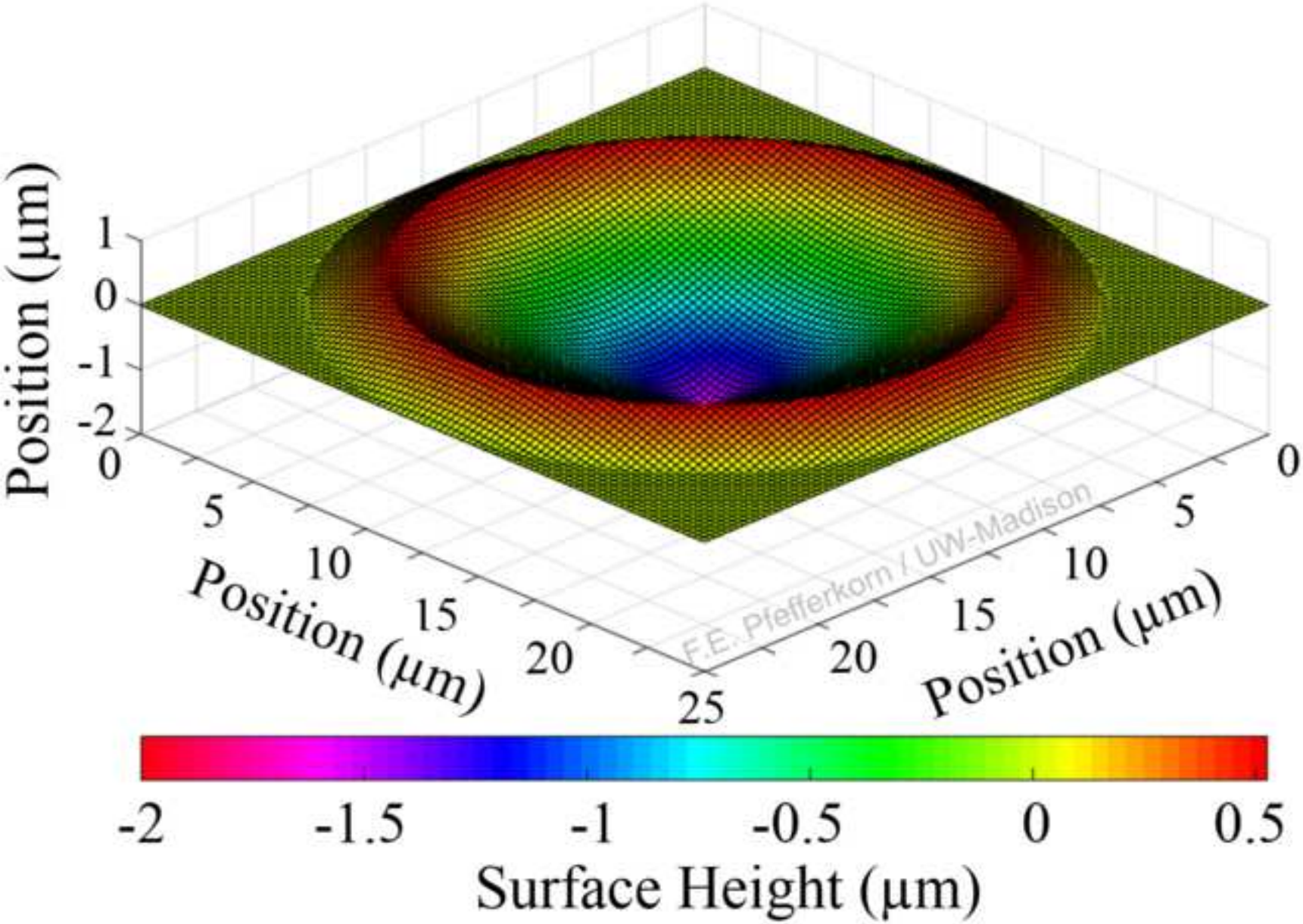

Supplement - Figure 4

Click here to download high resolution image

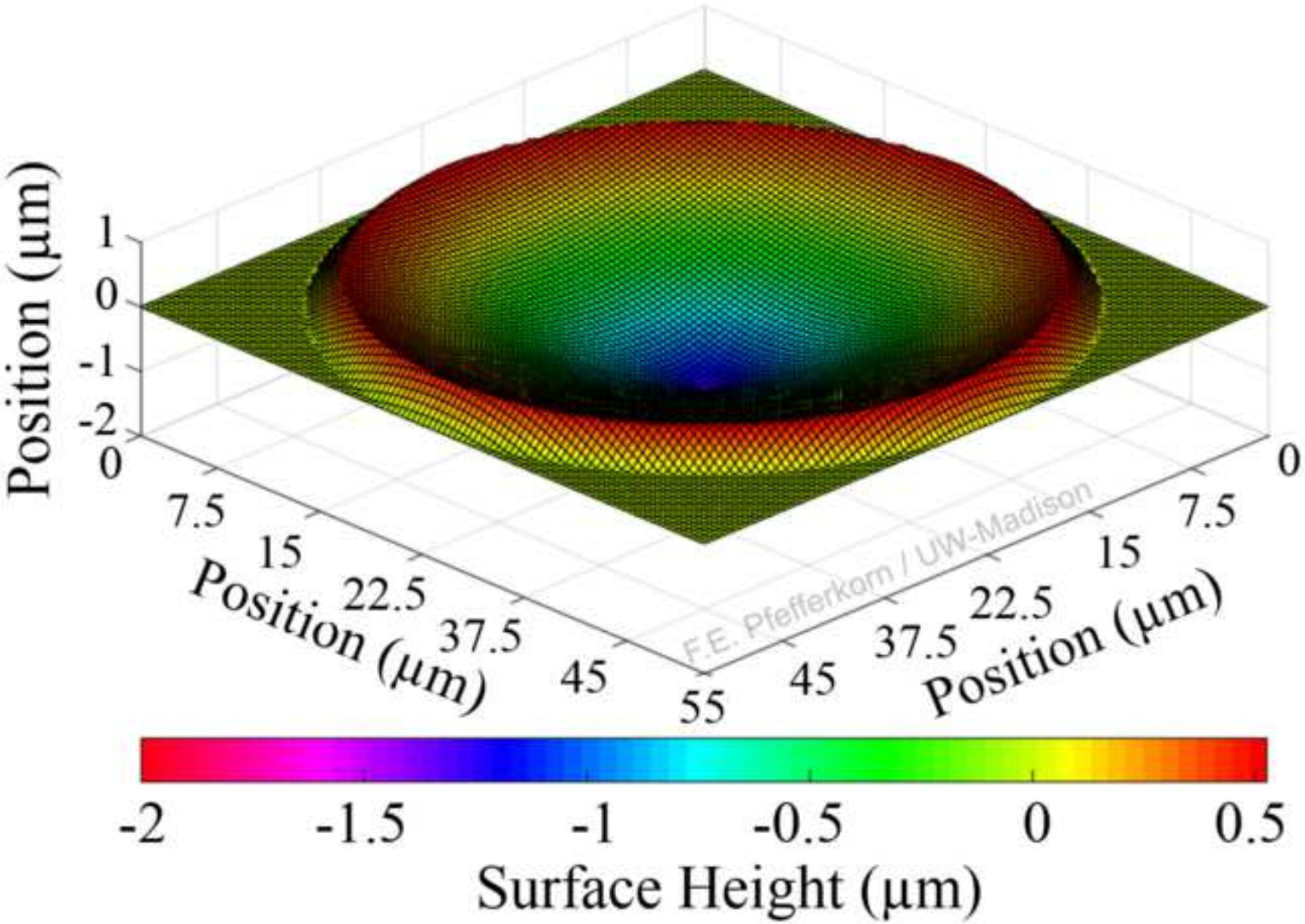

Supplementary Material or Appendix

Click here to download Supplementary Material for on-line publication only: Richter et al Part-2 Supplemental Material 12-17-201